STUDY OF ORTHOGONAL FLUXGATE SENSOR IN TERMS OF SENSITIVITY AND NOISE

FAN JIE

(*B.ENG., UNIVERSITY OF SCIENCE AND TECHNOLOGY OF CHINA*)

A THESIS SUBMITTED FOR

THE DEGREE OF DOCTOR OF PHILOSOPHY

DEPARTMENT OF MECHANICAL ENGINEERING

NATIONAL UNIVERSITY OF SINGAPORE

2010

Acknowledgements

First and foremost, I would like to wholeheartedly thank Prof. Li Xiaoping for his constant encouragement and patient guidance throughout the research carried out in this thesis. The author would also like to thank Prof. Li particularly for his invaluable help in selecting the proper and interesting research topic at the beginning, conveying the fundamentals of magnetic sensors, and recruiting me in the Neurosensors Lab as a research fellow.

I am indebted to Prof. Ding Jun in NUS and Prof. Zhao Zhenjie in East China Normal University for their kind guidance and helpful discussions at the beginning of this project. I would also like to thank Prof. Paval Ripka in Czech Technological University and Prof. Horia Chiriac in National Institute of Research and Development for Technical Physics in Romania for their great guidance and pleasant cooperation during the exchange programme between NUS and their institutions. Their deep insight and rich experience in magnetic materials and magnetic devices helped me solve many problems.

I would like to thank Dr. Shen Kaqiquan, Dr. Seet Hang Li, Dr. Yi Jiabao, Dr. Qian Xinbo, Mr. Ning Ning, Mr. Ng Wu Chun in Neurosensors Lab and all staff in the advance manufacturing lab (AML) for their precious assistance in the project.

Importantly, I deeply appreciate the unwavering support from my family. Mom, Dad, without you, I certainly would not be where I am today. Finally, I want to thank my beloved wife, Liu Yang. I am forever grateful and indebted to her patience, encourage, and love.

Table of Contents

Summary

Research and development of portable fluxgate sensors for precise magnetic field detection are driven by the emerging applications in biomagnetic, military, and medical fields. The main challenges in the miniaturization of the fluxgate sensors are how to enhance the resolution and at the same time reduce the noise. The objective of this project is to investigate the extreme of orthogonal fluxgate sensor in terms of sensitivity and noise, focusing on the design and characterization of the multi-core sensing element materials using ferromagnetic micro-wires and investigating and modeling the physical mechanism of multi-core orthogonal fluxgate effects.

In this study, investigation of the magnetic properties of the micro-wire arrays of $Co_{68.15}Fe_{4.35}Si_{12.5}B_{15}$ glass covered amorphous micro-wires (GCAWs) and $Ni_{80}Fe_{20}$/Cu composite wires (CWs) by hysteresis loops and magnetoimpedance (MI) effect show a strong dependence of the magnetic anisotropy on their physical dimensions and structures. For single wires, the magnetic anisotropy can be tailored by varying the length of the wire and the ratio of the thickness of glass coating layer to the metal core radius. Desirable circumferential anisotropy can be obtained in wires with a critical length smaller than 10 mm and the large glass-metal ratio. For GCAW arrays, the anisotropy inclines to the circumferential direction as the number of wires increases and the dynamic hysteresis loops showed that an ac current flowing into the arrays exasperated such effect. For CW arrays, the anisotropy inclines from the original helical direction to longitudinal direction as the number of wires increases. MI measurement showed, as the number of the wires increases, the frequency of the

maximum MI ratio decreases resulting from the decrease of the domain wall motion frequency caused by the interaction between wires.

The orthogonal fluxgate effect are thoroughly characterized with regard to the optimum parameters that influence the sensitivity and noise, such as working mode, tuning effect, excitation current, and the parameters of the pickup coil. The sensitivity increases exponentially with the increase of the number of wires. The highest sensitivity recorded is 1663 mV/μT in a 21-wire GCAW array and the lowest noise level has been found in a 5-wire array working in fundamental mode.

Based on the measured magnetic properties and orthogonal fluxgate characteristics, the magnetization process of the micro-wire arrays is modeled by three hysteresis loops. A dipolar interaction model taking into account of the compactedness of the micro-wire arrays is proposed and verified by experimental results on the noise level of arrays of CWs. According to this model the 7-wire honeycomb structure is most favourable array structure. Moreover, the nonlinear increase of the sensitivity is attributed to domain unification effect that enlarges the dimension of the effective domain and decreases the domain motion frequency. The decreasing trend of frequency with the number of wires is in good agreement with MI ratio results.

An analytical model of the 2^{nd} harmonic sensitivity of the multi-core orthogonal fluxgate is established showing that the number of wires, anisotropy field, initial susceptibility and frequency are the key parameters determining the sensitivity. The theoretical results agree well with the measured data from GCAW arrays with the number of wires less than ten. Discrepancy in large number of wires occurrs due to

the simplicity of the model and possible nonuniform arrangement of wires. A model of the white noise of the multi-core sensing element provides the theoretical limit of the white noise which is inversely proportional to the number of wires, maximum susceptibility, and working frequency. The noise limit of GCAWs is tens of femtotesla which is far below the experimental results while that of CWs is less than 4 picotesla which is closer to the experimental results.

Finally, in this project a 3-axis multi-core orthogonal fluxgate magnetometer with optimum parameters has been designed, fabricated, and tested. The highest sensitivity of 200 mV/μT in range of +/- 50 μT has been achieved with the noise level of 8.5 pT/rtHz@1 Hz, using 7-wire honeycomb structured GCAW array. The lowest noise level of 6 pT/rtHz@1 Hz has been achieved in range of +/- 15 μT, using a 10-wire GCAW array. Compared with commercial off-the-shelf magnetometers the novel multi-core orthogonal fluxgate magnetometer is competitive in regard to the sensitivity, noise, and size.

In conclusion, both the sensitivity and noise depend on the number of wires and the magnetic properties of the multi-core sensing element arrays. The extreme of the sensitivity has no limit as long as the magnetic properties have not been deteriorated as the number of wires increases. The noise in the micro-wire arrays has a minimum with an optimum structure. However, the theoretical minimum of the white noise is much smaller than the experimental one and is inversely proportional to the number of wires and the susceptibility of arrays.

List of Journal Publications

1. J. Fan, J. Wu, N. Ning, H. Chiriac, X.P. Li, "Magnetic dynamic interaction in amorphous microwire", *IEEE Trans. Magn.*, vol46, No.6, Jun. 2010, 2431-2434

2. P. Ripka, M. Butta, Fan Jie, Xiaoping Li, "Sensitivity and noise of wire-core transverse fluxgate, *IEEE Trans. Magn.*, vol46, No.2, Feb. 2010, 654-657

3. P. Ripka, X.P. Li, J. Fan, "Multiwire core fluxgate, *Sensors and Actuators A: Physical*, *Volume 156, Issue 1*, *May 2009*, *Pages 265-268*

4. J. Fan, N. Ning, J. Wu, X.P. Li, H. Chiriac, "Study of the Noise in Multicore Orthogonal Fluxgate Sensors based on Ni-Fe/Cu Composite Microwire Arrays", *IEEE Trans. Magn*, Vol45, No.10, Oct. 2009, 4451 - 4454

5. Z.J. Zhao, X.P. Li, J. Fan, H.L. Seet, X.B. Qian, P. Ripka, "Comparative study of the sensing performance of orthogonal fluxgate sensors with different amorphous sensing elements", *Sensors and Actuators A: Physical*, *Volume 136, Issue 1*, *1 May 2007*, *Pages 90-94*

6. X.P. Li, H.L. Seet, J. Fan, J.B. Yi, Electrodeposition and Characteristics of $NI_{80}Fe_{20}$/Cu Composite Wires, *Journal of Magnetism and Magnetic Materials,* 304 (2006), 111-116

7. Ning Ning, Li Xiaoping, Fan Jie, Ng Wu Chun, Xu Yongping, Qian Xinbo, Seet Hang Li, "A tunable magnetic inductor*", IEEE Trans. Magn*, vol42, No.5, 2006, 1585-1590

8. X.P. Li, J. Fan, J. Ding, H. Chiriac, X.B. Qian, J.B. Yi, "A Design of Orthogonal Fluxgate Sensor", *Journal of Applied Physics*, 99, 1 (2006)

9. X.P. Li, J. Fan, X.B. Qian, J. Ding, "Multi-core orthogonal fluxgate sensor", *Journal of Magnetism and Magnetic Materials*, 300 (2006) e98-e103

10. J. Fan, X.P. Li, P. Ripka, "Low Power Orthogonal Fluxgate Sensor with Electroplated $Ni_{80}Fe_{20}$/Cu Wire", *Journal of Applied Physics*, 99, 1 (2006)

11. P. Ripka, X.P. Li, J. Fan, "Orthogonal fluxgate effect in electroplated wires", *IEEE Sensors Journal*, Oct. 31, 2005, pp69-72

12. Qian, X., Li, X., Xu, Y.P., Fan, J., "Integrated Driving and Readout Circuits for Orthogonal Fluxgate Sensor", *IEEE Transactions on Magnetics*, vol41, No.10, Oct. 2005, 3715-3717

List of Figures

List of Tables

List of Symbols

H	Magnetic Field Strength
B	Magnetic Flux Density
M	Magnetization
M_s	Saturation Magnetization
H_c	Coercivity
H_k	Anisotropy Field
μ_0	Vacuum Permeability
μ_i	Initial Permeability
μ_r	Relative Permeability
χ	Susceptibility
J	Atom Quantum Number
A	Cross-sectional Area
N	Number of Turns
D	Demagnetization Factor
Φ	Magnetic Flux
f	Frequency
ω	Angular Frequency
S	Sensitivity
δ	skin depth
σ	Conductivity
k_B	Boltzmann constant
Z	Impedance
I	Current
V	Volume

Chapter 1 Introduction

1.1 Magnetic Sensors Overview

Magnetic sensors are the devices that detect the existence of magnetic field by measuring the absolute value or relative change of the magnitude and the direction of the magnetic field intensity. Magnetic sensors are probably the oldest sensing technology in the human history. It is believed that ancient Chinese invented the first compass, namely the first magnetic sensor, around 4,000 years ago [1]. However, we can also regard the magnetic field sensor as one of the most advanced technologies today. Nowadays magnetic sensors are used widely in industry, military, medical treatment, space research, geology, etc. Magnetic sensors can be found almost everywhere in our life, from digital compasses in mobile phones to hard disk readers in data storage systems, from unexploded ordnance (UXO) trackers in battle field to magnetic anomaly detector (MAD) for submarines searching in sea warfares, from magnetoecephalography (MEG) for brain signals monitoring to endoscope for interior body organ examining, from magnetic flux leakage (MFL) detector for oil pipelines to magnetometers equipped in Mars explorer, … The world magnetic sensor market was about USD 883 million and will reach to USD 2~20 billion in 2010 [2] benefiting from the increasing number of magnetic sensors used in various applications. For example, the number of magnetic sensors equipped in an average automobile was about 20 in 2007 and expected to exceed 50 soon [3].

The popularity of magnetic sensors mainly results from the advantages that they are: 1) non-invasive and non-destructive, the sensors can be in a distance to the

objects since the magnetic field distributes in the whole space; 2) versatile, physical parameters such as displacement, velocity, current density, stress, etc can be transduced to magnetic signal by specific sensing elements; and 3) highly reliable and safe, magnetic sensors can be used unattendedly in harsh conditions with loud noise, serious pollution, and large temperature variation.

1.2 Motivation

The trend of magnetic sensor development is towards smaller, faster, cheaper, more sensitive and more reliable. Especially new horizons in bio-magnetic field measurement and battlefield remote detection require portable and reliable magnetic sensors with ultra high sensitivity, low noise, and small size. For typical bio-magnetic field ranging from 10^{-15} to 10^{-10} Tesla, currently the only qualified technology is superconducting quantum interference device (SQUID). However, the demanding requirement of the cryogenic equipment and small dynamic range of SQUID restrict its portable and low power applications. Fluxgate is the next. When required resolution is in the range of 10^{-9} to 10^{-10} Tesla, fluxgate sensors, the most popular high-end magnetic sensors, are the best choice because of their advantages in linearity, temperature stability, and cost. The only weakness of the fluxgate sensors is the large size of the sensing element based on bulk ferromagnetic materials which limits further miniaturization and low power portable applications.

Therefore, the main challenges for fluxgate sensor studies are how to enhance the resolution and at the same time reduce the size. However, resolution and size are two contradictory parameters in conventional fluxgate using bulk materials as sensing elements: the smaller the size of the sensing elements, the higher the noise level. To

break through this dilemma, new materials and new approach have to be brought up. Thanks to the advances of the fabrication process in the past two decades, micro-sized ferromagnetic wires with excellent soft magnetic properties have been developed, among which $Co_{68.15}Fe_{4.35}Si_{12.5}B_{15}$ glass covered amorphous wires (GCAWs) prepared by Taylor-Ulitovsky method and nanocrystalline $Ni_{80}Fe_{20}$/Cu composite wires (CWs) prepared by electrodeposition stand out. These two kinds of micro-wires have advantages over other materials in that they are more uniform in shape and more stable in properties. In the early 21st century, GCAWs replaced the bulk materials used in orthogonal fluxgate sensors working as a single sensing element, which offers orthogonal fluxgate sensors great potential for miniaturization. However, the extreme of the orthogonal fluxgate sensor in terms of sensitivity and noise is unknown. Especially, if the bulk single core sensing element was replaced with a multi-core sensing element, in the form of an array of multiple ferromagnetic micro-wires with the desirable magnetic properties, the limitations in sensitivity and noise of the conventional fluxgate sensors would be broken through. This novel idea technologically motivates this project of developing a multi-core orthogonal fluxgate sensor with high sensitivity and low self-noise.

1.3 Objectives and significance of the Study

The main objective of this project is to investigate the extreme of orthogonal fluxgate sensor in terms of sensitivity and noise, focusing on the design and characterization of the multi-core sensing element materials using ferromagnetic micro-wires and investigating and modeling the physical mechanism of multi-core orthogonal fluxgate effects. The detailed objectives are:

1. To investigate the static and dynamic magnetic properties of multi-core sensing element based on GCAWs and CWs and study the effect of structure parameters, i.e. the number of wires in the micro-wire array, the geometry of the array, etc. on the magnetic properties;
2. To investigate the orthogonal fluxgate effect of multi-core sensing element based on GCAWs and CWs including characterization of fluxgate responses, dependence of sensitivity and noise on the number of wires, and interactive effect between multiple wires in the micro-wire array;
3. To model the magnetization process of the micro-wire arrays with certain anisotropy based on the experimental measurement, to theoretically study the interactive effect in the micro-wire array, and to formulate the sensitivity and noise by modeling the multi-core orthogonal fluxgate responses;
4. To develop a multi-core orthogonal fluxgate magnetometer with the highest possible sensitivity and lowest possible noise level as well as balanced performance including the size, power consumption, and stability.

This study incorporates both experimental and theoretical research in the orthogonal fluxgate effects on the multiple micro-wire structures. The central problems in the experimental study are design and characterization of the micro-wire arrays with novel structures to achieve the extreme performance in terms of sensitivity and noise, since the array structures directly affect the field distribution which is closely related to mechanism of the orthogonal fluxgate effects. For the theoretical study, analytical models has to be proposed to describe the magnetic properties of the micro-wire arrays and physics mechanism of the orthogonal fluxgate effects and to predict the

sensitivity and noise limitations of the sensors. Due to the complication of the problem, other sensor properties, such as temperature stabilities, operation range, linearity, etc are not in the scope of the modeling.

The results of the present study could provide a new design process for the weak field magnetic sensors with improved sensitivity, noise level, size and power consumption. The orthogonal fluxgate sensors with optimum structured multi-core sensing element are promising for the applications in weak field detection. Also, the dynamic characterization of multi-core structure and numerical modeling of the multi-core orthogonal fluxgate effect may enhance the understanding of the ferromagnetism of such micro-structured materials.

1.4 Organization of Thesis

A literature review on the state-of-the-art magnetic sensors is provided in Chapter 2 which introduces their classification, basic principles and mechanism, and applications. Attention has been paid to fluxgate sensors with both parallel and orthogonal types. The latest research findings on orthogonal fluxgate are presented. Furthermore, the noise sources in fluxgate sensors and the materials used for the fluxgate sensors which are the key issues of the main objective are reviewed. Chapter 3 describes the proposed research approach for this work and the characterization tools and experimental setups used in the project. The main contributions of this doctorial study start from Chapter 4 which presents the investigation of the static and dynamic magnetic properties of multi-core sensing element based on GCAWs and CWs and the effect of structure parameters, i.e. the number of wires in the multi-core array, the geometric of the array, etc. on the magnetic properties. Chapter 5 presents

the orthogonal fluxgate effects of multi-core sensing element based on GCAWs and CWs including characterization of fluxgate responses, dependence of sensitivity on the number of wires, and the interaction between multiple wires in the micro-wire array. The theoretical work is presented in Chapter 6 which describes the anisotropy and domain dynamics of the multi-core sensing element and the interaction in the micro-wire arrays. The sensitivity and noise of the multi-core orthogonal fluxgate are formulated. Comparison between theoretical results and experimental results is presented. Chapter 7 describes the design and development of the multi-core orthogonal fluxgate magnetometer in details from sensor head to readout circuit, as well as the testing results of sensitivity, noise level and other performance, for example, thermal stability. Comparison of the main performance between our prototype and commercial off-the-shelf magnetometers is tabulated. Finally the conclusions are provided in Chapter 8 summarizing the whole thesis contributions and proposing the future work.

Chapter 2

Background of Magnetic Field Sensors

Starting with a brief introduction of the applications and comparison of state-of-the-art magnetic field sensors, this chapter elaborates the background of the fluxgate sensors in regard to their principles, modeling, and latest research findings. Relevant literatures in noise and materials are also reviewed with emphasis on those needed for the subsequent chapters.

2.1 Introduction

Magnetic sensors play a significant role in physical measurements in a large range of applications [4] in which they provide safe, non-invasive and non-destructive means of detection. Magnetic field sensors measure the magnetic field directly, while other magnetic sensors use the field as an intermediary carrier for detecting some non-magnetic variables, such as position, velocity, force, etc. Most magnetic field sensors are vector sensors measuring the projection of the field into the sensitive axis, except resonant type sensors which measure the field in scalar value.

Precise magnetic field sensors are those with very high sensitivity and low noise (typically in pico-Tesla level) and they are traditionally used for geophysical and space research [5-10] and biomagnetic measurements [11-16]. New applications in military field and medical industries require extra specifications, for example, high stability against temperature, magnetic shocks, interferences and field gradients.

2.1.1 Emerging Applications

All of the following applications require magnetic sensors with high sensitivity (pico Tesla level) and small size (smaller than centimeters).

1) Physiological monitoring

It is well known that bio-magnetic signals from the heart (MCG) or the brain (MEG) can be detected by magnetometers with ultra-high sensitivity. These signals are in very low frequency range, as shown in Fig. 2.1 and are typically measured using superconducting quantum interference devices (SQUIDs). SQUIDs require cryogens, and are therefore limited in how close to the subject they can get and how many can be deployed effectively in an array. Due to the specific impact and mode of operation, the cost of these systems is not critical. However, if small sized magnetometers are capable of reaching the high sensitivity level, they would have a significant impact. Efforts have been made in combination of giant magnetoresistive sensors (GMR) with superconducting flux concentrators [17]. The objective of current research would be to develop a real-time system with the capability of at least 1 cm source localization. New applications for these devices would be low cost screening systems for routine medical checkups, arrhythmia diagnosis, and advance myocardial electrical diagnosis.

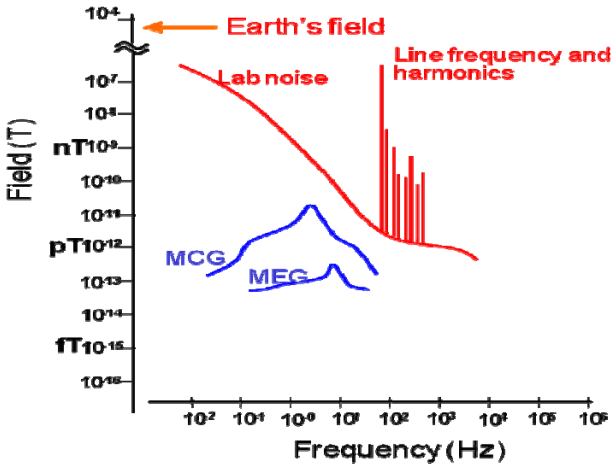

Fig. 2.1 Field range illustrations of MCG and MEG signals [18].

2) Battlefield remote detector[19-22]

This application has the most stringent requirements including high sensitivity, large dynamic range, robust to high ambient fields, low frequency operation, low power consumption, and low cost. In addition, the sensors have to be operated in highly variable environment, i.e. all possible types of terrain, weather conditions, and deployment methods. In general, the stability and reliability of these devices are critical because lives and homeland security are at stake. As shown in Fig. 2.2, the desired resolution of the magnetometers should be at least in pico Tesla level for regular magnetic anomaly detection (MAD) [23-25].

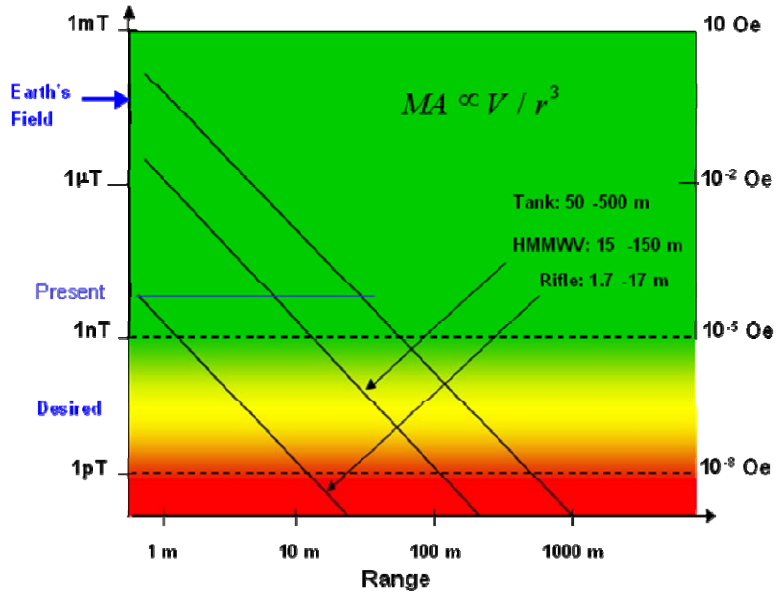

Fig. 2.2 Field ranges for battlefield magnetic anomaly detection [26].

3) Magnetic particles tracer [27-30]

This application of precise magnetic field sensors represent direct competition for the fluorescence tag technique that is used in health care assay applications. The sensors must be packed into a very high density array, and single bead detection is desirable. Similar applications are like bead tracking system which is very promising of studying blood flow in capillaries and organs. The magnetic method can be used in conjunction with other imaging techniques to understand the impact of stroke on cardiac function and the electrical circuits in the heart.

2.1.2 Existing Technologies

The drivers in the military, bio-magnetic and medical applications motivate the research and development of the precise magnetic field sensors. The key features of the precise magnetic field detection are high sensitivity and small size. Currently most

magnetic field sensors are limited by either the bulky size or low resolution. Though SQUID sensors offer adequate high resolution in weak field in most applications, it is difficult and expensive to implement SQUID systems to portable applications due to the cryogenic requirement.

For other room temperature sensors, break through is needed in several directions. For example, fluxgate sensors (parallel type) can reach the top resolution to 10 pT in a range of 10 mT. It is probably the most sensitive magnetometers commonly being used. But the main drawback is their bulk size: typical low-noise sensor has a 20 mm diameter core [31]. Miniaturizing fluxgate sensors and integrating the signal processing and control circuit are still challenging. It is a difficult topic to fabricate a thin film fluxgate with comparable performance compared with its bulky version.

The GMI sensors, seem promising in miniaturization, but still need improvement in resolution and stability. Typical top parameters of such sensor operation with 1-mm-long MI head are: a field resolution of 10^{-6} Oe (0.1 nT) for the full scale of ±1 Oe (0.1 mT), a response speed of 1 MHz, and a power consumption of about 10 mW. The commercial product has a lower resolution of 10 nT.

The MR sensors have great potential in the integration with silicon process. The main obstacles are their low sensitivity and large low frequency noises.

Magnetic sensors can be classified based on the physical phenomena. The common magnetic sensors are the superconducting quantum interference devices (SQUID), magneto-resistors (MR), magneto-impedance or magneto-inductance (MI) sensors, electromagnetic induction sensors (fluxgate and search coil), Hall effects sensors,

magnetostrictive-piezoelectric sensors, fiber-optic magnetostriction sensors, and resonance magnetometers, etc.

2.1.3 Performance Comparison

Specific applications require certain features of the sensors in the detection range, frequency range, operation temperature, power consumption, cost, etc. Table 2.1 shows the typical detection range of existing magnetic field sensors. Table 2.2 shows the comparison of magnetic field sensors in terms of resolution, frequency range, size, cost, notable advantages and disadvantages.

Table 2.1 Detection field range of existing magnetic sensor technologies

Magnetic Sensor Technology	Detectable Field Range (Tesla)
	10^{-12} 10^{-8} 10^{-4} 10^{0} 10^{4}
SQUID	
Magneto-Optical Sensor	
Hall-Effect Sensor	
Nuclear Procession	
Search Coil*	
Earth's Magnetic Field	
Anisotropic Magnetoresistive(AMR)	
Giant Magnetoresistive (GMR)	
Tunneling Magnetoresistive (TMR)	
Giant Magneto-impedance (GMI)	
Parallel Flux Gate	

*Search coil is kind of ac magnetic field sensor.

Table 2.2 Magnetic Field Sensor Comparison ([4, 15, 26-27, 31-36])

Sensor type	resolution	Frequency Range	Minimum sensor size/ Scalability	Cost	Advantages	Disadvantages
Search coil	30 fT	>1 Hz	1 mm	Moderate	Low cost for the sensitivity	Limited to > 1Hz, sensitive to angular vibrations, Loose sensitivity as decrease size
Hall probe	100 nT	< 1kHz	< 1μm	Moderate	Large range, linear	Temperature dependent
Fluxgate	10pT	< 1kHz	Loose S/N scaling down	Moderate	High sensitivity	Cost, size, energy consumption
SQUID	1 fT	<1kHz	< 1μm (system large)	Expensive	Sensitivity	Need for low temperature
AMR	50 – 100 nT	0-5 GHz	< 1μm	Moderate	Lower 1/f noise	
GMR	20 nT	0- 5 GHz	< 1μm	Cheap	Low cost in large quantities	
TMR	1 nT	0-1 GHz	< 1μm	Cheap	Large MR, low cost in large quantities	High 1/f noise, hysteretic
GMI	100 pT	<500 kHz	1 mm	Moderate		Cost, size, high power
Magneto-optic	100 pT	0-5GHz	0.1 mm	Moderate	No electrical connection	
Optical pumping	10-1000 fT	< 100 Hz	10 mm	Expensive	Insensitive to angular vibrations	Cost, power consumption, loss of sensitivity at higher frequencies
Magnetostrictive/ Magneto-electric	1 nT		10 μm	Moderate	Low power Large output voltage	Sensitive to vibrations

2.2 Parallel Fluxgate Sensor

Fluxgate sensors are the widely used precise magnetic sensors measuring the dc or low-frequency ac magnetic field in vector form. Most fluxgate sensors are parallel type, which means the excitation field is in the same direction with the measured field. When the excitation field is in orthogonal direction to the measured field, the sensor is called orthogonal fluxgate, which will be introduced in next section. There are also a few types of helical fluxgate sensors in which the excitation field is in an angle to the measured field.

The state-of-the-art parallel fluxgate magnetometers can detect the field in the range of up to 1 mT with the resolution down to 10 pT [4] and has been equipped in a series satellites for geomagnetic field exploration, i.e. Danish Ørsted 1999, German CHAMP 2000, and European Space Agency SWARM 2010 [37]. Table 2.3 lists the features of fluxgate sensor in top values and standard values. Note that normally only some top values can be achievable for a single sensor. There is no such a fluxgate sensor satisfying all the top parameters.

The sensing element used in this kind of sensors is the amorphous metal materials of ring-core type with very low noise and high thermal stability [38]. However, the core shape limits the further miniaturization of the magnetometer and low power portable applications.

Table 2.3 Features of Fluxgate sensors [33]

Fluxgate sensor parameters	Top value	Standard value
Range	10mT	200μT
Linearity error	10ppm	100ppm
Temp. coeff. of Sensitivity	<0.05nT/^{0}C	0.2nT/^{0}C
Perming	<1nT offset after 10mT shock	<5nT
Noise	5pT rms (0.05-10Hz)	100pT rms
Long-term Stability of offset	2nT/yr	5nT/8hrs
Bandwidth	10kHz	20Hz
Operating Temp. Range	-60^{0}C- +200^{0}C	-20^{0}C- +70^{0}C
Power consumption	1mW	100mW
Size	2mm	30mm
Crossfield error	<1nT for 50μT field	5nT

2.2.1 The Fluxgate Principle

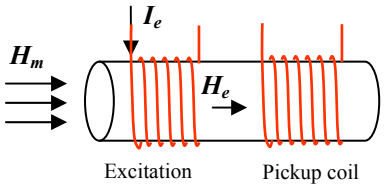

Fig. 2.3 Basic parallel fluxgate sensor setup.

The basic parallel fluxgate sensor setup, as shown in Fig. 2.3, consists of a sensing core of ferromagnetic material, an excitation coil, and a pick-up coil. The sensing core is excited by an ac magnetic field H_e generated by the excitation coil. The amplitude of the excitation field has to be large enough to saturate the sensing core. At the pick-up coil output, a pulse wave appears due to the induction through the magnetic core.

Without any external magnetic field, the pulse wave of the pick-up coil output is symmetrical, and it contains only odd harmonics of the excitation frequency. When an external magnetic field H_m to be measured is applied, there will be an offset in the waveforms of the total magnetic field (H_e+H_m), causing phase shift of the magnetic induction, and the pick-up coil output waveforms as shown in Fig. 2.4. As a result, even harmonics due to the asymmetry of the pulse appear. Since the second harmonic has the largest amplitude among even harmonics, the readout electronics usually tune to the second harmonic for the signal extraction. The amplitude of the second harmonic is proportional to the external magnetic field if the external magnetic field is sufficiently smaller than the saturation magnetic field of the sensing core. The amplitude of the second harmonic is also proportional to the excitation frequency in the frequency range where the frequency response of the ferromagnetic core is flat [39].This property is based on the fact that the induced voltage at the pickup coil output is proportional to the derivative of the magnetic induction.

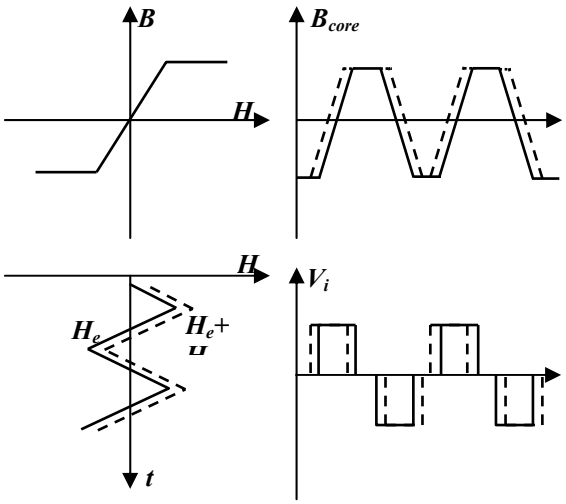

Fig. 2.4 Basic parallel fluxgate working principle

2.2.2 Modeling of BH loops

Fluxgate modeling consists of the magnetic properties of the materials and fluxgate effect induced in operation. In this section the key problem on how to model the hysteresis loops, or BH curves of the sensing element is discussed.

BH curves are closely related to the magnetization curves, which are the macroscopic description of the magnetization of materials [40]. The initial part of the magnetization curve satisfies the Rayleigh relation [41]

$$B(H) = \mu_0(\mu_i H + bH^2) \tag{2.1}$$

where μ_0 is the permeability of vacuum, μ_i is the initial permeability and b is known as the Rayleigh constant. However, the initial permeability can only be obtained from the "zero" state of the material when the net magnetization is zero, which is difficult to satisfy. In practical application, maximum permeability or incremental permeability which are easily calculated from BH loops are used.

An idealized, completely reversible anhysteretic magnetization model was given by Brillouin equation [42]

$$\frac{M(H)}{M_s} = \frac{2J+1}{2J}\coth(\frac{2J+1}{2J}\frac{H}{a}) - \frac{1}{2J}\coth(\frac{1}{2J}\frac{H}{a}) \tag{2.2}$$

where M_s is the saturation magnetization, J is the quantum number of the atom and a is the shape parameter of the material. Based on this theoretical model, some approximations had been made and BH curves were modeled [43-46]. In these models, the permeability is defined as the slop of the BH curves at origin point.

2.2.3 Modeling of Parallel Fluxgate Effect

With the assumption of constant pickup coil area, the induced voltage in the pickup coil in a basic parallel fluxgate can be

$$V_i = -\frac{d\Phi}{dt} = -NA\mu_0\mu_r \frac{dH_m(t)}{dt} - NA\mu_0 H_m \frac{d\mu_r(t)}{dt} \tag{2.3}$$

where N is the number of turns of the pickup coil, A is the cross-sectional area of the sensing core, and μ_r is relative permeability. The basic induction effect (first term) is still present in fluxgate sensors causing interference. The second term is caused by fluxgate effect in which the core permeability is periodically changing with the excitation field. In some types of fluxgate using ring-core sensing element, demagnetization effect has to be considered and the fluxgate voltage output becomes more complex,

$$V_i = NA\mu_0 H_m \frac{1-D}{\{1+D\mu_r(t)-1\}^2} \frac{d\mu_r(t)}{dt} \tag{2.4}$$

where D is the demagnetization factor of the sensing element. According to the Fourier analysis of the induced voltage waveforms, the second harmonic voltage is given by

$$V_2 = \frac{8NA\mu_0\mu_r^* H_e f}{\pi} \sin\frac{\pi\Delta H}{H_e} \sin\frac{\pi\Delta H_m}{H_e} \tag{2.5}$$

where f is the excitation frequency, μ_r^* is the effective relative permeability, and

$$\Delta H = \frac{2B_s}{\mu_0\mu_r^*} \tag{2.6}$$

where B_s is the saturation magnetic flux density. Normally the measure field $H_m << H_e$, the second harmonic sensitivity is given by

$$S = 8NA\mu_r^* f \sin\frac{\pi\Delta H}{H_e} \tag{2.7}$$

2.3 Orthogonal Fluxgate Sensors

In this section, firstly, we introduce several aspects of the orthogonal fluxgate sensors including set-ups, sensing materials, and working principles. Then performance of orthogonal fluxgate reported in literatures are summarized and analyzed. Finally several popular models and theories on orthogonal fluxgate are presented.

2.3.1 Introduction

Most fluxgate sensors are of parallel type, which means that the direction of excitation field H_e and the measured field H_m is the same. If the direction of H_e is perpendicular to that of H_m, then this type of sensors is called orthogonal type fluxgate [47]. The orthogonal fluxgate mechanism was first proposed by Palmer in 1953 [48]. Two configurations of orthogonal fluxgate were patented by Alldredge in 1958 [49], shown in Fig.2.5, the sensing cores were ferromagnetic wire or tube. A mixed orthogonal-parallel type was proposed by Schonstedt [50]. In practice, the sensing elements used in these early designs were bulky ferromagnetic rod or tube [47]. Also, electrodeposited permalloy films on cylindrical copper rod was suggested by Gise [51]. The orthogonal fluxgate sensors have not been widely used for the generally poor performance compared with parallel type fluxgate. But with the development of the fabrication technology of ferromagnetic micro-wires, this kind of sensor is re-discovered in recent years for its great potential of low power, high sensitivity and

miniaturization. The sensing elements normally used are ferromagnetic amorphous wires [52-53] and permalloy nanocrystalline wires, as shown in Fig. 2.6. New materials with specifically designed properties have been used in the recent development of orthogonal fluxgate, for example, ribbons with sandwich structure [54], ribbons with U-shape [55], and CMOS compatible electroplating permalloy [56], etc.

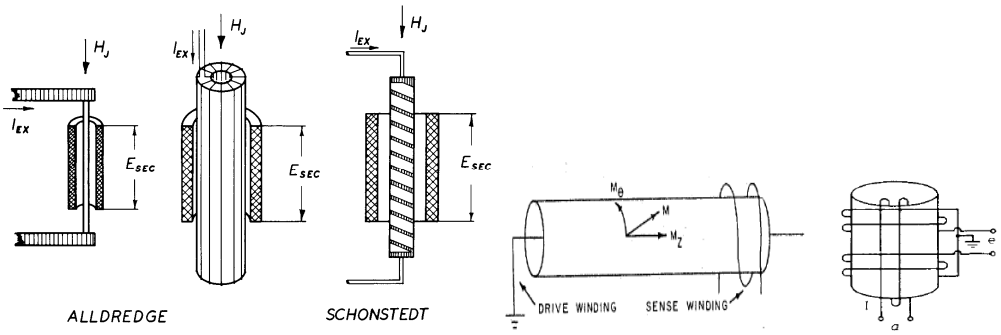

Fig. 2.5 Traditional orthogonal Fluxgate sensors [47, 51-52]

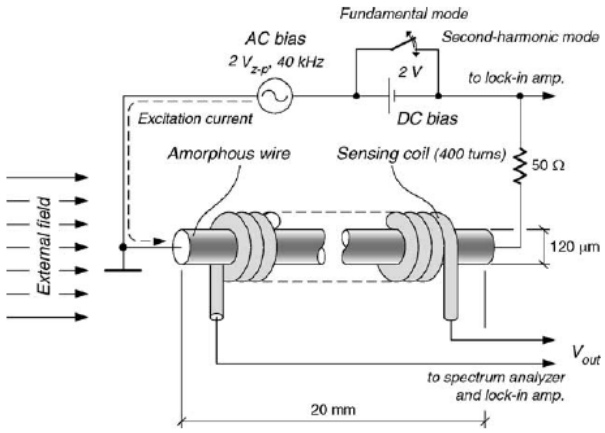

Fig. 2.6 Recent orthogonal fluxgate sensors in [57].

The conventional working mode of orthogonal fluxgate sensors is 2nd harmonic mode which was based on bipolar periodic saturation of the sensing core by the

excitation field and the output signal proportional to the measured DC field is on the second harmonic frequency of the excitation. The working mode of the orthogonal fluxgate sensors has been extended at the early 21st century. It was observed that if the excitation field contains DC component and it is adjusted to saturate the core only in one polarity, the output signal appears at the first (fundamental) frequency [57]. It was demonstrated that sensor working in such mode may have significantly lower noise, but the disadvantages are the degradation of the offset stability [58] and increased power consumption due to the additional bias current. Flipping the DC bias field may restore the stability, but it is paid by more complicated sensor design and again increased power consumption [59]. In fact this technique is equivalent to double-frequency excitation.

2.3.2 Performance of the Orthogonal Fluxgate Sensors

Performance comparison of the orthogonal fluxgate is given in Table 2.4, in respect to the resolution, frequency range, noise level, and sensor head size. Previous orthogonal fluxgate used tubular cores as the sensing elements, which had large volume [36, 51]. They also suffered from larger noise level, which may probably due to the quality of materials. Recently, new designs with ferromagnetic micro-wires provide high sensitivity and low noise level, as well as the great reduction in sensor size which makes orthogonal fluxgate a hot topic in the fluxgate sensor community. However, compared to the advanced parallel fluxgate, the orthogonal fluxgate has a large space for improvement in the resolution, noise level and stability.

Table 2.4 Comparison of performance of orthogonal fluxgate sensors in literature

	Resolution /Sensitivity	Frequency (Hz)	Noise level	Size(mm)	Remarks
Candidi [36]	-	0.02-5	0.26nT	d_o=4,d_i=3.8 L=144	Tubular core
Gise [51]	-/50mV/ μT	DC	-	D=6.35, L=63.5	Rod core
Sasada [57]	-/230mV/ μT	<51	0.1nT/rtHz@10Hz	D_w=0.12, L=20	Wire core
Papersno [58]	0.1nT/1.1mV/μT	<4.9	10pT/rtHz@2Hz	D_w=0.12, L=20	Wire core
Goleman[55]	121 mV/ μT	<200	50 μT/rtHz@10Hz	1x0.015, L=50	Ribbon
Zorlu [56]	510μV/mT	10	95nT/rtHz@1Hz	Dw=0.016x0.01 L=1	Rod core
Aichi sensor [60]	5nT/1600mV/μT	0.3-5	-	D_w=0.02, L=1	Wire core
				1 x 0.5	Pickup coil

The earliest explanation of orthogonal fluxgate mechanism was given by Primdahl [47], using the geometrical model, which showed validation by the experimental results. But it had an assumption that the material must be isotropic, which is not true in most cases. Recently new approaches including magnetization rotation and surface magnetoimpedance tensor have been developed. Also, some people regard the orthogonal fluxgate as an extended Inverse Wiedeman Effect. The following is a brief review of these theories, as well as their applicability and limitation.

2.3.3 Classical Model

The first theoretical discussion of orthogonal fluxgate sensors was proposed in [48]. A geometrical model was established based on Alldredge tubular sensor made of a kind of ferrite material (Permax 35) [47], which was regarded as isotropic materials. The circular scalar permeability μ, is calculated by

$$\mu = B_z / H_z = B_\theta / H_\theta \approx B_{sat} / H_\theta \tag{2.8}$$

for large H_θ, as shown in Fig. 2.7. Note that this result is based on the assumption of collinearity between B_{RES} and H_{RES}. When hysteresis concerned, the permeability could be corrected to

$$\mu = \frac{B_\theta}{H_\theta \pm H_c} \tag{2.9}$$

Considered the demagnetizing factor D of the tube, the net field in longitudinal direction is

$$H_z = H_m \frac{1}{1 + D\mu} \tag{2.10}$$

where H_m is the external field. Thus, the net permeability in longitudinal is

$$\mu_z = B_z / H_m = \frac{B_\theta / (H_\theta \pm H_c)}{1 + DB_\theta / (H_\theta \pm H_c)} \tag{2.11}$$

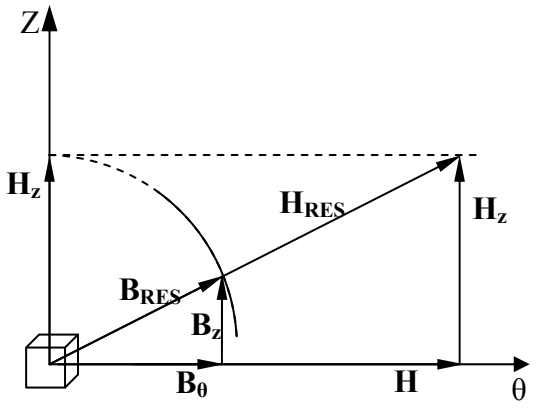

Fig. 2.7 Geometrical Model explaining $B_z/H_z=B_\theta/H_\theta$.

This is the expression of the gating curve (μ_z-B_θ) and could be obtained by experimental method, or by calculation from the circumferential B_θ-H_θ loop.

The geometrical model explained the gating curves fairly well but had essential limit for sensors with anisotropic sensing cores, for which the permeability cannot be taken as a scalar. However, in the cases when the material has moderate anisotropy, this model is sufficient.

2.3.4 Magnetization Rotation Model

A magnetization rotation model in the framework of quasi-static Stoner-Wohlfarth approximation was discussed by Antonov [61]. The theoretical analysis is given based on the assumption of single domain sensing element working in relatively low frequency. The setup is same with Fig. 2.6. Neglecting edge effects, the magnetic free energy density U of the micro-wire as a sum of the anisotropy energy and Zeeman energy in the fields He and H_φ.

$$U = (MH_a/2)\sin^2\vartheta - MH_m\sin\vartheta - MH_\varphi\cos\vartheta \tag{2.12}$$

where H_a is the anisotropy field. Consider $m_z = M_z/M = \sin\vartheta$, $m_z = (1-m_\varphi^2)^{1/2}$, and $\rho = 2r/d$, by minimization of the free energy we can obtain the solution $m_\varphi = m_\varphi(\rho,t)$. Since the expression of output voltage V_φ from the pickup coil can be derived from Faraday's Law,

$$V_\varphi = -\frac{8\pi^2 N}{c}\int_0^{d/2}\frac{dM_z}{dt}rdr \tag{2.13}$$

where c is the velocity of the light, d is the amorphous metallic nucleus diameter, N is number of turns of the pickup coil, M_z is the longitudinal component of magnetization, we can get,

$$V_{\varphi} = V_0 h_0 \cos(\omega t) \int_0^1 \frac{m_{\varphi}^2 (1 - m_{\varphi}^2) \rho^2 d\rho}{h_e m_{\varphi}^3 + h_0 \rho \sin(\omega t)(1 - m_{\varphi}^2)^{3/2}} \tag{2.14}$$

where $V_0 = 2\pi^2 d^2 NM\omega / c$, $h_0 = 4I_0 / cdH_a = H_0 / H_a$, $H_0 = 4I_0 / cd$, $h_e = H_m / H_a$.

I_0 is the driving current amplitude, H_m is the external field.

The V_φ depends on I_0 and H_m. With the increase of I_0, V_φ will increase to a certain amplitude and keep for a long range, then decrease slowly. V_φ rises dramatically in small H_e and then drops much slower. This conclusion shows a good consistence qualitatively with the experiment results.

Similar model is shown by Sasada [53] and Paperno [58], but only with a qualitative analysis. This model explained the possibility of suppression of the noise level by using unipolar magnetization instead of bipolar magnetization.

One of the drawbacks of this model is that it assumes the wire has single-domain structure, which is the ideal case and not always true in the reality. On the other hand, this model is the coherent rotation model, a kind of static magnetization, which does not consider the time parameter in the magnetization process. Actually based on ferromagnetic magnetism, a dynamic magnetization process appears and magnetic-after-effect occurs under the high frequency alternative magnetic field [40].

2.3.5 Off-diagonal Giant Magneto-impedance Model

The traditional GMI, which could be looked as a high frequency analogy of giant megnetoresistance, is not only non-linear with a symmetric output, but also unsuitable for sensing in near zero-field region. Thus, a differential structure and dc bias fields

are needed to obtain the linearity [27], which increase complicacy and power consumption of the device [14].

Off-diagonal MI is observed from the same sensor setup as the orthogonal fluxgate sensor [62]. Thus, some people considered the orthogonal fluxgate as a kind of off-diagonal GMI effect [63-64]. The linearity of output voltage in weak field range is the great advantage over traditional GMI.

Off-diagonal MI is really an extension of the GMI theory, which could cover all of the electromagnetic effects in the current driven magnetic materials, especially in wires. As seen in Fig. 2.8, the sample is exited by an ac current, the voltage signal measured across the wire, V_w and in the coil, V_c, represent the GMI and off-diagonal GMI effect, respectively. A concept of surface impedance tensor is developed to explain this phenomenon [65-68].

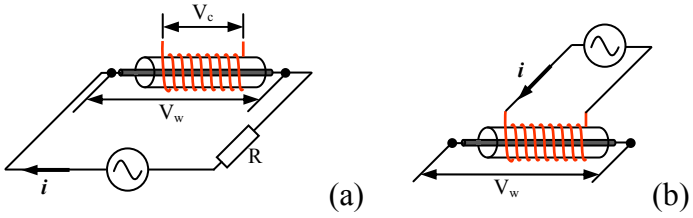

Fig. 2.8 Voltage outputs in GMI and off-diagonal GMI setup [37]

The GMI takes into account of the eddy current effect, so the model deals with the surface impedance. The output response (V_w, V_c) in a magnetic wire is related to the surface impedance tensor ς in the following forms

$$V_w \equiv e_z l = \left(\varsigma_{zz} \frac{i}{2\pi a} - \varsigma_{z\varphi} h_{ex} \right) l \tag{2.15}$$

$$V_c \equiv e_\varphi 2\pi a n_2 l = \left(\varsigma_{\varphi z} \frac{i}{2\pi a} - \varsigma_{\varphi\varphi} h_{ex} \right) 2\pi a n_2 l \tag{2.16}$$

where l is the wire length, a is the wire radius, $h_{ex} = n_1 \tilde{i}_c$, n_1 and n_2 are the numbers of turns per unit length in the excitation and pickup coils, respectively. e_z and e_φ are electrical fields in longitudinal and circumferential direction, respectively.

Thus, the impedance tensor $\hat{Z}$ can be derived

$$\hat{Z} = \begin{pmatrix} Z_{zz} & Z_{z\varphi} \\ Z_{\varphi z} & Z_{\varphi\varphi} \end{pmatrix} = \frac{(1-j)R_{dc}a}{2\delta} \cdot \begin{pmatrix} \sqrt{\mu_{eff}} \sin^2\theta + \cos^2\theta & -2\pi a n_1 (\sqrt{\mu_{eff}} - 1)\sin\theta\cos\theta \\ 2\pi a n_2 (\sqrt{\mu_{eff}} - 1)\sin\theta\cos\theta & -(2\pi a)^2 n_1 n_2 (\sqrt{\mu_{eff}} \sin^2\theta + \cos^2\theta) \end{pmatrix} \tag{2.17}$$

where R_{dc} is the dc wire resistance, δ is the skin depth of the high frequency ac current, μ_{eff} is the ac effective circular permeability with respect to the equilibrium magnetization M_0 in the wire surface, M_0 inclines toward the wire z axis by an angle θ.

Theoretically 4 kinds of voltage outputs can be obtained in the MI system from the above equation. Thus, the concept of MI tensor provides explanations to both traditional MI effect and orthogonal fluxgate (off-diagonal MI), and moreover, the parallel fluxgate.

The MI model is also based on the single domain and helical equilibrium magnetization similar to the coherent magnetic rotation model, but it is a more general form. A more detailed discussion could be the expression of the permeability tensor.

For the wires with multi-domain states, no off-diagonal MI has been reported, and this issue is still under study.

2.3.6 Inverse Wiedemann Effect

Another attempt is to explain orthogonal fluxgate phenomenon is to treat it as the Inverse Wiedeman Effect (IWE). IWE initially [69] was named for the phenomenon: when the tubular magnetic materials are twisted with the axis, the longitudinal applied field will give rise to the circumferential magnetization. But people later extend the IWE to include the effect: when tubular magnetic materials are twisted with the axis, the applied circumferential alternative field gives rise to longitudinal alternative magnetization [70-75]. All of these experiments were made on the magnetic wires under torsion or after stress annealing, which indicated that the effect was related to the magnetostriction. A theoretical analysis based on coherent magnetization rotation with consideration of magnetoelastic energy was presented in [70]. Vazquez [73] concluded the reason for IWE is the helical anisotropy which could be induced by torsional strain or heat treatment in the presence of torsion stress.

Though extended IWE takes into account the effect of magnetostriction, the model is a full-scale consideration including Zeeman energy, magnetocrystalline and magnetoelastic energy, which is similar to the one in section 2.3.4.

From IWE, we can notice that behind MI tensor is the permeability tensor, which actually represents the cross magnetization process. Furthermore, the permeability tensor is dependent on the magnetic properties of the material, such as anisotropy and domain structure. Therefore, the proper preparation and accurate characterization of materials are essential to the sensor development.

2.4 Noise in Fluxgate Sensors

Sensor noise in the fluxgate magnetometer is regarded as a substantial source of errors and must be seriously considered. The two basic classification of noise for the magnetic sensor system are inherent (or intrinsic) noise and interference (or extrinsic) noise.

Extrinsic noise is induced from an external source and can cause unsatisfactory operation of the device. The interference of sources of noise occurs by means of coupling from conductance, capacitance, magnetic field, radiation, and power line. Magnetic noises may come from the ferromagnetic materials used in the lab or the magnetized objects outside the lab, or from the induced field by the large current in the equipments, or from the variation of the earth's magnetic field caused by the unstable geographical poles or even by the solar wind (magnetic storm) [4].

In case of orthogonal fluxgate sensors, the intrinsic noises have three main sources: thermal noise, flicker noise (or contact noise) and magnetic Barkhausen noise.

The limiting noise of a single domain flux gate sensor would be the thermal equilibrium magnetic fluctuation of the core material [76]. In practical realization of a sensor, other less fundamental sources of noise may be overwhelming [77]. They include nonequilibrium magnetic Barkhausen noise driven by the magnetic fields which alternately saturate the core in opposite directions and noise from the electronic circuits which record the magnetic signal from the sensor [78].

2.4.1 Thermal equilibrium

The spectral power density of the thermal noise is independent of frequency f [47],

$$e_n = 2\sqrt{k_B T R \Delta f} \tag{2.18}$$

where k_B is the Boltzmann constant, R is the resistance of the pick-up copper coil, T=300 K in the room temperature, Δf = 10 Hz. e_n corresponds to a noise equivalent input field of $B_n=e_n$/Sensitivity. In our sensors, with a pickup coil of 1000 turns, the resistance is around 19Ω and the normal initial sensitivity is around 10 μV/nT, so

$$e_n = 2\sqrt{1.38\times10^{-23}\times300\times19\times10} = 1.77\times10^{-9}V$$

$$B_n = 0.18\text{pT}$$

2.4.2 Flicker noise

Flicker noise, or contact noise, occurs in almost all electronic devices, and results from a variety of effects, such as impurities in a conductive channel, generation and recombination noise in a transistor due to base current, and so on. It is always related to a direct current. Flicker noise is a low frequency noise and its spectral density is roughly proportional to 1/*f*. It is always pronounced at frequencies below 100 Hz, where our sensor system operates, so it seriously impairs the performance of the system.

2.4.3 Barkhausen noise

Barkhausen noise comes from the changing magnetization by the excitation current. It is reported that the Barkhausen noise is closely related to the composition of the sensing element. In our case, the CoFeSiB amorphous wires used as the sensing

element has quite low noise compared with NiFeSiB alloy [79]. The Barkhausen is proportional to f-α where α goes from 0.6 to 1.5 in the low frequency range normally considered for magnetometers. Normally the Barkhausen noise is about 1-2 orders of magnitude larger than thermal noise. So, the Barkhausen noise is probably at least several pico Tesla. It is reported that by dc biasing through the sensing wire, the Barkhausen noise could be reduced greatly [58].

2.5 Materials Used for Fluxgate Sensors

Different materials respond to the applied magnetic field in different ways that determine the sensor types and related characteristics. These responses include magnetic, electrical, caloric, optical, and magnetorstrictive effects, etc, or the combination of them. For fluxgate sensors, the mechanism of the field responses is the magnetization process of the materials presented in the combination of a high frequency excitation field and a low frequency external field. Hence, the magnetic properties of the materials are pivotal for the sensor performance.

Characterization of the material's magnetic properties normally is the preliminary requirement of the sensor design. The magnetic properties of materials, especially ferromagnetic materials, can be categorized into intrinsic and extrinsic properties. The intrinsic properties, including Curie temperature, saturation magnetization, magnetocrystilline anisotropy, magnetostriction, etc, present the inherent characteristics of the materials. These properties are derived from the composition and crystalline structure and are independent with defects, grain size, post treatment, and external field.

The extrinsic magnetic properties, like permeability, susceptibility, remanent magnetization, coercivity, etc, are derived from magnetization curve or hysteresis loop, which could be affected by the defects, grain alignment, fabrication, and post treatment of the materials.

2.5.1 General Requirements

General requirements of the materials are:

1. High permeability and low coercivity, non-rectangular shape of the magnetization curve is preferred;
2. Low number of structural imperfections, low internal stresses, uniform cross-section, smooth surface and high homogeneity of the parameters;
3. Low magnetostriction;
4. Low saturation magnetization and high electrical resistivity.

Thus, the specific materials used for fluxgate sensors include semiconductors, superconductors, single crystal metals, nanocrystalline alloys, amorphous alloys, etc. The structures of the materials can be wires, films, multilayers, etc.

The ferromagnetic micro-wires are good candidates for the micro magnetic sensors application benefiting from their superior magnetic properties, i.e. high permeability, low coercivity, small size, and uniformity. The micro-wires can be fabricated by various technologies. Totally three kinds of micro-wires are used for the orthogonal fluxgate development in this project. The CoFeSiB amorphous wires were fabricated by in-rotating-water quenching method [80-81], the CoFeSiB GCAWs were fabricated by Taylor-Ulitovsky method [82], and the NiFe/Cu CWs were prepared by electrodeposition [83-84] .

2.5.2 Domain Structures of GCAWs and CWs

2.5.2.1 GCAWs

Due to the internal stresses induced in the fabrication process, the anisotropy of the GCAWs with near zero magnetostriction is complicated. In the inner core (IC) of the wire, the anisotropy is in radial direction according to [85], while other researcher reported axial anisotropy in IC [86]. Nevertheless, the anisotropy of outer shell (OS) of the wire was found in circumferential direction and the anisotropy constant is dependent on the thickness of the glass coating layer, as shown in Fig. 2.9.

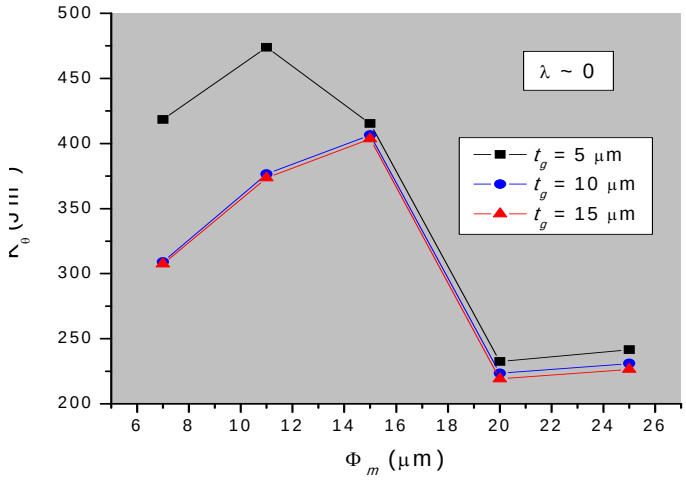

Fig. 2.9 Dependence of circumferential anisotropy constant on metallic core diameter for $Co_{68.15}Fe_{4.35}Si_{12.5}B_{15}$ amorphous glass-covered wires, with the glass coating thickness as a parameter. [87]

One proposed domain distribution of the GCAWs with negative and near zero magnetostriction is shown in Fig. 2.10. The domains in IC are with radial anisotropy and the domains in OS are with circular anisotropy. However, the direct observation of the domains in such kind of wires has not been reported.

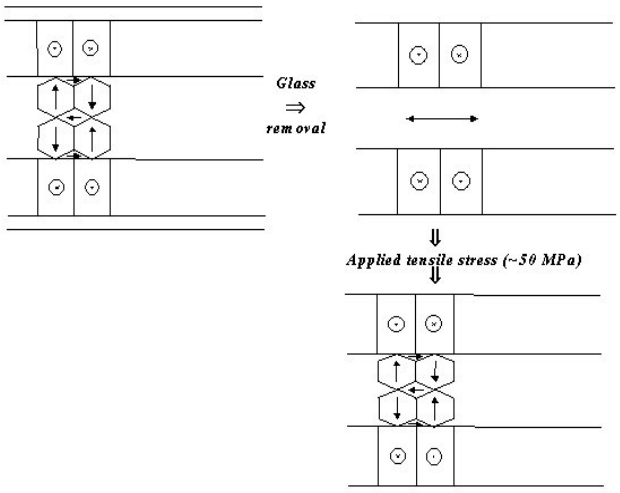

Fig. 2.10 Domain distribution of the GCAWs with negative and near zero magnetostriction [85].

2.5.2.2 Composite micro-wires

For electroplated NiFe/Cu composite wires, it was revealed using method of scanning Kerr microscopy, that in the near-surface range of the CWs, there are circular domains with the alternating left- and right-handled magnetization in the adjacent domains [88], as shown in Fig. 2.11.

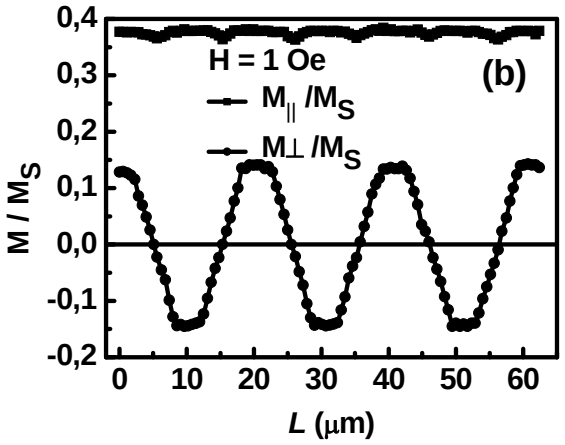

Fig. 2.11 The typical distributions of $M_{\parallel}(L)$ and $M_{\perp}(L)$ observed in the typical NiFe/Cu CWs wires [88].

2.5.3 Interaction between ferromagnetic micro-wires

For typical micro-wires system, magnetostatic interactions have been studied thoroughly in Fe-rich amorphous wires with axial bistability [89-94] and Co-rich amorphous wires with circular bistability [91, 95-96]. Dipolar interactions, arising from domain walls, surface defects, or wire end domains [93], were generally believed dominant in the micro wire system, though nondipolar contributions were reported not negligible [92]. Moreover, recent studies showed that for the micro-wires closely placed in a linear array, the simple dipole approximation in which the whole wires were treated as dipoles is not valid [94]. Instead, a more complex model concerning multipolar field contributions has to be considered [94, 96].

The intrinsic mechanism of such interactions was not fully understood because of: 1) the structure complexity of the array that contains a large number of magnetic entities and the magnetization state of each entity depends on their neighbors, and 2) the dynamic nature of magnetization reversal process in the entities when they are used as the sensing array driven by an alternative current [97], which was not clearly understood.

2.6 Summary

Research and development of precise magnetic sensors with high sensitivity, low noise, and small size are driven by the emerging applications in the biomagnetic, military, and medial fields. Among the existing sensor technologies, orthogonal fluxgate is one of the most promising sensors to be miniaturized. Different from

parallel fluxgate, orthogonal fluxgate needs no excitation coil. An excitation current flows into the sensing element and the induced field magnetizes the material in orthogonal direction. Similar to parallel fluxgate, a pickup coil is used to transduce the magnetic field information to voltage by Faraday's law. In the readout, the low frequency magnetic field was demodulated traditionally from the second harmonic of the induced voltage. The sensitivity depends on the working conditions and magnetic properties of the sensing element.

In orthogonal fluxgate, theoretical studies have modeled the sensing element with simplified magnetic properties, either by isotropic approximation or single domain structure. Experimental studies of the orthogonal fluxgate have introduced new operations and materials. Fundamental working mode has been found to have less noise than the 2^{nd} harmonic mode as long as applying an additional dc current into the sensing element. Various soft ferromagnetic materials in the forms of ribbon, wire, thin film have been used as the sensing element, among which the non-magnetostrictive micro-wires are the most favorable due to their good and stable magnetic properties and uniform shape. CoFeSiB GCAWs fabricated by Taylor-Ulitovsky method and NiFe/Cu CWs fabricated by electrodeposition are such typical wires. Intensive studies have revealed that the magnetic domains of the GCAWs are in core-shell structure with the outer shell in circumferential anisotropy while CWs were found with a helical anisotropy. The interaction between micro-wires has been studied focused on the magnetostrictive wires with large Barkhausen jump. The dipolar interaction model has been established.

A survey on newly developed fluxgate sensors showed that the state-of-the-art fluxgate are still in parallel type. The main challenge for parallel fluxgate is to reduce the size while maintaining the high performance. Several attempts in orthogonal fluxgate still focused on the improvement of single sensing element.

In general, the orthogonal fluxgate effect of multi-core structure is a novel approach to the high performance sensor development. Both theoretical and experimental studies may pave a new direction of magnetic sensor research and development and contribute significantly to the academic community and industry.

Chapter 3
Research Approach and Experimental Setups

3.1 Research Approach

The research approach implemented in this study to accomplish the project objective, which is to investigate the extreme of the sensitivity and noise of orthogonal fluxgate sensors, is an iterative and interactive process consisting of four modules: material design, material characterization, device development and testing, and modeling, as shown in Fig. 3.1. Firstly the novel multi-core sensing element based on the ferromagnetic micro-wires has to be designed and fabricated regarding to their composition, dimension, and structure. Secondly the magnetic properties of the multi-core sensing element have to be characterized including static and low frequency hysteresis loops measurement using vibrating sample magnetometer (VSM) and induction method, respectively, high frequency property investigation using magnetoimpedance (MI) effect, and dynamic sensing property measurement using orthogonal fluxgate response. Thirdly the performance of the developed multi-core orthogonal fluxgate sensor has to be tested in respect of sensitivity, noise level, power consumption, temperature stability, etc. This step-by-step procedure has always been accompanied by multi-core orthogonal fluxgate modeling which focuses on the domain structure of the micro-wires, permeability of the sensing element, and magnetic interaction between multiple wires in the sensing element. The modeling study is trying to interpret the observed phenomenon and understand the physics

behind it based on the results from the three steps and also works as a feedback to guide the design of the multi-core sensing element.

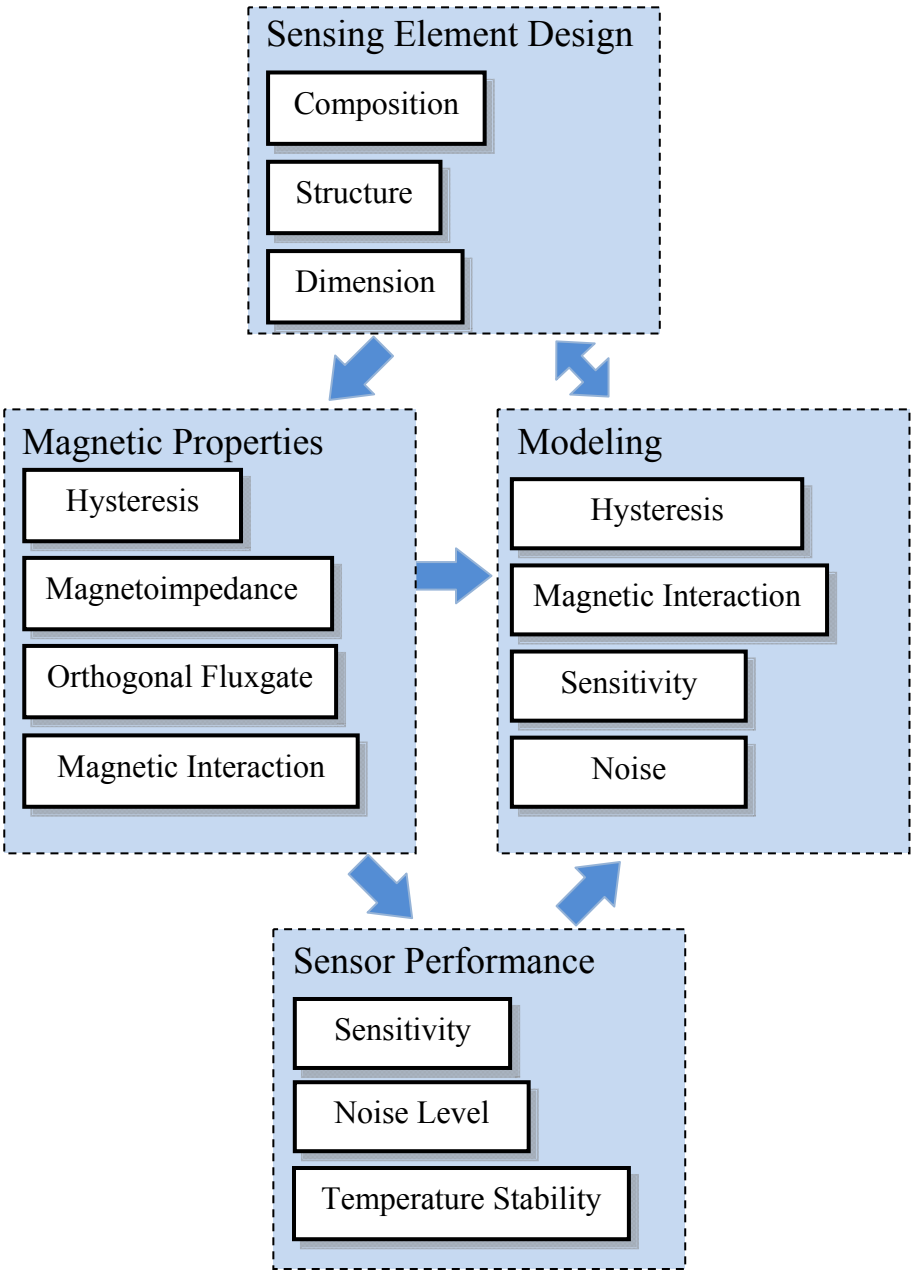

Fig. 3.1 Flow chart showing the research approach used in this project including material design of the sensing element, material characterization of the magnetic property of the sensing element, device development and performance testing, and modeling of the material and device.

In this chapter the experimental setups of the magnetic property characterization and sensor performance measurement have been described.

3.2 Introduction

Magnetic properties of materials include intrinsic properties and technical properties. Intrinsic properties are determined by the chemical composition and crystalline structure of the material, including curie temperature T_c, saturation magnetization M_s, crystal anisotropy constant K_u, magnetorestriction λ, etc. Technical properties depend on the microstructure of the material, including permeability μ, susceptibility χ, remanent magnetization M_r, and coercivity H_c, etc. which can be obtained by magnetization curves and hysteresis loops measurement. The technical properties are essential for the sensor performance and they are affected by impurities, defects, grain size, grain arrangement, shape, and post treatment of the specimen.

For the ferromagnetic micro-wires studied in this project, due to their cylinder structure these technical parameters are all in form of tensors, i.e. they are all direction sensitive. Their values in axial and circumferential directions may be very different. Conventional characterization tools for example, VSM and induction method used for hysteresis loops measurement, are all orthogonal coordinated and can only be used for the measurement in axial or transverse direction. Therefore new characterization tool has to be developed to measure in circumferential direction. In this project, a hysteresis loop tracer capable of measuring hysteresis loops of multi-core sensing elements in both longitudinal direction and circumferential direction has been

designed and fabricated. Magnetic parameters M_s, M_r, μ, and H_c can be derived from the measured data using the hysteresis loop tracer.

Noted that the hysteresis loops provide the static or low frequency properties of the material, in most cases, the sensing elements are working at frequency ranging from tens of kHz to a few MHz. Therefore, magnetic properties of the multi-core sensing element at high frequency have to be characterized. For this purpose, magneto-impedance effect and gating curve have been used, which can provide frequency response of the materials with additional information on anisotropy and permeability.

3.3 Magnetic Property Characterization

3.3.1 Hysteresis loop tracers

Hysteresis of magnetization is a typical phenomenon in magnetic materials and can be directly measured by a vibrating sample magnetometer (VSM) or using induction method. The two methods are all based on Faraday's law according to which an electromotive force (emf) is induced in a coil by a time-varying magnetic flux. The difference is in VSM the change flux is caused by the vibrating of the sample while in induction method the varying flux is generated by excitation coil.

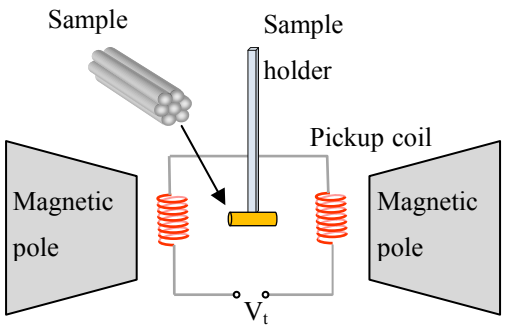

Fig. 3.2 Schematic working principle of the VSM.

The VSM was invented by Foner 50 years ago [98] and up to now has been the most successful hysteresis magnetometer due to its simplicity, ruggedness, easy operation, and high sensitivity. The field resolution can be as high as a few mili-Gauss while the field range is tens of mT. The working principle of VSM is shown in Fig. 3.2 in which the sample to be tested is mounted to the sample holder which is attached to a vibration exciter. The sample is magnetized by the constant field provided by electromagnet poles and the magnetic dipole moment of the sample will create a stray field $\boldsymbol{B}(\boldsymbol{r})$ around it.

$$\boldsymbol{B}(\boldsymbol{r}) = \frac{\mu_0}{4\pi}\left(\frac{\boldsymbol{m}}{r^3} - \frac{3(\boldsymbol{m}\cdot\boldsymbol{r})\boldsymbol{r}}{r^5}\right) \tag{3.1}$$

where $\boldsymbol{m}$ is the dipole magnetization moment of the sample, $\boldsymbol{r}$ is the position vector to the dipole, and

$$\frac{\partial B_i(t)}{\partial t} = \frac{\partial \boldsymbol{a}(t)}{\partial t}\cdot\nabla_{\boldsymbol{r}}\left\{B(r)\right\}_i \tag{3.2}$$

$\boldsymbol{a}$(t) being the position of the dipole and $\{B(r)\}_i$, i=1, 2, 3, the ith component of B at $\boldsymbol{r}$ due to dipole $\boldsymbol{m}$ [99]. When the sample is vibrating, changing flux from the stray field

induces the emf V_t in the pickup coils, which is proportional to the magnetization of the sample.

$$V_t = \sum_n \int_A \frac{\partial \boldsymbol{B}(t)}{\partial t} d\boldsymbol{A} \tag{3.3}$$

where $\boldsymbol{A}$ is the area vector of a single turn of the coil and the summing is done over n turns of the coils.

VSM can only measure the samples' hysteresis loops in longitudinal and transverse directions. However, for micro-wires with cylinder structure, circumferential hysteresis loop is also an important characteristic. Fig. 3.3 shows the designed hysteresis loop tracer capable of recording hysteresis in both longitudinal and circular directions for micro-wires. The device is based on induction method [100] which uses a different mechanism compared with VSM. For longitudinal hysteresis as shown in Fig. 3.3 (a), instead of measuring the stray field of the samples, the device measures the longitudinal magnetization $M_z(t)$ of the sample directly by a pair of pickup coils. The pickup coil pair consists of two nearly identical coils wound by 80 μm diameter enameled copper wire on cylinder plastic holders with inner and outer diameters of 3 mm and 4.5 mm, respectively. The length of the winding is 15 mm. Initially both coils were wound with 1600 turns and then a calibration was carried out and several turns were removed from one coil to get the exact compensation. From Eqn. 3.3 and

$$B(t) = \mu_0 H(t) + \mu_0 M(t) \tag{3.5}$$

the magnetization of the sample can be obtained by

$$\mu_0 M(t) = \int \frac{V_t}{nA} dt \tag{3.4}$$

Therefore, the hysteresis loop measured by induction method represents the dynamic magnetization of the samples at the certain frequency – typically at low frequencies (200 Hz).

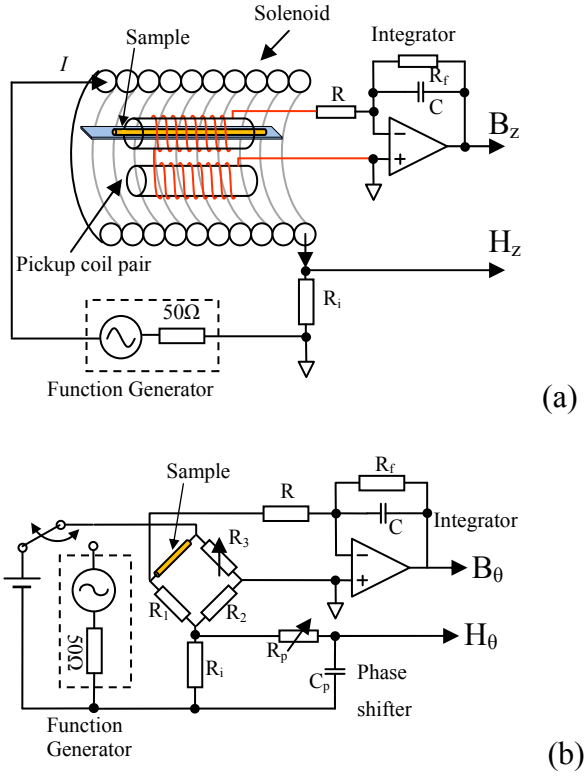

Fig. 3.3 Hysteresis tracer setups for hysteresis loops in (a) longitudinal and (b) circumferential directions. The combination of (a) and (b) can be used for the measurement of the off-diagonal components of the permeability.

For circumferential hysteresis loop measurement, the sample has to be excited by a circumferential magnetic field which can only be generated by an electric current flowing through the sample. In this case, no coils are able to pick up the induced voltage signal due to the fact that the changing flux is within the sample body and only electric potential difference between the two ends of the sample can be detected.

As a result, the sample itself is regarded as an equivalent pickup coil. However, according to Ohm's law, when a current flows through a conductor, the potential difference across the conductor is proportional to the current due to the conductor resistance. In another word, the voltage detected across the sample has two parts, one from changing flux, the other from dc voltage. Therefore, a Wheatstone bridge has been used in the circuit to compensate the dc voltage from the sample. Similar to Eqn. 3.3, the circumferential flux density $B_{\emptyset}$(t) can be obtained by

$$B_{\phi}(t) = \int \frac{V_t'}{A'} dt \tag{3.6}$$

Where V_t' is the compensated voltage across the sample and A' is the induction area of the sample, as shown in Fig. 3.4. In amorphous wires, $A' = R \cdot L$ where R is the radius of the wire. In composite wires, $A' = T \cdot L$ where T is the thickness of the permalloy layer and L is the length of the wire.

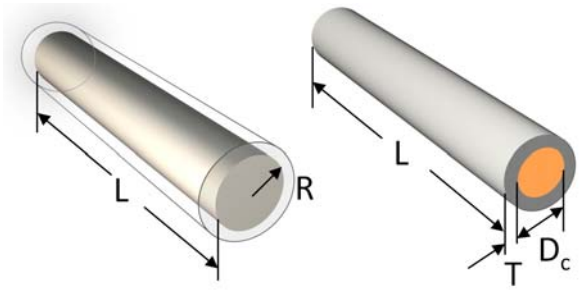

Fig. 3.4 Diagram of the dimensions of glass covered amorphous wire (left) and composite wire (right).

The circumferential hysteresis loops can then be plotted against circumferential magnetic field H, which depends on the excitation current and the distance between test point and the center of the wire, as shown in Fig. 3.5. Normally the peak value

$$H = \frac{I}{2\pi R} \tag{3.7}$$

was used as the x-axis in the BH curves.

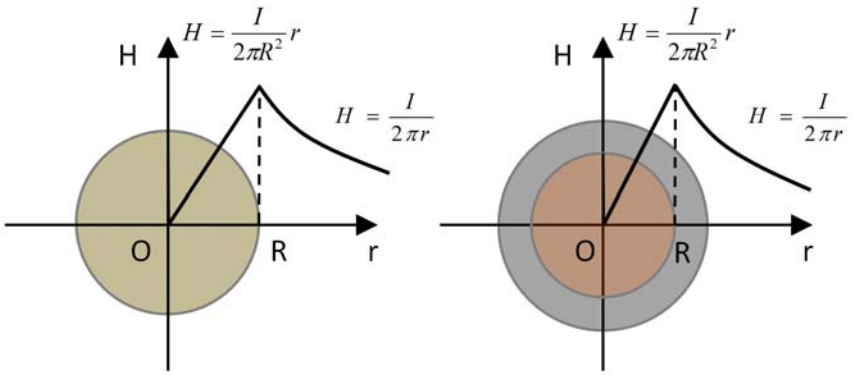

Fig. 3.5 Dependence of current induced circumferential magnetic field on the distance to the wire center in the amorphous wire (left) and composite wire (right) in which the current is assumed only within the inner copper core.

The advantages of the induced method over VSM are: 1) the size of samples can be larger, especially for wires, since VSM treats the sample as a magnetic dipole which is valid only when the sample size is small enough; 2) the range and frequency of the excitation field can be easily adjusted due to the simplicity of the device while the field resolution can be in a few nT; 3) the measurement is faster and results can be observed using a two-channel oscilloscope.

3.3.2 MI testing

Magneto-impedance effect which was firstly reported in ferromagnetic amorphous micro-wires in early 1990's [101-102], has been intensively studied for decades and become a research tool for characterization of novel structured ferromagnetic materials, such as micro-wires [103], thin films [104], and ribbons [105]. Magnetic properties of the materials, such as the magnetic anisotropy of the sensing elements with and without the longitudinal magnetic field, directional permeability, and

frequency responses, determine the MI measurement results and also can be deduced inversely from their features.

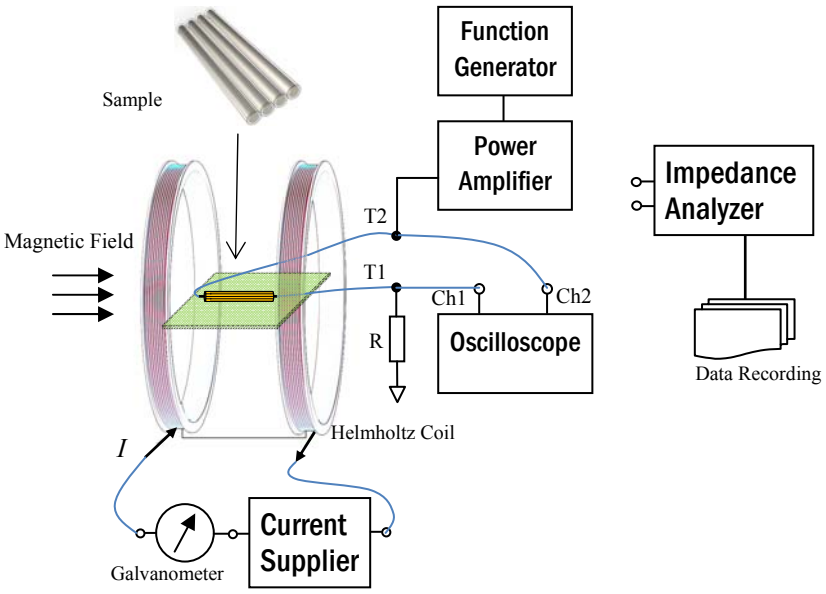

Fig. 3.6 Schematic diagram of MI measurement setup for multi-core sensing element test. For single wire, connect T1 and T2 to the impedance analyzer input directly.

The experimental setup of MI measurement is shown in Fig. 3.6, in which the sample was placed in the center of a Helmholtz coil connected to a current source providing an external magnetic field. An ac current was flowing through the sample and the amplitude of the current was monitored by channel 1 of the oscilloscope which measured the voltage drop across a resistor, $\tilde{V}_1$ at test point T1. The channel 2 measured the voltage at test point T2, $\tilde{V}_2$. Hence, the impedance of the sample $\tilde{Z}$, can be obtained by

$$\tilde{Z} = \frac{\tilde{V}_2 - \tilde{V}_1}{\tilde{V}_1} R \tag{3.8}$$

where R is a resistor connected to the sample in series. The impedance is a function of the frequency f, current amplitude I_0, and external magnetic field H_{ext}. The testing frequency was ranged from 10 kHz to 100 MHz and the current amplitude can vary from 20 mA_{rms} to 100 mA_{rms} typically for multi-core sensing element. When single wire was tested, the current amplitude needed was only 10 mA_{rms} and the testing setup can be simplified using a precision impedance analyzer (HP4294A) with T1 and T2 connected to the device input.

External magnetic field was controlled by changing the dc current going through the Helmholtz coil. The relative change of impedance, called MI ratio, is defined as

$$\frac{\Delta Z}{Z} = \frac{Z(H_0) - Z(H_{max})}{Z(H_{max})} \times 100\% \tag{3.9}$$

where $Z(H_{ext})$ and $Z(H_{max})$ are the impedance values of the sample under an external magnetic field H_{ext} and under the maximum external magnetic field H_{max}, respectively. Since MI is sensitive to the magnetic field, the measurement should be conducted inside a magnetic shielding chamber which is capable of attenuating the magnetic noise from environment. In this project, a shielding cylinder consisting of seven layers of FINEMET [106] sheets separated by insulators has been used and the attenuation factors of the shielding cylinder are 180 for dc magnetic field and 20 for ac magnetic field [107].

3.3.3 Gating curves

Gating curve is a transfer function describing the dependence of the changing flux on the excitation current which is proportional to the excitation magnetic field in fluxgate sensors [108]. Gating curves was firstly introduced in [36] to show the dependence of apparent permeability on the excitation field and later has become a characterization of magnetic property of sensing elements used in fluxgate sensors [109-114]. Experimental setup for gating curve measurement is shown in Fig. 3.7 in which the multi-core structured sensing element was place inside a pick-up coil wound with a 70 μm copper wire consisting of 1000 turns. The pickup coil was 3 mm in inner diameter and 9 mm of length. In operation, the sensing element is parallel to the external field to be sensed provided by a Helmholtz coil. The ac passing through the sensing element generates circumferential alternating magnetic field that drives the permeability of the ferromagnetic material in the sensing element to a sensitive dynamic state varying at the ac frequency, and the variation of magnetic flux in the sensing element with the external magnetic field induces an output voltage in the pick-up coil, as acquired by a pre-amplifier (SR560). The ac excitation current was supplied by a function generator, Agilent 33250A. The sensing output voltage was firstly amplified by the pre-amplifier and then measured using a SR844 DSP lock-in amplifier. The output voltage V_{out} can be viewed using an oscilloscope, Agilent 54624A. The changing flux Φ(t) can be obtained by

$$\Phi(t) = -\int V_{out} dt \tag{3.10}$$

Gating curves show the dependence of the axial field B in the core on the excitation current for certain value of external dc measured axial field H_0. The axial flux density

B_z(t) is calculated as an integral of the voltage on sensing coil, divided by the effective core cross sectional area and the number of turns (Eqn. 3.4). The height of this curve corresponds to the variation of the core axial field during the excitation cycle. Gating curves clearly reveal the operational mechanism of the orthogonal fluxgate: when the sensing element is periodically magnetized in circumferential direction, the axial flux changes simultaneously.

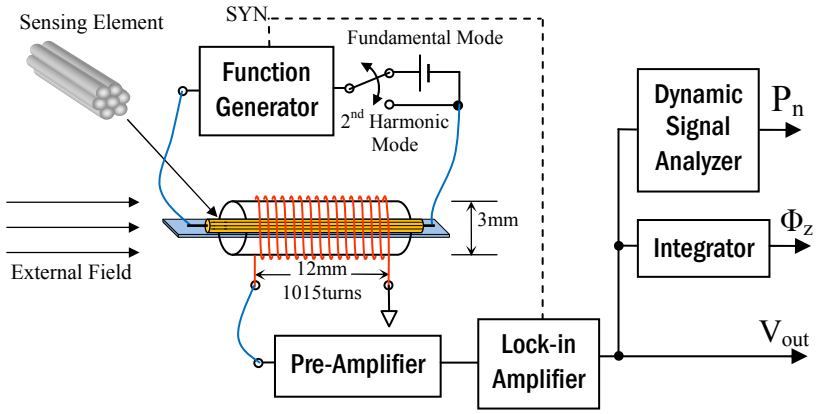

Fig. 3.7 Experimental setup for measurement of gating curve of the sensing element, sensor sensitivity, and noise level.

3.4 Sensor Performance Measurement

3.4.1 Sensitivity and uniformity

The experimental setup of sensitivity and noise measurement is similar to that of gating curves, as shown in Fig. 3.7. Two working modes can be selected by a switch: the fundamental mode has a dc bias current while the second harmonic mode has no bias. The sensitivity S of the tested structured sensing element is calculated by

$$S = \frac{\Delta V}{\Delta H} \tag{3.11}$$

where ΔV is the output voltage change in an external field range ΔH. The external magnetic field provided by a Helmholtz coil is normally ranging from 0 to 800 μT.

The setup of sensitivity measurement can also used to check the uniformity of the sensing element by simply monitoring the sensitivity while moving the long sensing element through the pickup coil. In this case, the pickup coil should be as short as possible to avoid the net effect. Power amplifier may be necessary in case of long samples that need large excitation voltage.

3.4.2 Noise level

The noise level measurement has to be conducted in a good shielding device. In this project, a four-layer shielding chamber with attenuation factor of 8,000 for dc magnetic field and 10,000 for ac magnetic field. In the measurement, the sensing element was placed inside the shielding chamber and no external field applied. The output voltage signal was firstly pre-amplified, then demodulated by a lock-in amplifier, and finally measured by a dynamic signal analyzer (Agilent 35670A) configured with 50 times RMS averaging with 98% overlap and a flattop window. The noise spectra was plotted in a frequency range from 60 mHz to 20 Hz. Unit used for noise level is

$$\frac{\sqrt{V^2/Hz}}{V/T} = T/\sqrt{Hz} \tag{3.12}$$

3.4.3 Temperature stability

Temperature stability of the sensor is a key requirement for precise magnetometers used in many outdoor applications with large temperature variations. To measure the

temperature stability of the multi-core orthogonal fluxgate sensor, a temperature-controlled shielding chamber has been designed and fabricated in this project. The design concept, as shown in Fig. 3.8, has an open cylindrical type magnetic shield, with an external heating chamber used to heat up air and a cooling chamber used to cool down air. The air being heated up would subsequently be pumped through the shielding chamber at a constant rate by a small fan. The heating and cooling effect was achieved by a thermoelectric module (TEM) [115] with a power of 241W [116]. Practically the heating chamber and the cooling chamber can share a same chamber since the transition from heating to cooling effect of the TEM can be easily implemented by changing the current flowing direction in the TEM.

The Advantages of this concept using thermoelectric module are:

1) Uniform heating as the air is pre-heated in an external chamber and subsequently transported through the chamber;

2) Less possibility of collecting dew in the chamber as the dew can be easily removed by tilting the chamber.

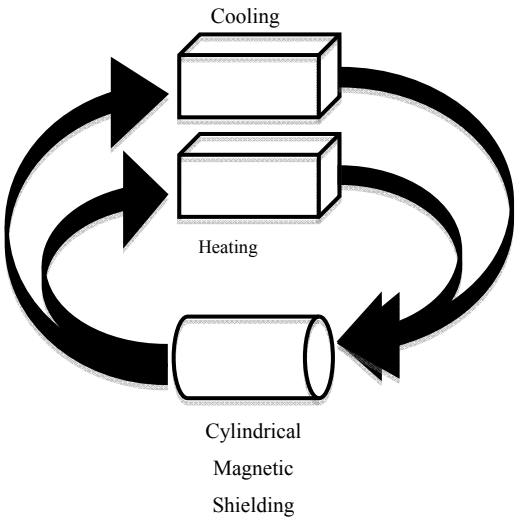

Fig. 3.8 Schematic of the cylindrical form magnetic shielding chamber

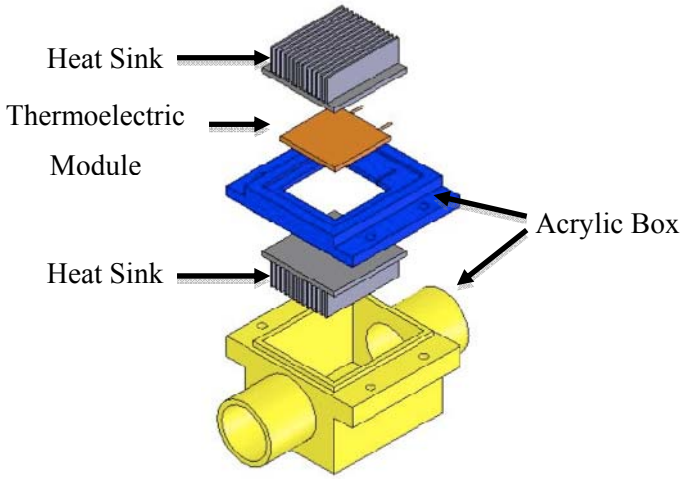

Fig. 3.9 Design of the thermal chamber using one piece of TEM

The thermal chamber design is shown in Fig. 3.9 in which one TEM was used as the heating/cooling source. The designed magnetic shielding chamber as shown in Fig. 3.10, possessed a length of 300mm and an internal diameter of 50mm. By having a dual-shelled cylindrical magnetic chamber that had 4 layers of FINEMET material, it was able to provide magnetic shielding attenuation factor of 100 when the magnetic source was located 10 cm away. Moreover, by sealing all the possible gaps in the

material by EMI shielding tape, it can further increase its shielding effectiveness by about 10 times. A temperature variation ranging from 10 ^{o}C to 70 ^{o}C in the shielding chamber can be achieved in 60 minutes.

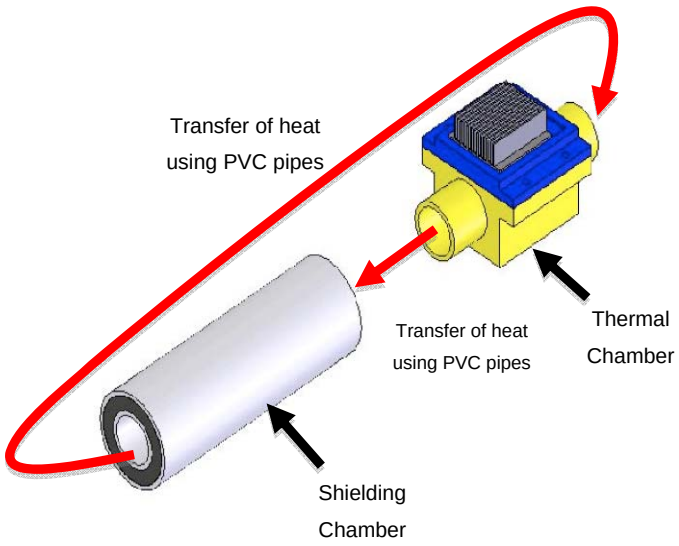

Fig. 3.10 Thermal chamber and shielding chamber of the temperature-controlled system.

Chapter 4
Magnetic Properties of Multi-core Sensing Element

Magnetic properties of the materials used as the sensing element in the magnetic sensors are essential for the sensor performance. Improving the magnetic properties of the single-wires is limited by their volume, uniformity, and fabrication processes. Therefore, new methods are needed for the further improving the magnetic properties of the sensing materials. It is found that multiple wires forming a structured array and being excited by ac current with at a certain frequency presented different magnetic properties compared to single wire, which is in favor for the orthogonal fluxgate application. In this chapter, the magnetic properties of the micro-wires in form of single wire and multiple-wire arrays will be characterized by hysteresis loops and magneto-impedance measurement. The dependence of magnetic properties of the two kinds of micro-wires, i.e. glass covered amorphous wires and composite wires, on their physical dimensions and structures has been investigated.

4.1 FeCoSiB Glass Covered Amorphous Micro-wires

4.1.1 Uniformity

Generally GCAWs fabricated using Taylor-Ulitovsky method have an advantage of uniformity compared with other fabrication methods. Nevertheless, it is necessary to characterize the uniformity of the samples before they are used as the sensing element of the sensors. Orthogonal fluxgate sensitivity test is a convenient and effective method as described in section 3.3.3. Fig. 4.1 shows a typical sensitivity profile of a

GCAW sample with length of 60 cm. At different points of the wire length huge changes of sensitivity can be observed within cm distance. Fig. 4.2 shows the large different sensitivity characteristics at some certain points.

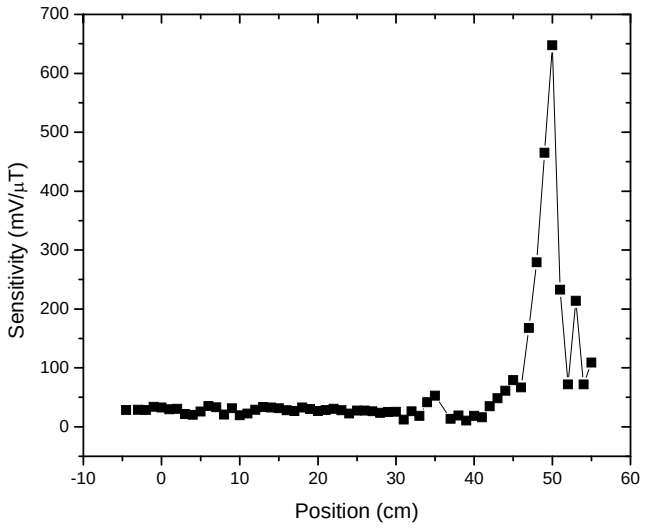

Fig. 4.1 Sensitivity profile along the 60 cm section of the amorphous wire

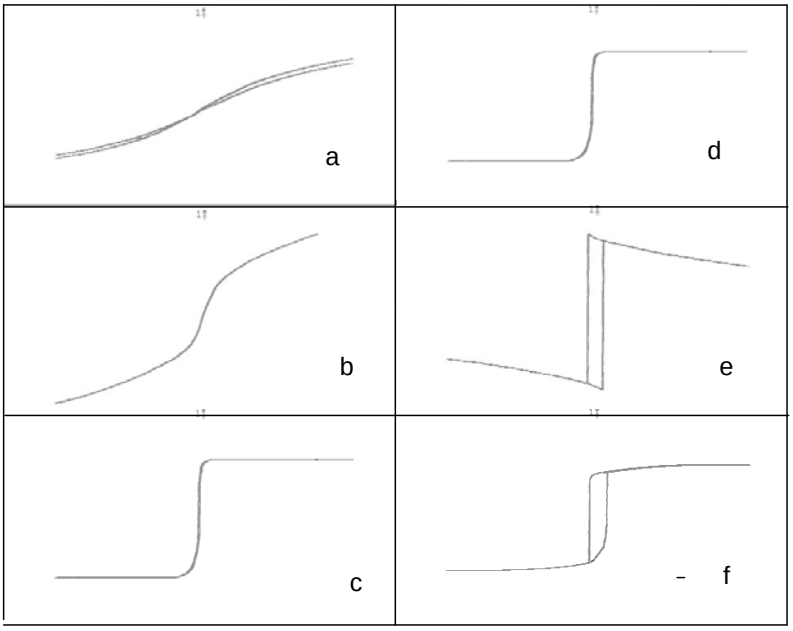

Fig. 4.2 Sensor characteristics (second harmonics voltage versus longitudinal external field) at different points of the wire from Fig. 4.1.

The main factors affecting the change of the shape are residual mechanical stresses in the wire and local regions with induced anisotropy causing spatially changing off-diagonal components of the permeability tensor. The irregular distribution of stresses can be caused by defects in the metal core or imperfect glass layer.

4.1.2 Hysteresis Loops of Single Micro-wire

4.1.2.1 Critical length of GCAWs with different anisotropy

FeCoSiB GCAW samples fabricated using Taylor-Ulitovsky method may have different magnetic properties due to configured composition and the complicated fabrication parameters. By measuring hysteresis loops of the single wire in longitudinal direction some important parameters, such as saturation magnetization M_s, remanent magnetization M_r, coercivity H_c, and anisotropy, can be obtained. For micro-wires with length ranging from one millimeter to several centimeters which is typical for the sensor applications, although the demagnetization factor should be very tiny according to the theoretical estimation [40], it was found that the length of micro-wires really matters [117-118]. GCAWs with longitudinal anisotropy had no critical length for the single large Barkhausen jump (LBJ) if the wire was longer than 2 mm [117]. However, GCAWs with different anisotropy can have remarkable different hysteresis profile and different length correlation. As shown in Fig. 4.3, FeCoSiB GCAWs with circumferential anisotropy display quite stable hysteresis profiles with as the length of the wires increases from 2 mm to 40 mm. There is no critical length to observe LBJ.

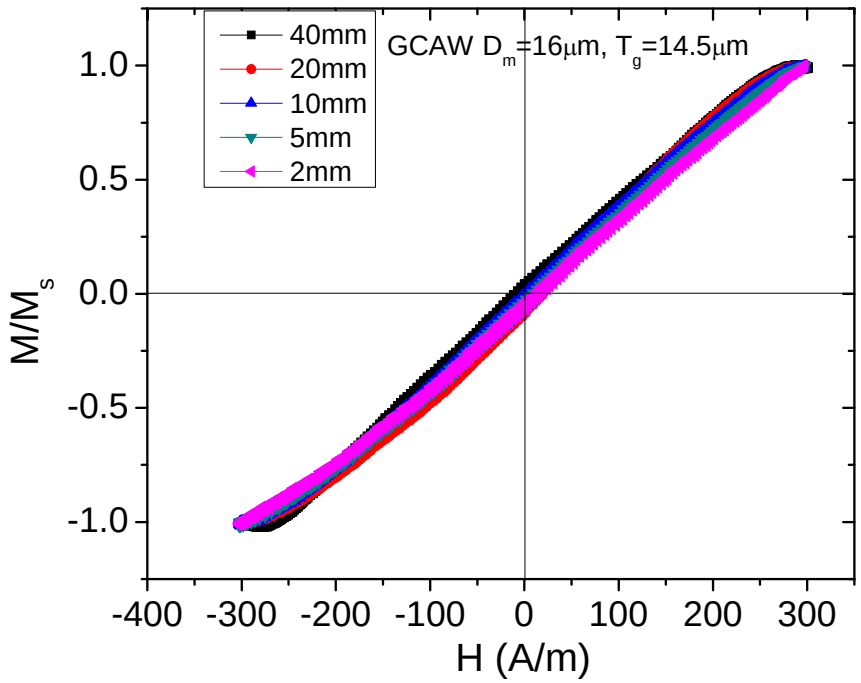

Fig. 4.3 Longitudinal hysteresis loops for CoFeSiB GCAWs with metal core diameter of 16 μm and a glass coating layer of 14.5 μm.

Fig. 4.4 (a) shows the hysteresis loops of the GCAWs with helical anisotropy and only small Barkhausen jump can be observed. There is a clear transform of the shape of the hysteresis loops, which can be characterized by the dependence of squareness ratio or the remanent to saturation magnetization ratio, M_r/M_s, and coercivity, H_c, on the wire length. Since only the IC contributes to M_r/M_s, the following relationship holds [119]:

$$\frac{M_r}{M_s} = \frac{R_c^2}{R_m^2} \tag{4.1}$$

where R_c is the radius of the IC.

As shown in Fig. 4.4 (b), a critical length around 5~10 mm can be found below which the anisotropy switches from helical direction to circumferential direction. The trend of the two curves is similar but details do not coincide. Since the transform process is a not a disrupted change, it can also be described by the maximum gradient of the hysteresis loops, χ_m, as

$$\chi_m = \frac{d\left(M/M_s\right)}{dH}\Big|_{H\to H_c} \tag{4.2}$$

χ_m is the normalized maximum susceptibility of the wires, χ_{max},

$$\chi_m = \frac{\chi_{\max}}{M_s} \tag{4.3}$$

And the maximum permeability of the material can be easily obtained by

$$\mu_{\max} = 1 + \chi_m M_s \tag{4.4}$$

As shown in the inset of Fig. 4.4 (b), with the increase of the wire length, the susceptibility increases at two rates, demarcated at 10 mm below which it increases almost 6 times faster than it does with the length above 10 mm. This value is more similar to the one got from M_r/M_s curve. Since M_r/M_s reflects the volume of IC that mainly responses to the external field in the low area, it can be concluded that the critical length is around 10 mm.

The critical length difference of the amorphous wires can be explained by the domain structures of the wires. For amorphous wires with LBJ there is a large single domain in the inner core (IC) dominates and the easy axis of the anisotropy is in the longitudinal direction. At the two ends of the wires there are relatively a small number

of domains with arbitrary anisotropy as so called end domains [93] or “closure” domains [117]. When the length of the wire decreases below the critical length, the single domain in the IC becomes much shorter and the end domains turn to dominate. For GCAWs without LBJ the domain structure in the outer shell (OS) plays an essential role for the magnetization process. The glass layer coated in the fabrication process exerts a significant stress on the OS of the metal core and induces a magnetoelastic coupling with magnetostriction in the OS, resulting in a circumferential anisotropy. The anisotropy direction of IC also depends on the coupling between dominant stress and magnetostriction. Therefore, the magnetization process of the wire has to be determined by a combined effect from IC and OS. In case of GCAWs with helical anisotropy, the IC has axial anisotropy. IC and OS have balanced contributions to the net magnetization. A quick inference is that the critical length of this kind of wires must be larger than that of wires with LBJ, which agrees well with the experiment results.

In case of GCAWs with circumferential anisotropy, the anisotropy of IC can be in either axial or radial directions. If IC has axial anisotropy, the OS must have dominant domain structure with strong circumferential anisotropy. For the sample tested, no LBJ observed and consequently no critical length found.

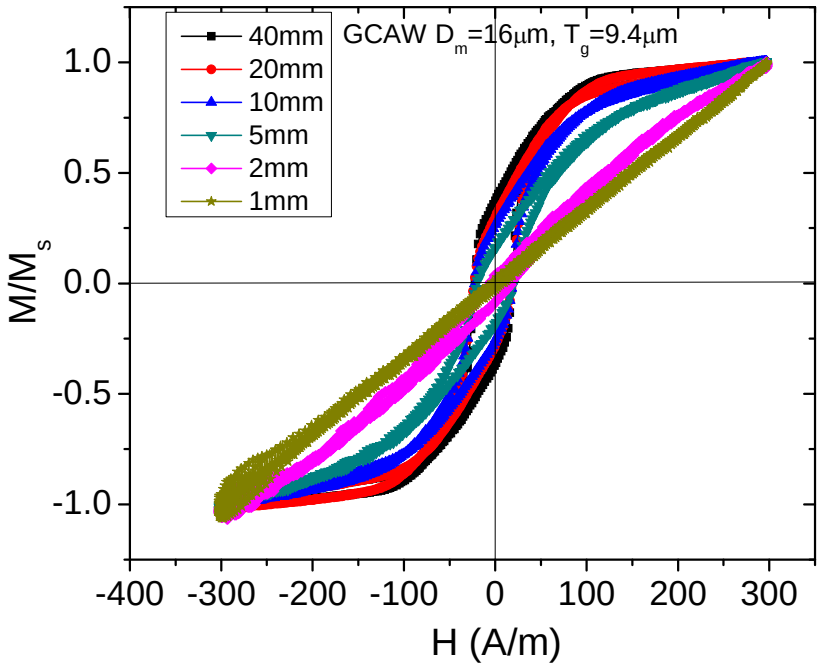

(a)

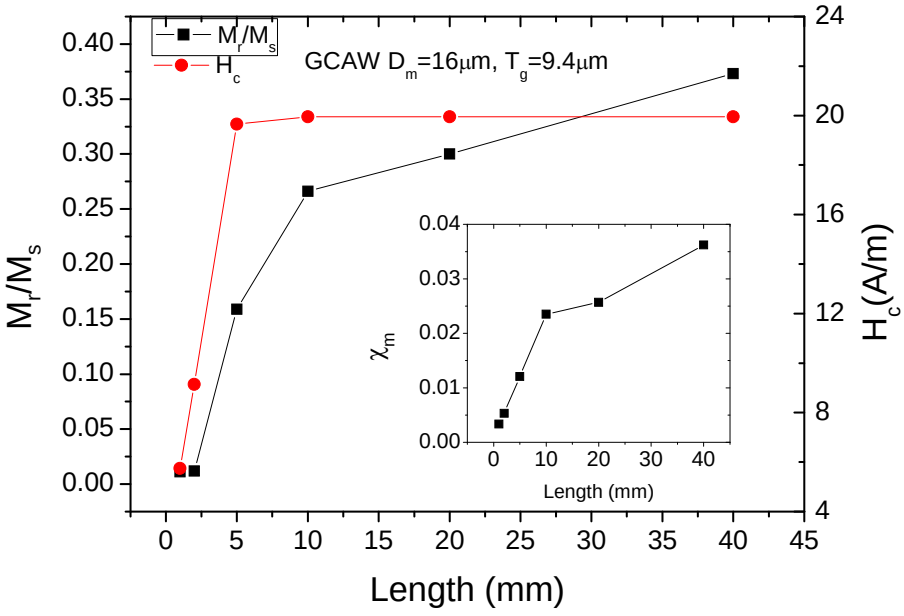

(b)

Fig. 4.4 (a) Longitudinal hysteresis loops of CoFeSiB GCAWs with metal core diameter of 16 μm and a glass coating layer of 9.4 μm with length ranging from 1 mm to 40 mm; (b) dependence of M_r, H_c and χ_m (inset) on the length of the wire.

4.1.2.2 GCAWs with different metal core diameters and glass coating thickness

It is well known that the intrinsic anisotropy of GCAWs is due to the magnetoelastic coupling between magnetostriction and internal stresses [87, 117, 120-125]. For GCAWs with certain composition of $Co_{68.15}Fe_{4.35}Si_{12.5}B_{15}$, the magnetostriction constant is near zero negative, typically in the order of 10^{-7}. The internal stresses in the micro-wires are induced by rapid solidification of the metal core and the difference between the thermal expansion coefficients of metal and coating glass. Since the stress from the glass coating layer to the metal core plays an essential role in the anisotropy distribution of the GCAW, it is of great significance to study the dependence of the magnetic properties on the geometrical parameters, i.e. metal core diameter and glass coating thickness. Fig. 4.5 and Fig. 4.6 show the longitudinal hysteresis loops for circumferential anisotropic GCAWs and helical anisotropic GCAWs, respectively. The metal core diameters were ranging from several microns to tens of microns, which is typical for micro-wires. All the micro-wire samples were in same length of 20 mm – far above the critical length of the GCAWs so that the shape of hysteresis loops results only from the structure of IC and OS of the wires and the effect of end domains can be ignored.

It can be observed from Fig. 4.5 (a) and Fig. 4.6 (a) that for CoFeSiB GCAWs there is no definite boundary between circumferential anisotropy and helical anisotropy. The anisotropy direction of some circumferential anisotropic micro-wires displays certain degrees of inclination from circular direction to helical direction and vice versa for some helical anisotropic samples. Therefore, besides the critical length, there must be some other parameters directly affecting the anisotropy and domain

distribution of the micro-wires. It was shown in section 2.5.2.1 that the circumferential anisotropy constant depends on the diameter of metal core and the thickness of glass coating layer but the relationship is unclear. Since the metal core of GCAWs has complicated anisotropy structures – at least in IC and OS and even the area between them, using metal core diameter alone cannot precisely characterize the local properties, for example, the circumferential anisotropy constant of the OS. Therefore, it is more accurate to employ the ratio between the thickness of glass coating layer T_g and the radius of metallic core R_m as a parameter. Indeed, the switching field and the coercitvity of the positive magnetostrictive GCAWs depends strongly on this ratio [85]. In this study, the switching field and coercivity are not always available due to the composition and structure of the CoFeSiB GCAWs. Instead, the normalized maximum susceptibility χ_m and ratio of M_r/M_s were used.

As shown in Fig. 4.5 (b) and Fig. 4.6 (b), the dependence of χ_m and M_r/M_s on T_g/R_m ratio is consistent and identical. Both χ_m and M_r/M_s decrease as the T_g/R_m ratio increases at a power exponent of -0.7 of T_g/R_m. That means the larger the T_g/R_m ratio, the anisotropy direction of the wires inclines more to the circumferential direction. This behavior can be well explained by the core-shell model of the GCAWs in which the IC is axial anisotropic and the OS is circumferential anisotropic. Larger T_g/R_m ratio results in larger magnetoelastic coupling between OS and effective stress from the glass coating layer. Correspondingly the volume of OS will increase and the volume of IC will decrease, as reflected by the squareness ratio M_r/M_s.

Two regions of the T_g/R_m ratio can be used to characterize the anisotropy of the micro-wires. When T_g/R_m ratio is smaller than 1, the wires show obvious

hysteresis loops and the anisotropy is in helical direction; when T_g/R_m ratio is larger than 1, the wires show little hysteresis loops and the anisotropy is almost in circumferential direction. Therefore, by controlling T_g/R_m ratio in the fabrication process, it is possible to tailor the properties of the GCAWs for specific applications.

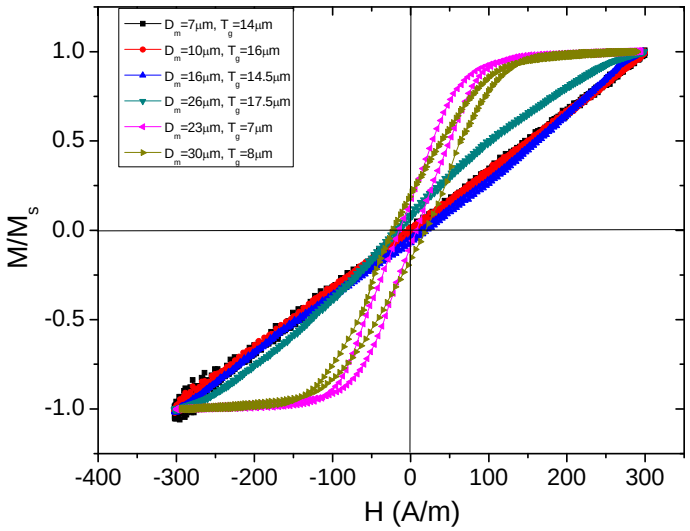

(a)

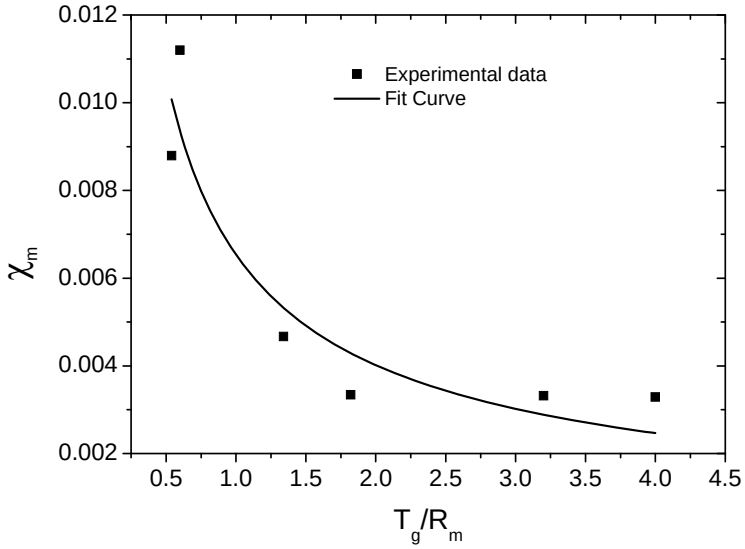

(b)

Fig. 4.5 (a) Longitudinal hysteresis loops of circumferential anisotropic CoFeSiB GCAWs with metal core diameter ranging from 7 μm to 30 μm; (b) Dependence of normalized maximum susceptibility χ_m on the ratio of glass coating thickness to metal core diameter T_g/R_m.

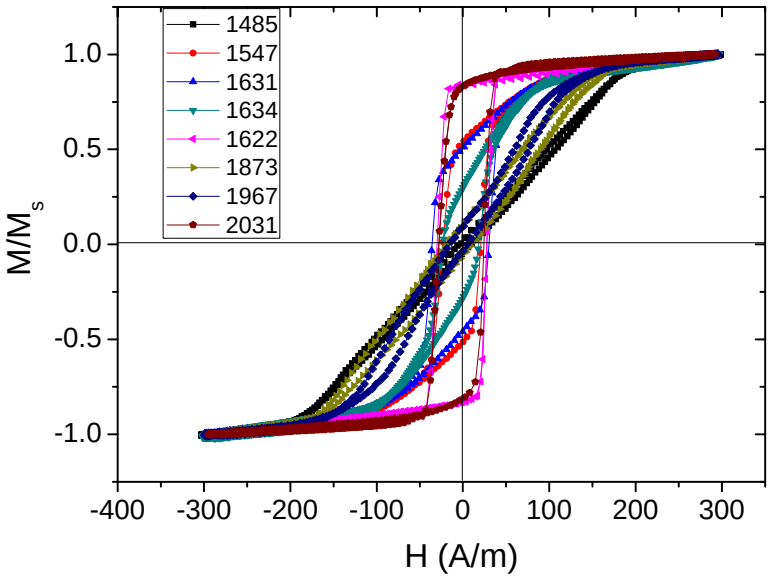

(a)

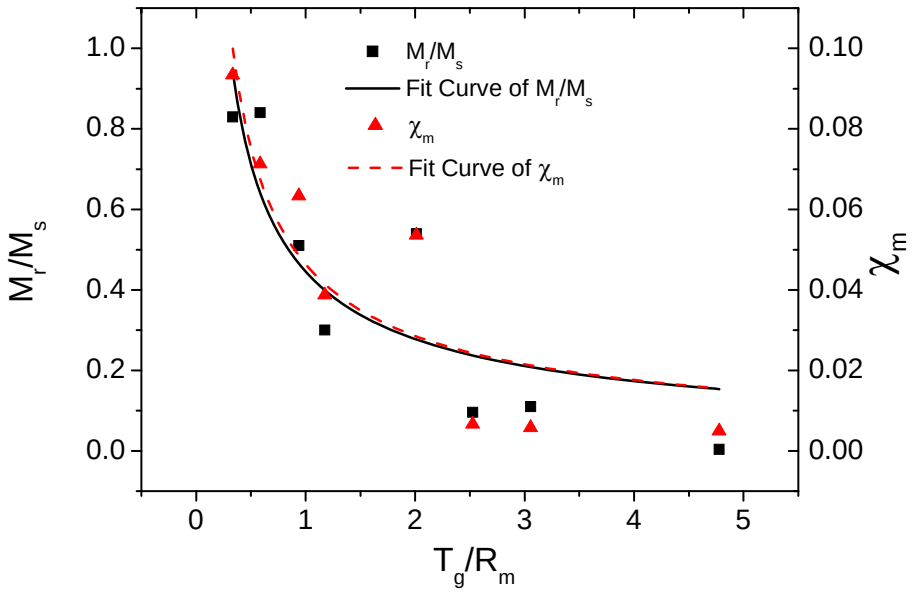

(b)

Fig. 4.6 (a) Longitudinal hysteresis loops of helical anisotropic CoFeSiB GCAWs with metal core diameter ranging from 14 μm to 20 μm; (b) Dependence of the squareness ratio M_r/M_s and normalized maximum susceptibility χ_m on the ratio of glass coating thickness to metal core diameter T_g/R_m.

4.1.2.3 Comparative study of GCAW and CDAW

GCAW with composition of $Co_{68.2}Fe_{4.3}Si_{12.5}B_{15}$ was produced by the Taylor-Ulitovsky method. Cold drawn amorphous wire (CDAW) with the same composition of $Co_{68.2}Fe_{4.3}Si_{12.5}B_{15}$ was obtained by in-rotating-water-quenching techniques and then cold-drawn (UNITIKA Co.). These two kinds of micro-wires were used as the sensing element in the orthogonal fluxgate sensors and showed different sensitivity characteristics [126]. Their basic magnetic properties have been investigated by longitudinal hysteresis loops at low frequency (300 Hz). It can be seen in Fig. 4.7 that GCAW has a coercivity of 8.0 A/m, smaller than that of CDAW, 25.6 A/m. Both of the two wires were not of pure circumferential anisotropy structure. The GCAW has an inner core with radial anisotropy and an outer shell with circumferential anisotropy [127]. So the coercivity of the GCAW is very small. The anisotropy of CDAW wire has a larger deviation angle from circumferential direction to longitudinal direction, due to an inner core with longitudinal magnetization [128], which is one reason for the larger coercivity than that of GCAW.

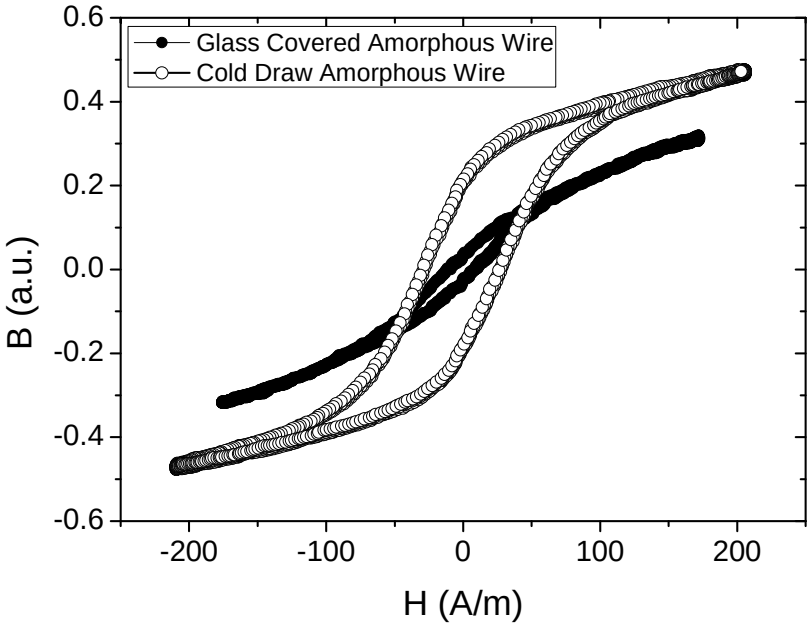

Fig. 4.7 Hysteresis loops of the cold-drawn amorphous wire (CDAW) and glass-coated amorphous wire (GCAW) in equal length of 15 mm. The metallic diameters of CDAW and GCAW were 30 μm and 20 μm, respectively.

4.1.3 Hysteresis Loops of Micro-wire Arrays

Fig. 4.6 shows the longitudinal hysteresis loops of micro-wire arrays measured by a VSM with and without ac current passing through the arrays. The arrays consisted of 1, 4, and 16 near-zero magnetostrictive $Co_{68.15}Fe_{4.35}Si_{12.5}B_{15}$ GCAW prepared in Taylor-Ulitovsky method. The dimensions of the wires were same 16 μm in metallic diameter and 10 mm in length. The wires were placed closely side by side and packed into bunches. During measurement the frequency of the ac current was 500 kHz for all samples and the current amplitude was fixed at 6 mA_{rms} per wire which was large enough to saturate the wires in the circumferential direction [97]. The used Co-based amorphous wire has a circumferential anisotropy [85] resulted from the well-known

core-shell structure with the inner core (IC) having a radial anisotropy and the outer shell (OS) having a circular anisotropy [129]. It is shown in Fig. 4.6 (a) that with the number of wires in the arrays increases the anisotropy direction of the arrays inclines to circular direction. Since the thickness of the OS is usually about 5% of the metallic nucleus diameter and there is a larger interdomain wall between the IC and OS [130], the neighboring wires can interact with each other to rearrange the domain distribution in the array resulting in a lower total magnetostatic energy. This is a unification effect of the domain wall movement possibly in the interdomain walls between IC and OS as well as in the OS that enlarges the circular domain components and consequently changes the net anisotropy direction.

In understanding the fundamental difference between the single-core orthogonal fluxgate sensor and multi-core orthogonal fluxgate sensor, the magnetic coupling between the multi-cores under the condition of excitation ac passing through should be noted. That is, besides the static hysteresis loops, the dynamic hysteresis loops of the arrays are more significant for the sensor applications. Fig. 4.6 (b) shows that when an ac current was applied to the wire array, the anisotropy direction further inclined, which indicates that an additional circumferential anisotropy was induced. The normalized maximum susceptibility χ_m quantifies the inclination of the anisotropy direction showing a trend of decreasing with the increase of the number of wires in the array in both static and dynamic measurement.

Moreover, the saturation field H_s increases with the number of wires and H_s values with current excitation are much larger than the H_s values without current excitation (3 times for 1-wire and 4-wire arrays, and 1.7 times for 16-wire array). This

means that the more wires in the array, the larger magnetizing energy required to saturate the array in the longitudinal direction, and that the excitation current applying to the arrays exasperates such effect.

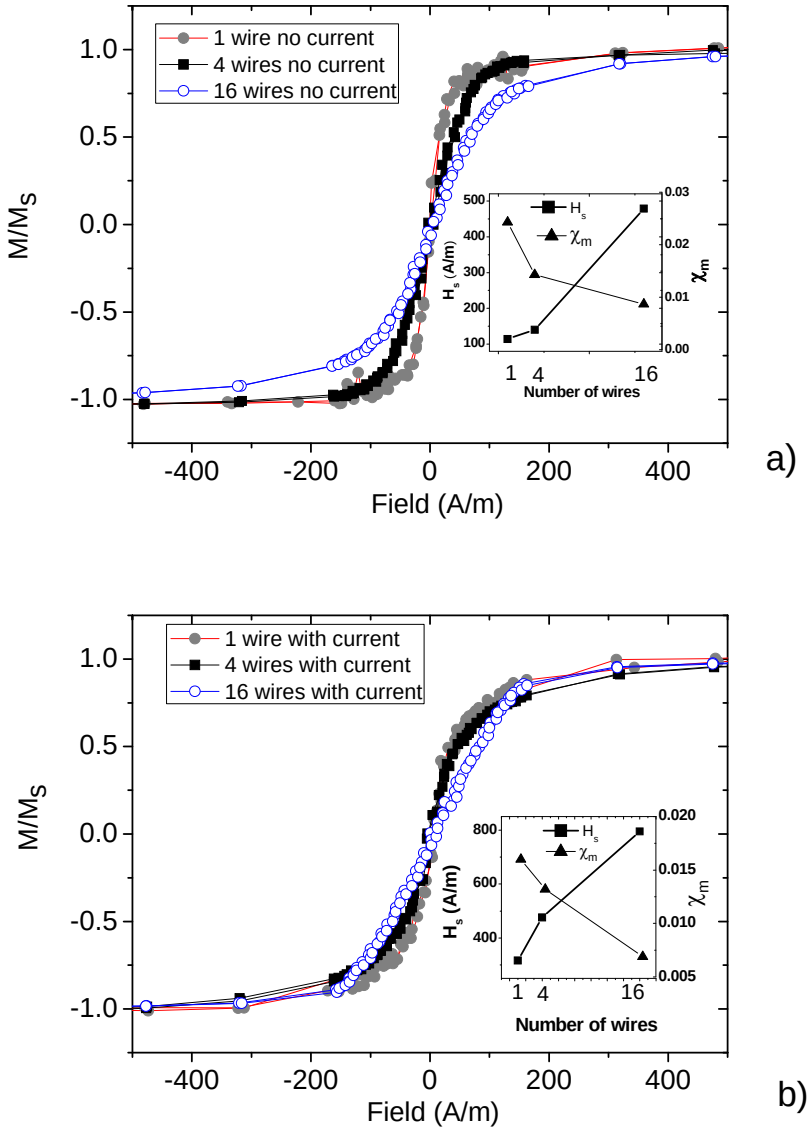

Fig. 4.8. Longitudinal hysteresis loops of 1-wire, 4-wire, and 16-wire arrays measured (a) without and (b) with applying excitation current (frequency was 500 kHz, amplitude was 6 mA_{rms} for 1-wire, 24 mA_{rms} for 4-wire and 96 mA_{rms} for 16-wire). The insets show the dependence of saturation field H_s and normalized maximum susceptibility χ_m on the number of wires.

4.1.4 MI effect

4.1.4.1 Comparative study of GCAW and CDAW

The different magnetic anisotropy of the inner core of the GCAW and CDAW may also affect the frequency characteristic of the circumferential permeability μ_φ, which has the similar trend with sensitivity of the orthogonal fluxgate. We used magnetoimpedance effect (MI) to examine this frequency characteristic, since the sensitivity of MI sensors is proportional to the $\sqrt{\mu_\phi}$ [128].

Fig. 4.9 (a) and (b) show the MI ratios in variation with an external magnetic field for GCAW and CDAW, respectively. Both of the two kinds of sensing elements showed double-peak MI curves at high frequency. The MI ratio spectrums of GCAW and CDAW are shown in Fig. 4.10. It can be seen that in the lower frequency range, the MI ratio of GCAW was smaller than that of CDAW, but at higher frequency range the MI ratios for GCAW were higher than those of CDAW. This is consistent with the frequency dependence of sensing output for sensors using GCAW and CDAW. It can be explained by the nature of MI, which is based on the circumferential permeability of the sensing element in variation with the external magnetic field. Driven by an *ac* current, the impedance of the sensing element depends on the skin-effect depth,

$$\delta = \sqrt{\frac{2}{\sigma \mu_\phi \omega}} \tag{4.5}$$

where σ is the conductivity and ω is the angular frequency of the *ac* current.

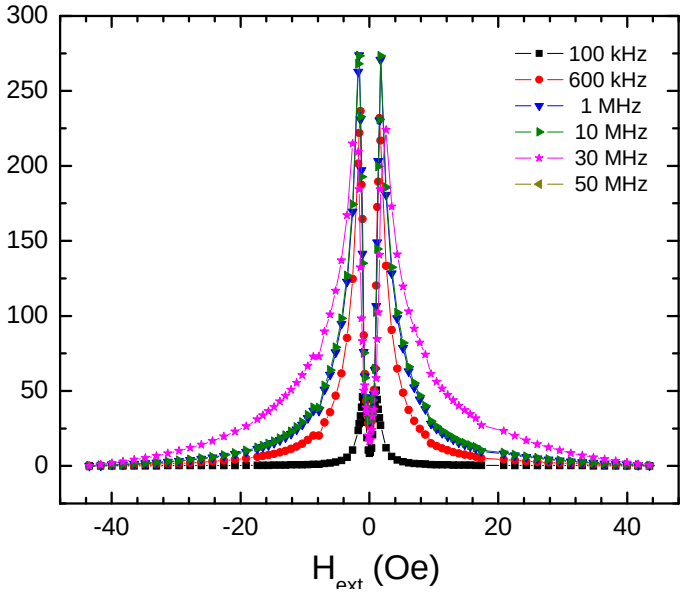

(a)

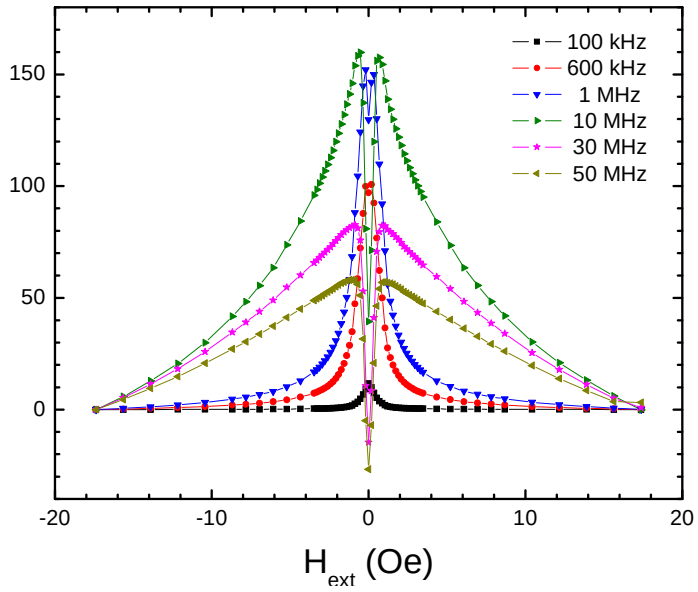

(b)

Fig. 4.9 MI ratio in variation with an external magnetic field for: (a) glass-coated amorphous wire and (b) cold-drawn amorphous wire.

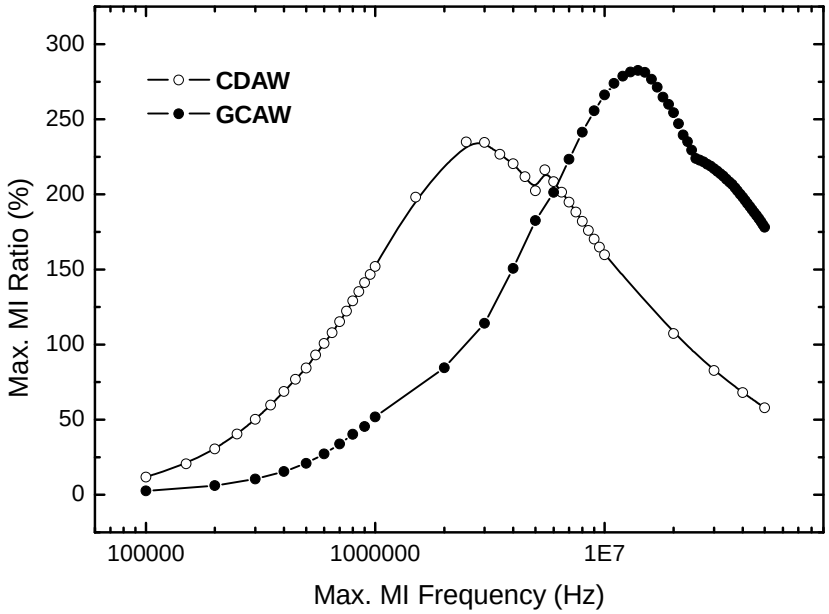

4.10 Maximum MI spectrum of the cold-drawn amorphous wire (CDAW) and glass-coated amorphous wire (GCAW).

The MI ratio is related to the dependence of circumferential permeability on the external magnetic field, while the orthogonal fluxgate sensor sensitivity is dependent on the differential of the longitudinal permeability of the sensing elements with time. The MI ratio and the sensor sensitivity have similar trends in variation with the external field [126]. The external magnetic field affects the magnetization distribution and consequently affects the magnetic permeability of the wire. As a result, the impedance becomes a function of the magnetic field. Since GCAW and CDAW have the same composition, the difference in the MI ratio spectrum must be due to the differences in their diameter and anisotropy. Theoretically, the MI reaches the maximum while the skin depth is equivalent to the geometric size, therefore

$$D_m^2 \propto \frac{1}{\mu_\phi \omega} \tag{4.6}$$

where D_m is the metal core diameter of the micro-wire. Hence generally, if the magnetic properties of the wires were identical, for wires with smaller diameter the optimum excitation frequency is higher. For CDAW the diameter was 30 μm and MI optimum frequency was 2.5 MHz, while for GCAW these values were 20 μm and 14 MHz respectively. The ratio of the optimum frequencies would be $(30/20)^2 = 2.25$, while the measured ratio was 14/2.5 = 5.6. The discrepancy between the measured ratio and the one calculated from the diameter ratio could be attributed to the difference between the circumferential permeability of CDAW and GCAW, as can be derived from the MI curves shown in Fig. 4.9.

4.1.4.2 MI effect of micro-wire arrays

MI effect of micro-wires arrays consisting of 1, 2, and 4 near-zero magnetorestrictive $Co_{68.15}Fe_{4.35}Si_{12.5}B_{15}$ GCAWs prepared in Taylor-Ulitovsky method has been investigated. All of the micro-wires were cut from a single long micro-wire with metal core diameter of 16 μm and therefore they were of same electrical and magnetic properties. The wires were of same length of 20 mm and were closely placed side by side into bunches. Fig. 4.11 shows the typical field dependence of the MI ratios for the 1-wire, 2-wire, and 4-wire arrays at the frequency of the driving ac current varying from 10 kHz to 100 MHz. In all cases, double peaks were observed, which coincides with the result from hysteresis loop measurement that their easy axis of the anisotropy is in circumferential direction.

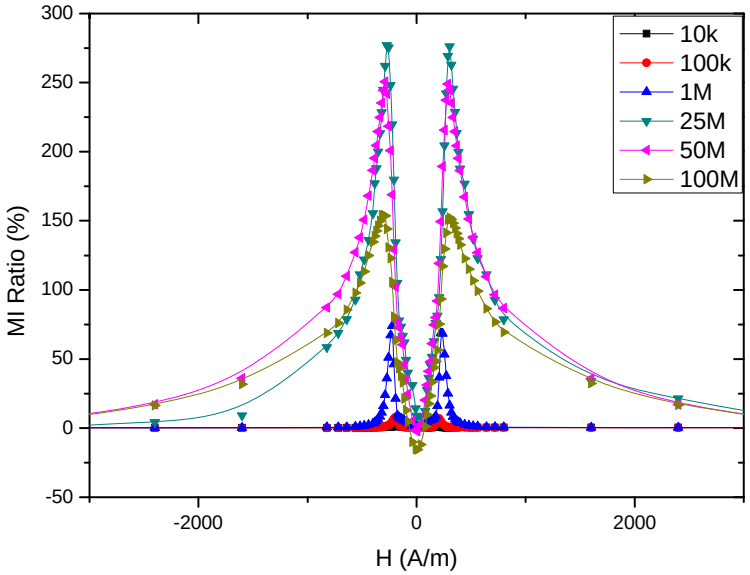
MI Ratio (%)
H (A/m)
10k
100k
1M
25M
50M
100M
300
250
200
150
100
50
0
-50
-2000
0
2000

(a)

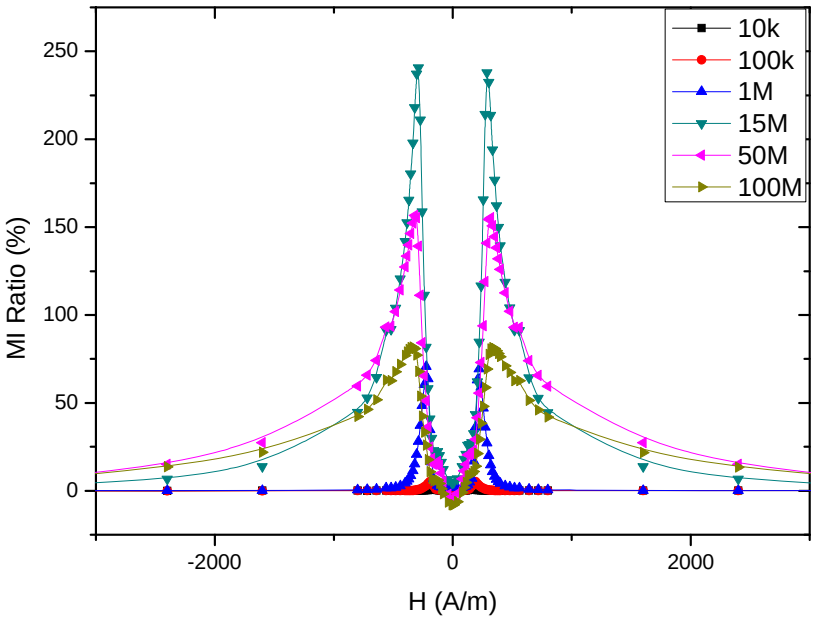
MI Ratio (%)
H (A/m)
10k
100k
1M
15M
50M
100M
250
200
150
100
50
0
-2000
0
2000

(b)

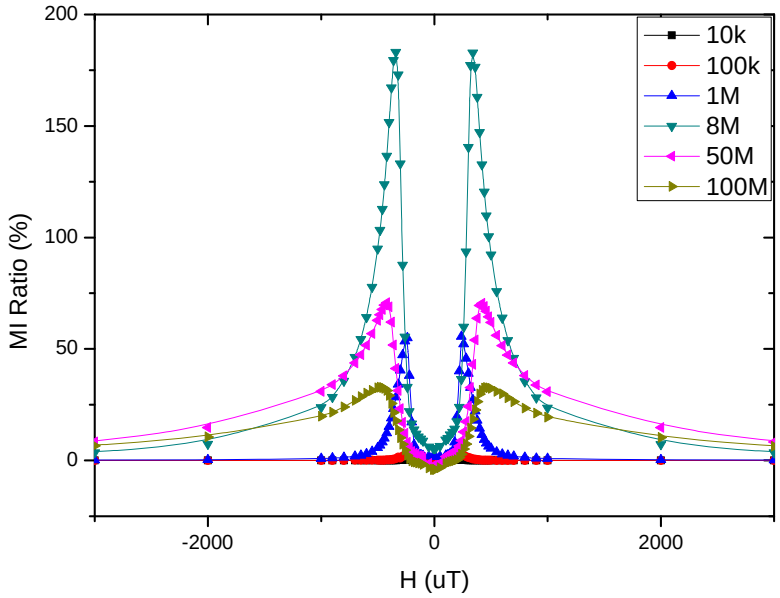

(c)

Fig. 4.11 Field dependence of MI ratios for (a) 1-wire, (b) 2-wire, and (c) 4-wire arrays.

The frequency dependence of the maximum MI ratios shown in Fig. 4.12 (a) indicates that the maximum MI ratio decreases as the number of wires in the arrays increases, which is in contradiction to the results reported in [131]. The MI ratio decrease can be explained by the fact that the skin effect in each wire of an array was weakened by the domain unification in the array. The relationship between impedance, Z, of the material and the skin depth, δ, is [132]:

$$Z \sim \frac{1}{\delta} \tag{4.7}$$

Since the driving current was flowing through the wires in parallel, the eddy current in the wires was compensated by the effect of the stray field from neighboring wires so

that the skin depth of each wire in a multi-wire array was larger than that in a 1-wire array. As a result, the MI ratio was smaller.

It is noteworthy that the frequency of the maximum MI ratios decreased with the increase of the number of wires in the arrays, as shown in the inset of Fig. 4.12 (a), where the peak MI ratio occurred at about 35 MHz for 1-wire array, 28 MHz for 2-wire array and 15 MHz for 4-wire array, respectively. Consider the domain wall velocity of the amorphous micro-wires, v, and the dimension of the circular domains spacing, l, the domain motion frequency, f, can be expressed as

$$f \sim \frac{1}{l/v} \tag{4.8}$$

When v is in the range of 450-650 m/s at room temperature [133] and l is in the order of 10 μm (40 μm for Co-based amorphous microwires [134]), the maximum domain motion frequency is in the range of 11-65 MHz, which is in good agreement with the frequency of the maximum MI ratio in variation with the increase of the number of wires in the array, where the dimension of the interacting domains increased as the number of wires increased and then the frequency decreased.

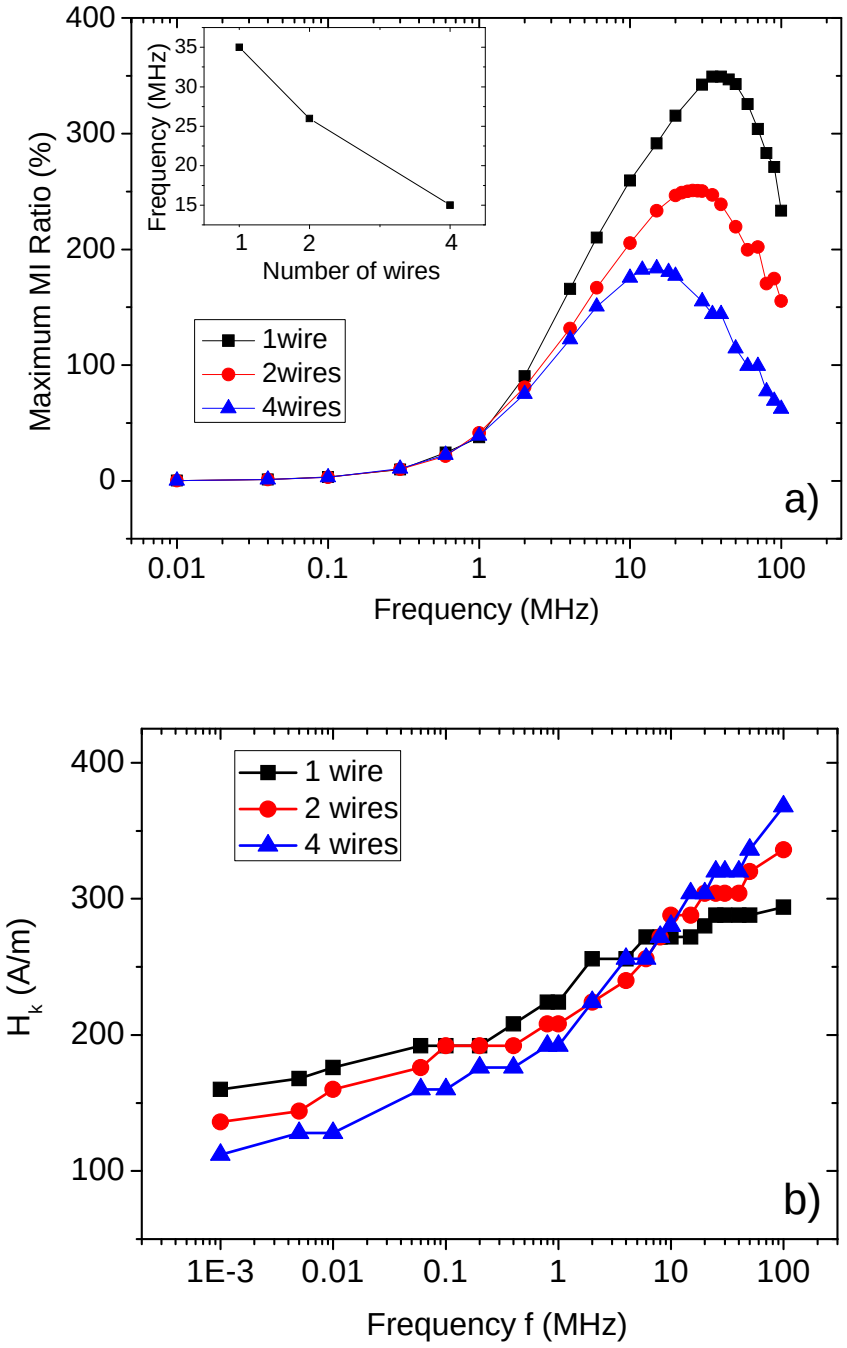

Fig. 4.12 Frequency dependence of (a) maximum MI ratios and (b) peak field (approximately the anisotropy field) for 1-wire, 2-wire, and 4-wire arrays.

Fig. 12 (b) shows the field dependence of the peak field (approximately the anisotropy field H_k) for 1-wire, 2-wire, and 4-wire arrays. The peak fields for all samples increased with the frequency. A critical frequency, f_c, can be found at around 10 MHz, below which H_k decreased with the number of wires and above which H_k increased with the number of wires. This can be explained by the fact that the higher the frequency, the larger the phase lag of the magnetization of the arrays behind the excitation field and consequently smaller effective permeability. At a certain frequency, smaller H_k leads to larger initial permeability of the wire arrays.

Moreover, the critical frequency delimitates the frequency to two bands: below f_c, the both domain wall displacement and domain rotation contributes to the MI responses and domain wall displacement dominates the domain unification effect; above f_c, the domain displacement is strongly damped by eddy current and domain rotation dominates. Therefore, the MI response of the micro-wire arrays is a dynamic phenomenon resulted from the interaction of the magnetic domain unification and eddy current.

4.2 Electroplated NiFe/Cu Composite Micro-wires

The NiFe/Cu composite wires used in the magnetic property characterization are prepared by electrodepositing of a 2 um thick permalloy layer on a 20um diameter copper wire under the same conditions. For micro-wire arrays, the inter-wire insulation coating has been conducted for each composite wire using diluted epoxy resin. Arrangement of the micro-wire arrays with different number of wires has been accomplished. The length of the arrays is equally 10 mm.

For the purpose of constructing the micro-wire arrays as the multi-core sensing element, specific setups have been designed and fabricated to place the multiple wires close enough to make magnetic interaction between the wires possible. One design of such setups is a multi-wire holder with several straight 'V' shape grooves which allow the wire to alight with. The schematic of the multi-wire holder is shown in Fig. 4.13 (a). In the optimal case, the sensing element should be placed as close to each other as possible, while not touching each other. Fig. 4.13 (b) shows the fabricated 3-wire holder under a microscope, where 3 grooves can be easily identified.

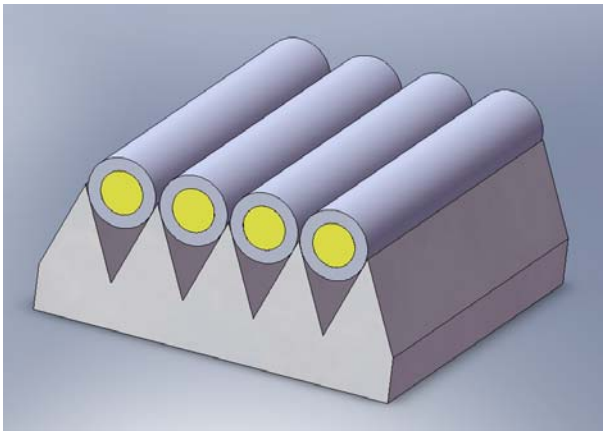

(a)

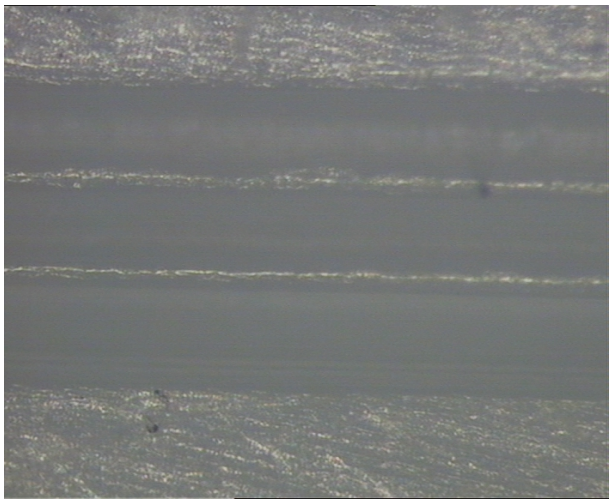

(b)

Fig. 4.13 (a) schematic of multi-wire holder for micro-wire array (b) Fabricated 3-wire holder under a microscope.

Micro-wire arrays were fabricated under microscope manually. The composite wires are placed side by side or on the top of previous wires. A planar structure was firstly constructed and fixed and then other wires were added one by one. Diluted nail polish was used for fixation of the wires on the holder. Fig. 4.14 shows the fabricated multi-core sensing elements with different number of wires and different structures.

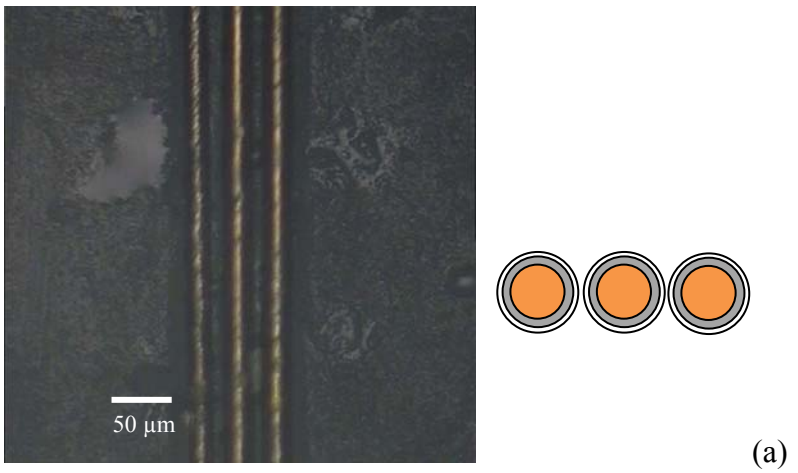

(a)

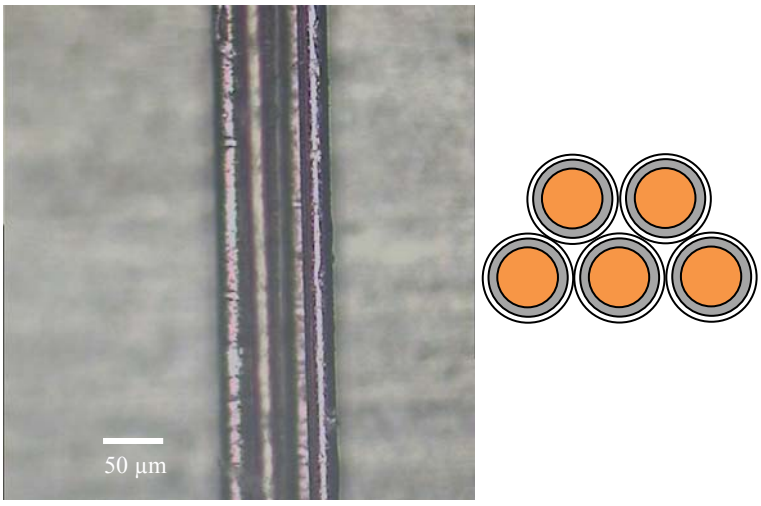

(b)

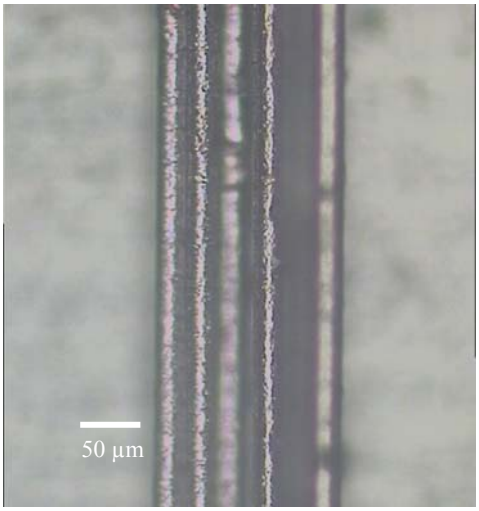

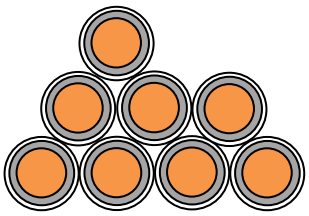

(c)

Fig. 4.14 NiFe/Cu composite Micro-wire arrays under microscope and schematic of the structures. (a) 3-wire, (b) 5-wire, and (c) 8-wire.

4.2.1 Hysteresis loops of composite micro-wires

4.2.1.1 Hysteresis loops of single wire

Length effect of the anisotropy of NiFe/Cu composite wires has been investigated by measuring the axial hysteresis loops of samples. Fig. 4.15 (a) shows the dependence of the hysteresis loops on the wire length ranging from 2 mm to 40 mm. The shape of the hysteresis loops transforms gradually from large hysteresis to near linear indicating that the anisotropy direction of the CWs changes from helical to circumferential as the length of the wires decreases. Quantified parameters are plotted in Fig. 4.15 (b) showing that the transform process is quite smooth compared with that of GCAWs. Instead of a clear critical length indicated in the curves of GCAWs, there is no obvious demarcation in the curves of CWs so that the critical length can only be estimated to be around 10 mm.

The squareness ratio M_r/M_s of CW is almost twice of that of GCAW with the same length while the coercivity H_c of CWs is also 75% larger than that of GCAWs. It can be concluded that the anisotropy of CWs is in helical direction and inclines more to axial directions than of GCAWs.

Another difference with GCAWs is the dependence of M_r/M_s, H_c, and χ_m on the length are quite identical implying that the magnetic properties of CWs are uniform and stable in the samples with different length. This significant difference is due to the structure and material of the wires. For CWs, the wire structure is much simpler than that of GCAWs. There is no magnetic inner core in the wire center and no glass coating layer outside the shell, which provides no complicated magnetic domain walls between neighboring magnetic domains and much less coupling between stresses and magneostriction. As for the material, instead of amorphous CoFeSiB in GCAWs, the NiFe in CWs displays nanocrystlline state and there is magnetocrystalline anisotropy involved. Considering the shape of the CWs, the demagnetization can be ignored so that the magnetocrystalline anisotropy is dominant in the CWs.

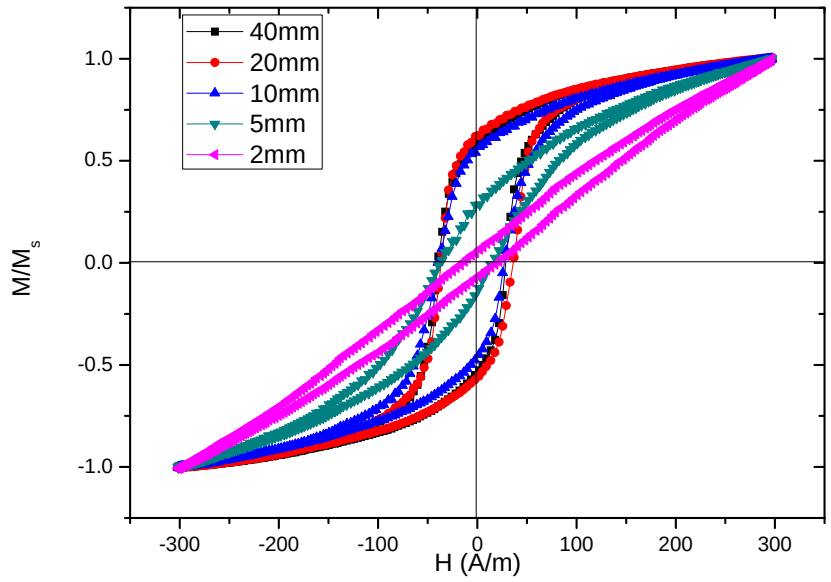

(a)

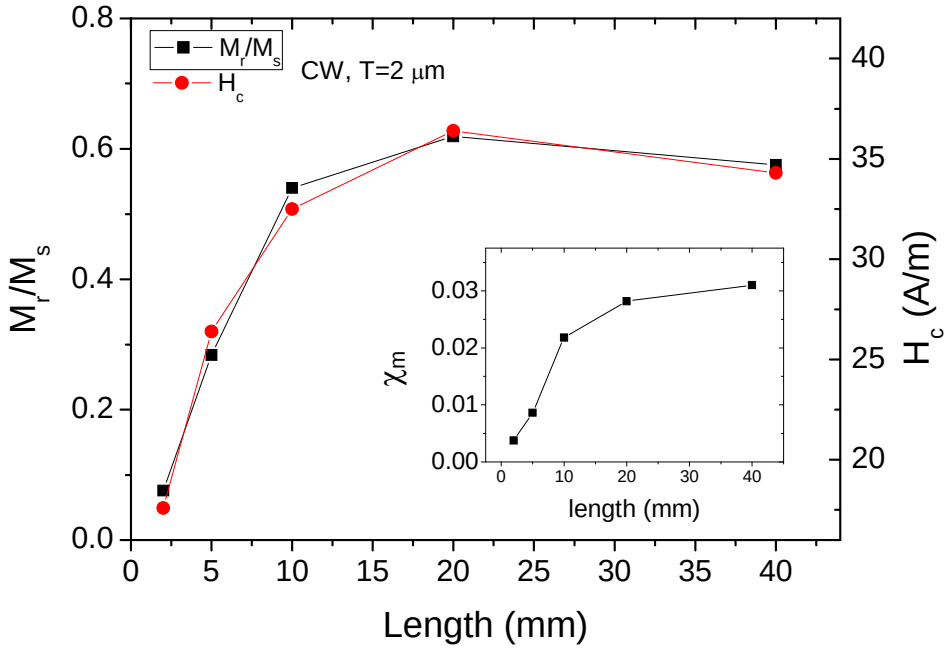

(b)

Fig. 4.15 Longitudinal hysteresis loops of NiFe/Cu CWs with copper core diameter of 20 μm and a permalloy layer of 2 μm with length ranging from 2 mm to 40 mm; (b) dependence of M_r/M_s, H_c and χ_m (inset) on the length of the wire.

Besides the length effect, circumferential hysteresis loops [108] have been measured compared with longitudinal hysteresis loops, as shown in Fig. 4.15, to characterize the magnetic properties of the CWs. The hysteresis loops indicate that the CWs have moderate anisotropy in preferred helical direction. Since the ferromagnetic material is only on the surface of the conductive core forming a thin cylinder shell, compared with the core-shell structure in amorphous wires, the magnetic anisotropy of composite wire was unitary and would result in less magnetic remanence.

The circumferential hysteresis loops are of significance for the magnetic property study. Comparing these loops with conventional axial hysteresis loops allows to investigate the core anisotropy and to optimize the annealing treatment. It can be obtained from the hysteresis loops that the normalized maximum susceptibility χ_m in the axial direction, $\chi_{m,z}$, is 3 times of that in circumferential direction, $\chi_{m,\theta}$. The direction of the helical anisotropy inclines more to axial direction.

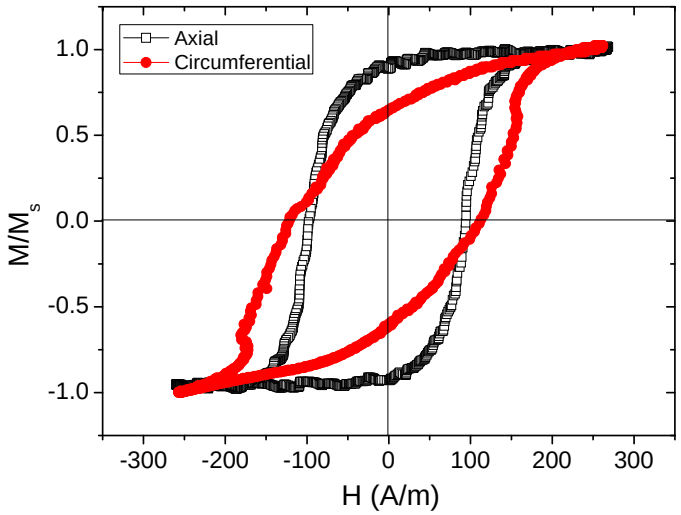

Fig. 4.16 Circumferential and longitudinal hysteresis loops of the NiFe/Cu composite wire.

4.2.1.2 Hysteresis loops of micro-wire arrays

Previous study revealed that the electrodeposited NiFe/Cu microwire has a helical anisotropy with a inclination to circular direction [88][108]. The longitudinal hysteresis loops of the microwire array show that their anisotropy changes towards longitudinal direction with the increase of the number of wires in the arrays, except the 3-wire array which demonstrated obviously an inclination to circumferential anisotropy, as shown in Fig. 4.17 (a). As shown in Fig. 4.17 (b), the coercivity H_c increases with the increase of number of wires and presents a local maximum in the 5-wire array, whereas the squareness ratio M_r/M_s and normalized maximum susceptibility χ_m also increases with the number of wires but presents a local minimum in the 3-wire array. The trend is just in opposite with that of GCAWs. Since all the wires were fabricated at the same conditions and carefully selected based on their composition and surface uniformity, the anisotropy of each wire was almost the same as others. The change in anisotropy is mainly due to the magnetic interaction between the wires in the arrays. It can be seen that for wires with helical anisotropy, domains in longitudinal direction can be enlarged easier than those in circumferential direction in the interaction process. The arrays with different structures verified this – the 3-wire array has the planner structure which is unfavorable for the interaction while other arrays are in compact structure which is favorable for the interaction.

It is worth examining the identical trend of squareness ratio M_r/M_s and normalized maximum susceptibility χ_m. As discussed in section 4.12, M_r/M_s ratio reflects the magnetization volume mainly responses to the external field. The

increasing trend of M_r/M_s indicates that the portion of magnetization with axial directions increases with the increase of the number of wires in the arrays.

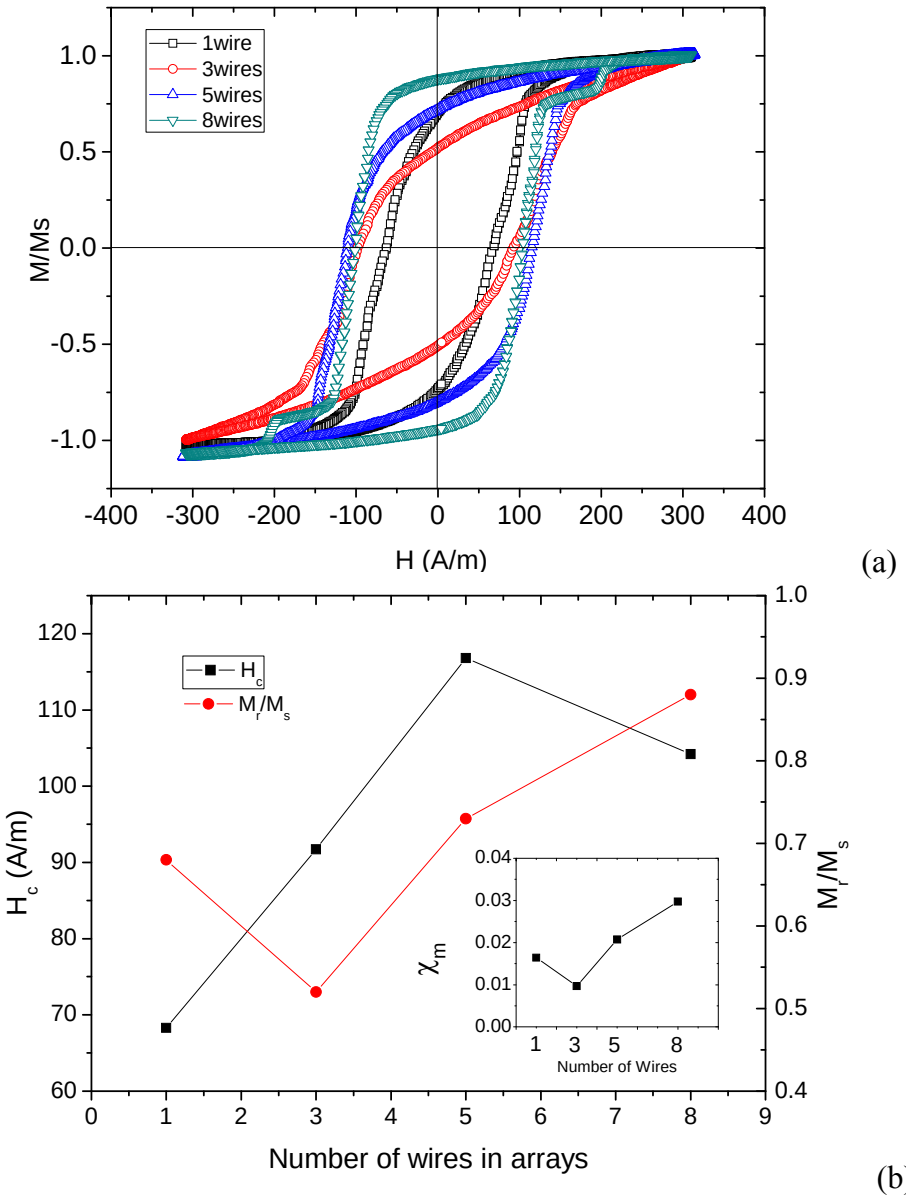

Fig. 4.17 Longitudinal hysteresis loops of the microwire arrays; (b) dependence of coercivity and remanent magnetization on the number of the wires in the microwire arrays. [135]

4.2.2 MI effect

4.2.2.1 MI ratio of single CW

Magnetoimpedance (MI) effect of single NiFe/Cu composite wire with length of 18 mm and permalloy thickness of 2.5 μm has been studied. The output was either the impedance of the core itself in MI transverse mode or impedance of the axial coil in MI axial mode. The main disadvantages of MI sensors are their non-linear characteristics that are changing with the amplitude of the measuring current. This indicates that the observed effect is not simple giant magnetoimpedance (GMI). GMI effect is a change of the high-frequency impedance of ferromagnetic wire with the measured DC axial field. GMI is based on eddy currents and the effect does not depend on the amplitude of the current which is used to measure the impedance [136]. The current level we used is higher than that for basic GMI so that the wires were saturated by the current induced field.

1) Transverse MI mode

In this mode the measuring current is flowing through the sensor core exactly as the excitation current in the transverse fluxgate. The sensor output is the voltage drop on the core. The advantage of this mode is the simplicity of setup - no coil necessary for the signal pickup and the disadvantage is low sensitivity and the influence of the contact resistance. As the MI sensor characteristics are measured by the impedance analyzer, they are usually plotted as impedance Z or its components L_s and R_s. Fig. 4.18 shows the frequency dependence of this effect for measuring current, or excitation current I_e = 20 mA. $L_s(f)$ and $R_s(f)$ curves are shown for B = 0 and B = 60

μT. The maximum sensitivity was achieved for 1 MHz. Fig. 4.19 shows the dependence of L(B) on the external magnetic field for f = 500 kHz. In this frequency, the CW can be also working in orthogonal fluxgate mode. The curves were measured for I_e = 3 mA and I_e = 20 mA to show that unlike the ordinary GMI there is an optimum amplitude of the measuring signal. The substantial non-linearity with two pronounced peaks is an attribute of this kind of sensor. Double peak is typical for samples with transversal magnetic anisotropy [137].

From Fig. 4.19 the effective sensitivity S_{MI} can be estimated in the transverse MI mode: for the measuring current I_e = 20 mA and measured field B_0 = 400 μT the change of the impedance is ΔL = 0.5 μH, which corresponds to the output voltage change of $\Delta V = 2\pi f \Delta L\, I_e$ = 30 mV, thus S_{MI} = 30 mV/400 μT = 75 V/T.

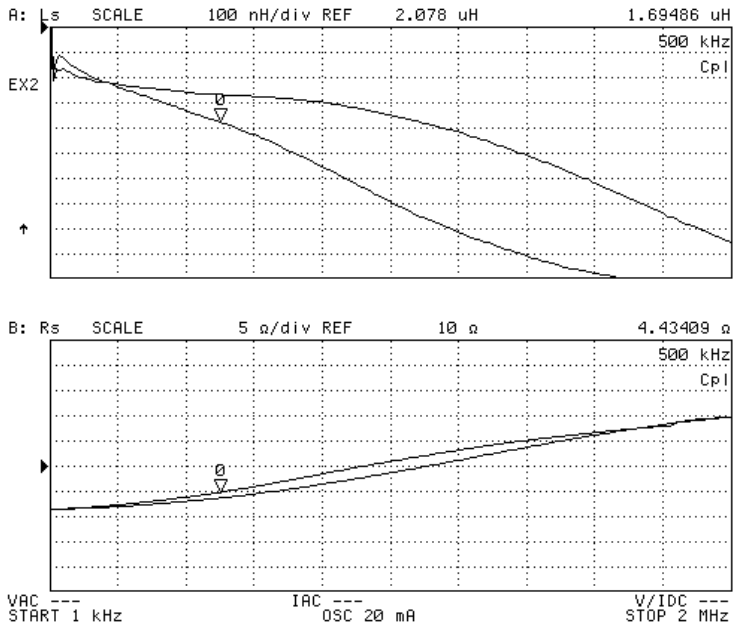

Fig. 4.18 Transverse MI frequency characteristics for B=0 (upper curve) and B = 60 μT (lower curve) when excitation current I=20mA.

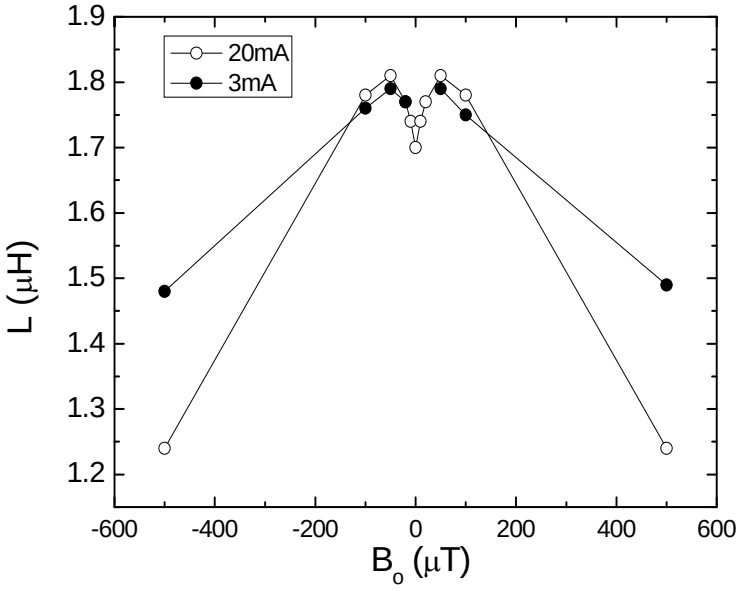

Fig. 4.19 Transverse MI curve at 500 kHz

Transverse GMI measurements performed on electrodeposited wires were also shown in [138]. The wires had similar composition, but the diameter was much larger than our CWs: 50 μm diameter Cu wire substrate and 10 μm NiFe layer.

2) Axial MI mode

In this mode the sensor output is the impedance of the solenoid coil. This means that there is no current through the sensor core, which thus needs no electric contacts. Fig. 4.20 shows an example of the axial MI characteristics measured at 500 kHz: the coil impedance is plotted as a function of the measuring current for $B_0 = 0$ (lower curves) and $B_0 = 500$ μT (upper curves). The maximum sensitivity was achieved for $I_e = 15$ mA and the achieved impedance change was 40 μH / 500 μT, which corresponds to

the output voltage $V = I \cdot \Delta L \cdot \omega =$ 1.8 V. The effective voltage sensitivity is thus S = 3600 V/T, about one third of the sensitivity in fluxgate mode.

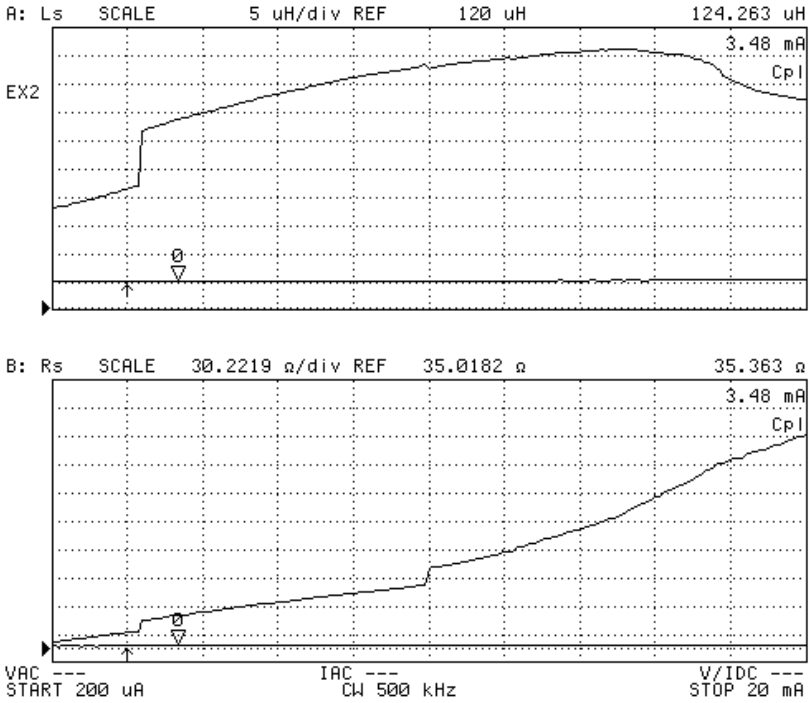

Fig. 4.20 Axial MI curves L_s amd R_s as a function of amplitude of the measuring current. The curves were measured at 500 kHz for $B_0 = 0$ (lower curves) and $B_0 = 500$ μT (upper curves)

4.2.2.2 MI ratio of CW arrays

MI ratios of CW arrays with different number of wire and structures are shown in Fig. 4.20. The maximum MI ratio decreases with the increase of the number of wires, which shows different trend compared with reported results [131]. Moreover, interaction between the multiple wires in the micro-wire arrays can be conjectured from the MI results as shown in Fig. 4.21. Compared with the MI profile of single

wire in Fig. 4.21 (a), it can be seen that the peak field in the MI curves in 3-wire array (Fig. 4.21 (b)) is much larger than single wire sample. This means the anisotropy of the 3-wire array is more in circumferential direction than that of single wire sample. This phenomenon has been verified by the longitudinal hysteresis loops discussed in section 4.2.1.2. Since the wires are fabricated in the same conditions, the anisotropy of each wire is almost same. A reasonable explanation is that the interaction effect enhances the circumferential anisotropy of the whole structure of the 3-wire array, which will change the magnetic property of the sample. However, the 5-wire array and 8-wire array show similar anisotropy structure with single wire, which means that compact structures act more like single wire than planar structures. This provides a hint to understand the interaction between micro-wires in the arrays which will be discussed in section 6.2.2.

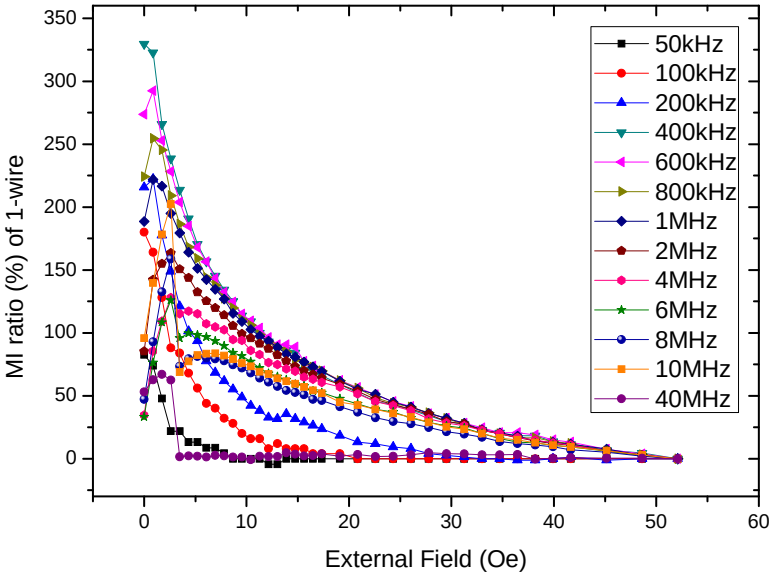

(a)

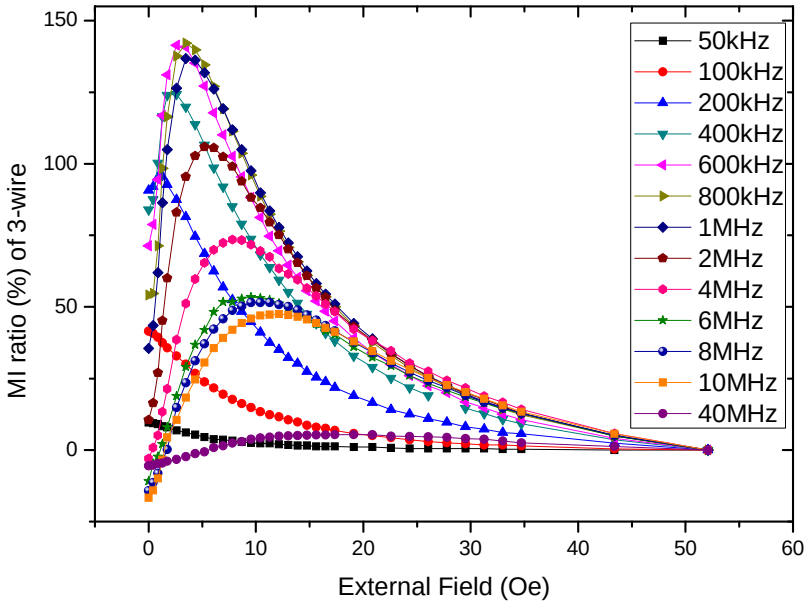
MI ratio (%) of 3-wire
External Field (Oe)
50kHz
100kHz
200kHz
400kHz
600kHz
800kHz
1MHz
2MHz
4MHz
6MHz
8MHz
10MHz
40MHz

(b)

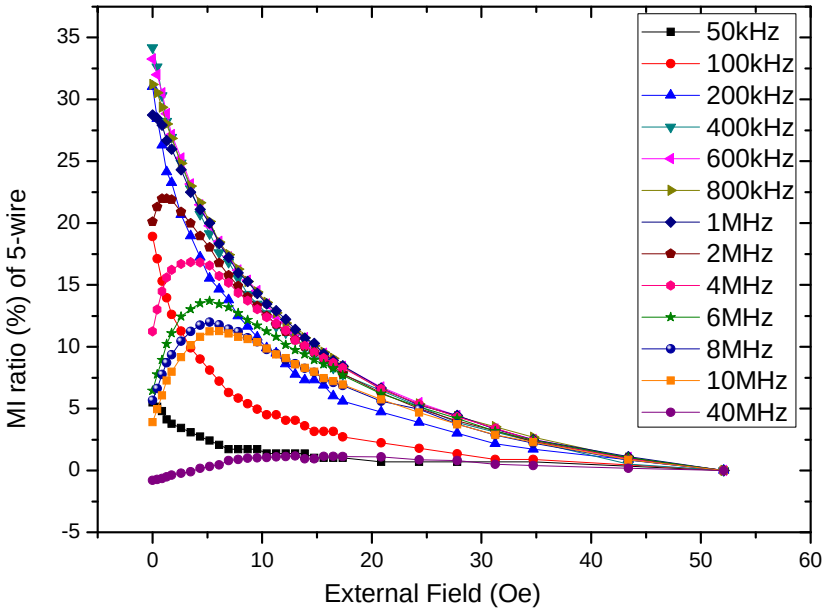
MI ratio (%) of 5-wire
External Field (Oe)
50kHz
100kHz
200kHz
400kHz
600kHz
800kHz
1MHz
2MHz
4MHz
6MHz
8MHz
10MHz
40MHz

(c)

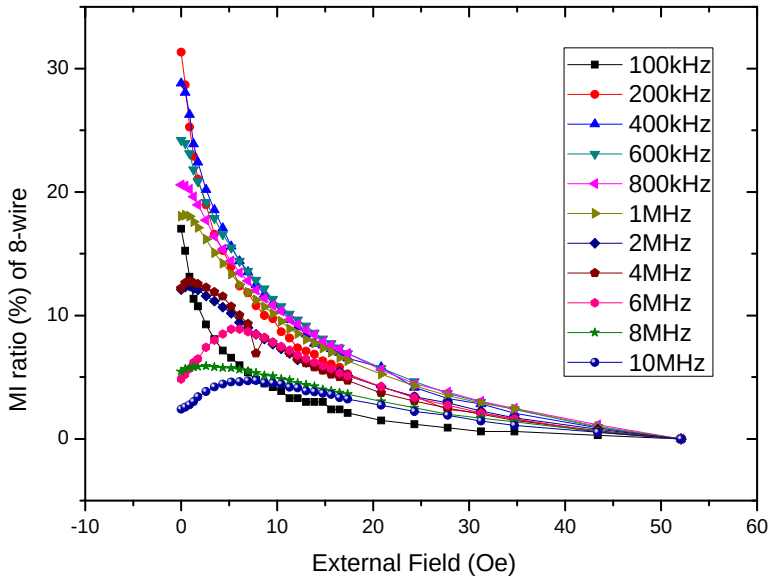

(d)

Fig. 4.21 MI ratio of micro-wire arrays: (a) single-core, (b) 3-wire, (c) 5-wire, and (d) 8-wire

4.3 Summary

The magnetic properties of the micro-wire arrays used in multi-core orthogonal fluxgate are pivotal to the sensor performance. Investigation on the magnetic properties of the micro-wires in form of single wire and multiple-wire arrays have be conducted by measuring the hysteresis loops and magneto-impedance ratios. The dependence of magnetic properties of two kinds of micro-wires, i.e. GCAWs and CWs, on their physical dimensions and structures has been studied.

CoFeSiB GCAW with near zero magnetistriction is kind of ferromagnetic micro-wire with desirable magnetic properties for sensor applications. The magnetic anisotropy of the wire depends on the coupling of magnetostriction and internal

stresses. Results showed that the anisotropy can be tailored by varying the ratio of glass coating layer to the metal core radius due to the fact the this ratio characterizes the stress in the ferromagnetic core. The larger the ratio, the smaller the angle between the easy axis of anisotropy and circumferential direction. Further study showed that the length of the wires can influence the anisotropy direction of the micro-wires originally with helical anisotropy. Shortening the length below a critical value changed the anisotropy direction from helical to circumferential. This phenomenon can be explained by the end domains in the wires that have significant circumferential anisotropy. The critical length is around 10 mm for both GCAWs and CWs.

The hysteresis loops of GCAW and CW arrays have been measured in variation of the number of the wires. For GCAWs with circumferential anisotropy, the easy axis of the anisotropy inclines more to the circumferential direction with the increase of the number of wires and the dynamic hysteresis loops showed that an ac current flowing into the arrays exasperates such effect. This effect can be explained by a domain unification mechanism in which the circular domains can be enlarged by the interdomain wall movement caused by the interaction between wires. For CWs, the anisotropy variation is just in opposite – the original helical anisotropy inclines to longitudinal direction with the increase of the number of wires. This is also due to the interaction between wires in which the longitudinal domains are enlarged.

MI measurement of GCAW and CW arrays confirmed the anisotropy of the arrays and presented the dynamic magnetic properties. In both cases, with the number of the wires increases, the frequency of the maximum MI ratio decreases resulting

from the decrease of the domain wall motion frequency due to the enlarged domain dimensions by the interaction between wires.

Chapter 5

Orthogonal Fluxgate Effects

5.1 Introduction

Orthogonal fluxgate effect, transducing magnetic flux to electromotive force, is similar to parallel fluxgate effect in terms of working mode and signal readout. However, they are quite different in the excitation mechanism and sensing element structure. Characterization of the orthogonal fluxgate responses of sensing elements with single wire and structured arrays is the basis for the research and development of orthogonal fluxgate magnetometers. Investigation of the effect of working mode, excitation current, and parameters of pickup coil on the orthogonal fluxgate effect will provide the necessary knowledge, especially when novel materials, i.e. ferromagnetic micro-wire arrays with tailored magnetic properties are used as the multi-core sensing element. Using multi-core sensing element in forms of micro-wire arrays is a novel approach to enhance the sensitivity and noise performance of the orthogonal fluxgate sensors. The sensitivity can be increased exponentially and the noise level can be well controlled. The physics mechanism behind the effect is still under study and the magnetometer based on the multi-core approach has been developed.

In the section 5.2, firstly the orthogonal fluxgate responses are introduced in terms of working mode and effect of excitation current. The parameters of pickup coil have been investigated for the optimum design. Sensitivity and noise characterization of the multi-core sensing element based on GCAWs and CWs are presented in section 5.3 and 5.4. Finally the preliminary experimental study of the interaction in the multi-core structure is presented in section 5.5.

5.2 Orthogonal Fluxgate Responses

5.2.1 Fundamental and 2nd harmonic working modes

In the fundamental mode, the sensor is based on unipolar saturation: the sensor gives output signal at the excitation frequency [53]. This mode is obtained by applying a large enough dc current to the sensing core to induce a biasing field on the core. The amplitude of ac excitation current could not exceed the dc current. Thus, the excitation field varies within the positive region but still the flux density changes in the circumferential direction. It was reported that the fundamental mode has smaller noise level compared to 2nd harmonic mode [58].

The gating curves, or called transfer function [4], of the fluxgate sensors present the characteristics of the sensing process. It demonstrates the dependence of the axial magnetic field in the core on the excitation current (or the excitation field) for given value of external dc measured axial field B_0. Gating curves clearly reveal

the operational mechanism of the orthogonal fluxgate: when the sensing element is periodically magnetized in circumferential direction, the axial flux changes simultaneously.

5.2.1.1 Orthogonal fluxgate response of GCAWs

The gating characteristics of CoFeSiB GCAWs of 23 μm in diameter and 18 mm in length have been studied. The pick-up coil has 750 turns. Fig. 5.1 shows the excitation current and output voltage waveforms in untuned second harmonic mode at 40 kHz. Fig. 5.2 shows the corresponding gating curve. The height of this curve corresponds to the change of the core axial field ***B*** during the excitation cycle. The axial field ***B*** is calculated as an integral of the voltage on sensing coil, divided by the effective core cross sectional area and number of turns.

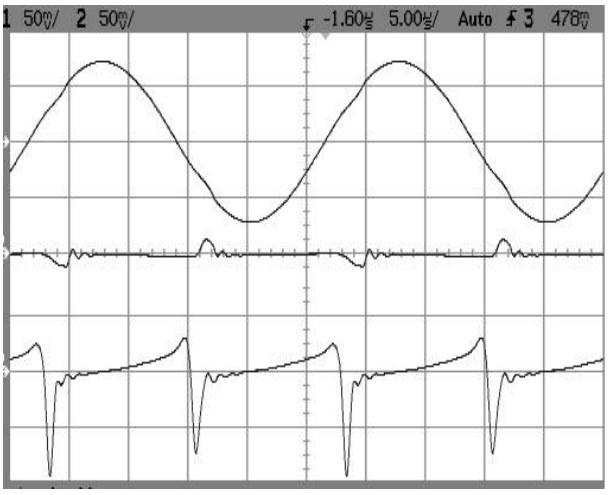

Fig. 5.1 Excitation field and induced voltage, Waveforms of un- tuned sensor (5 mA rms, 40 kHz):Upper trace: Iexc (5 mA/div); Mid trance: Vout (B =0;)Lower trace: Vout (B = 60μT)

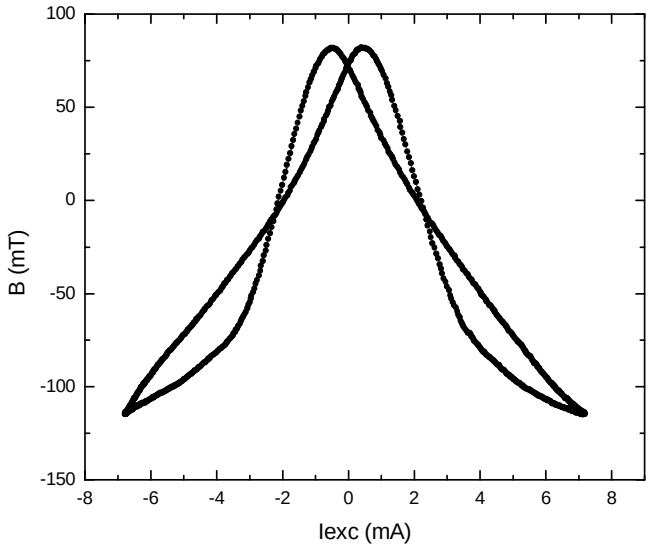

Fig. 5.2 Gating curve for B_0 = 60 μT, f_{exc} = 40 kHz, I_{exc} = 5 mA rms, unturned.

When the coil is tuned to resonance, the coil voltage is no longer proportional to the derivative of flux. Thus the apparent gating curves which still remain as a valuable tool for optimization of the sensor parameters, do not give correct information about the coil flux. The apparent gating curves are presented in Fig. 5.3 and Fig. 5.4 which show apparent and real gating curves for tuned and untuned mode respectively. Note that the real gating curve was obtained from a 10 turns of pick-up coil to avoid the parasitic self-capacitance tuning effect. Fig. 5.5 shows the waveforms of tuned 2nd harmonic mode, from which we could observe the saturated point of the excitation field and the dependence of output signal on the external field.

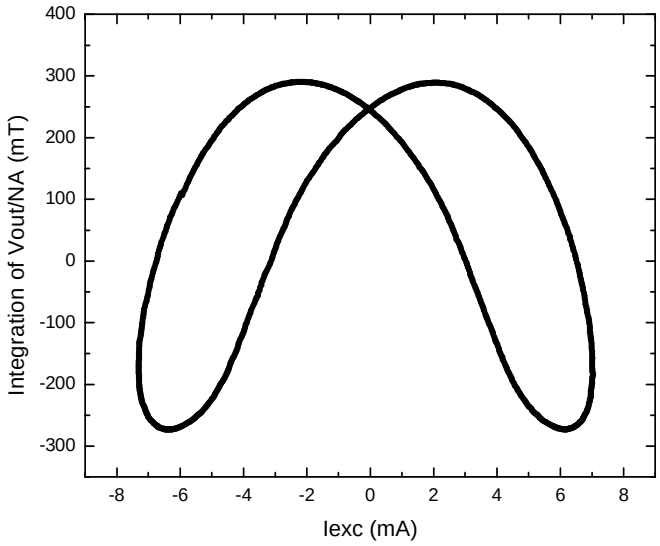

Fig. 5.3 Apparent gating curve for B_0 = 60μT, fexc = 500 kHz, Iexc = 5 mA rms, tuned.

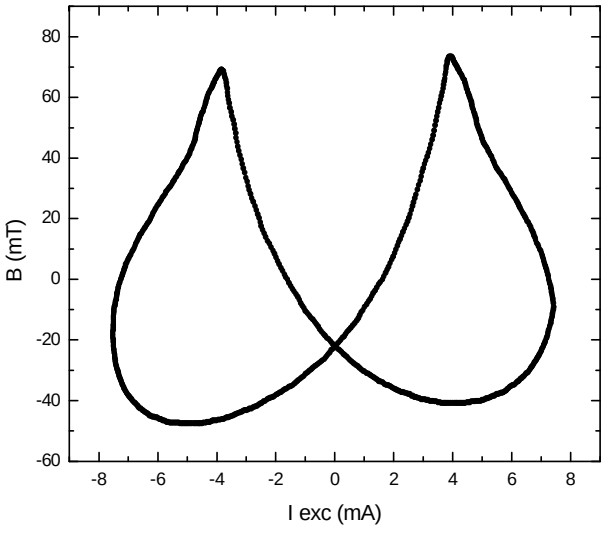

Fig. 5.4 Real gating curve for same case as in Fig. 5.2.

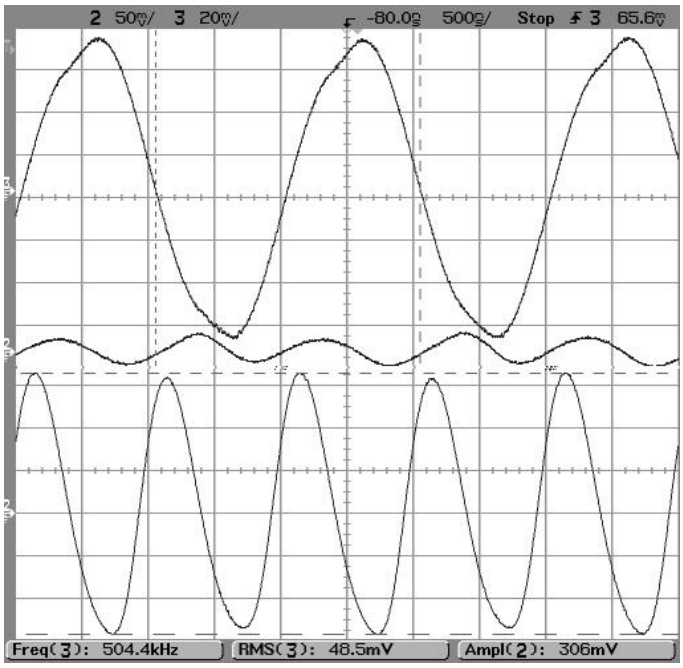

Fig. 5.5 Waveforms of tuned sensor (5mA, 500kHz), Upper trace: I_{exc} (2 mA/div); Middle trace: V_{out} (B = 0); Lower trace: V_{out} (B = 10 μT)

Fig. 5.6 shows the comparison of 2nd harmonic mode and fundamental mode in different bias current I_{dc}. Fig. 5.7 is the apparent gating curve of tuned fundamental mode.

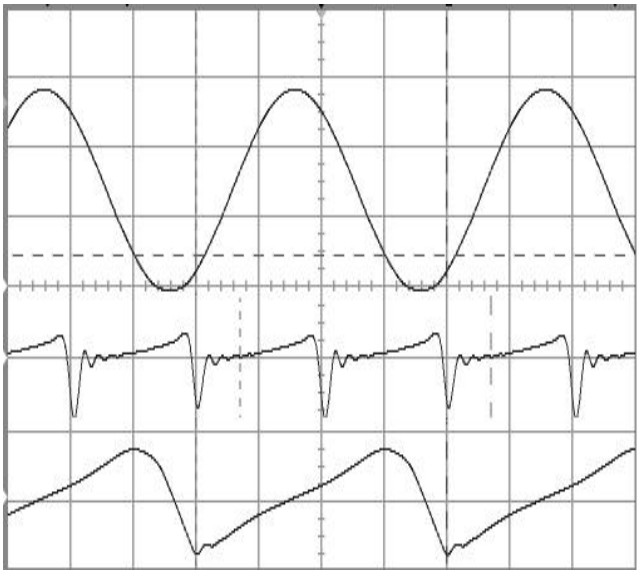

Fig. 5.6 Comparison of output waveform in untuned 2nd harmonic and fundamental modes (50 kHz, B_o = 60μT). Upper: I_{exc} (5 mA/div); Mid: 2nd harmonic mode (I_{dc} = 0); Lower: fundamental mode (I_{dc} = 6.7 mA)

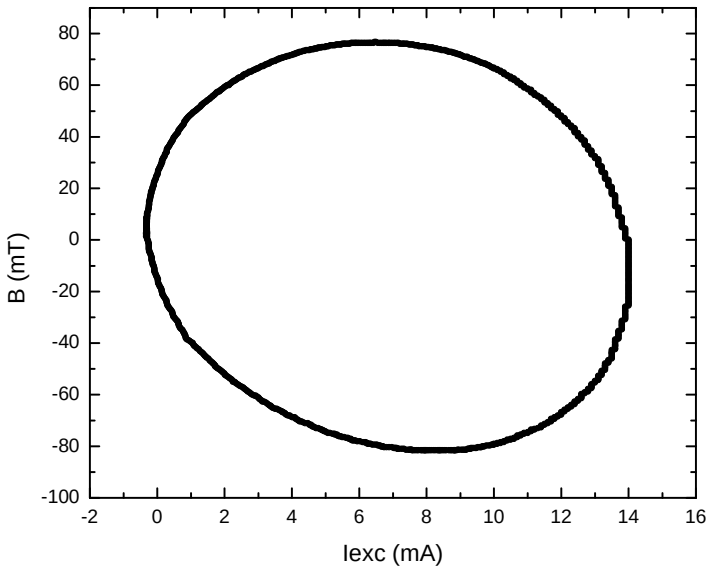

Fig. 5.7 Apparent gating curve for B_0 = 10 μT, f_{exc} = 900 kHz, I_{exc} = 5 mA rms, I_{dc} = 6.7mA, tuned mode.

5.2.1.2 Orthogonal fluxgate response of CWs

Fig. 5.8 shows the important waveforms of the fluxgate sensor using CWs as the sensing element working in the untuned transverse fluxgate mode: the excitation current (upper trace), output voltage induced into the pick-up coil (lower trace) and axial flux obtained by numerical integration of the output voltage (middle trace). The DC axial measured field was B_0 = 60 μT. From these waveforms we can plot the gating curve: dependence of the axial flux on excitation current (which is proportional to radial field intensity). Gating curve corresponding to Fig. 5.8 is shown in Fig. 5.9.

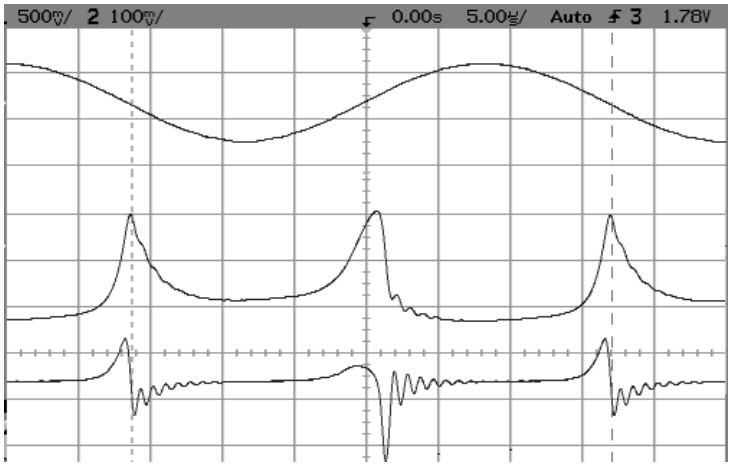

Fig. 5.8 Untuned sensor waveforms for external field B_o = 60 μT: excitation current (upper trace, 50 mA/div), axial flux (middle trace, 50 nWb/div), output voltage (lower trace, 100 mV/div)

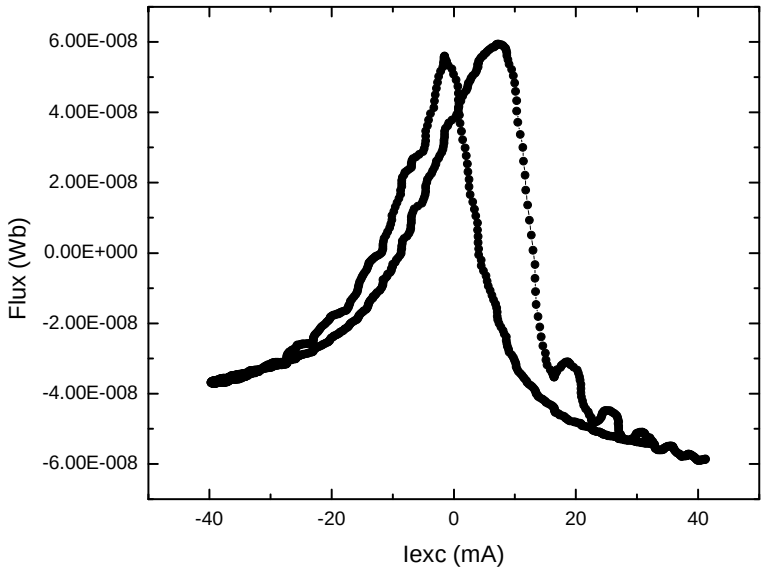

Fig. 5.9 Gating curve for untuned fluxgate response in Fig. 5.8.

Note that the motion of the instantaneous working point along the gating curve is changing speed: the sensor spends most of the period in radial saturation referred to "low flux state"; the "high flux state" corresponds to low excitation current and high axial permeability. Ideally the low flux value is zero; in reality it is an air flux through the pick-up coil. It cannot be neglected as the coil cross-sectional area is much higher than that of the ferromagnetic material. The difference between low flux and high flux state is proportional to the measured field. In this case the difference $\Delta\Phi$ is about 10^{-7} Wb. Taking into account the axial cross-section of magnetic layer ($A_{ax} = 1.73 \cdot 10^{-10}$ m^2), the magnetic field change during one cycle is $\Delta B = \Delta\Phi / NA_{ax} = 0.58$ T. From that we can estimate the axial effective permeability $\mu_{ax} = \Delta B / B_0 = 9700$.

The sensor sensitivity can be significantly increased by tuning the pick-up coil – either by external capacitor, or at higher frequencies by the coil self-capacitance, which however may be temperature dependent. Fig. 5.10 shows sensor waveforms for 70 kHz excitation frequency, where the value of the parallel capacitor is 6.8 nF for tuning at 2nd harmonics. The corresponding virtual gating curve is shown in Fig. 5.11. The vertical axis of this curve is again integrated output voltage, but because of the parametric amplification which occurs in the tuned circuit, the voltage integral it is no longer equal to the core flux.

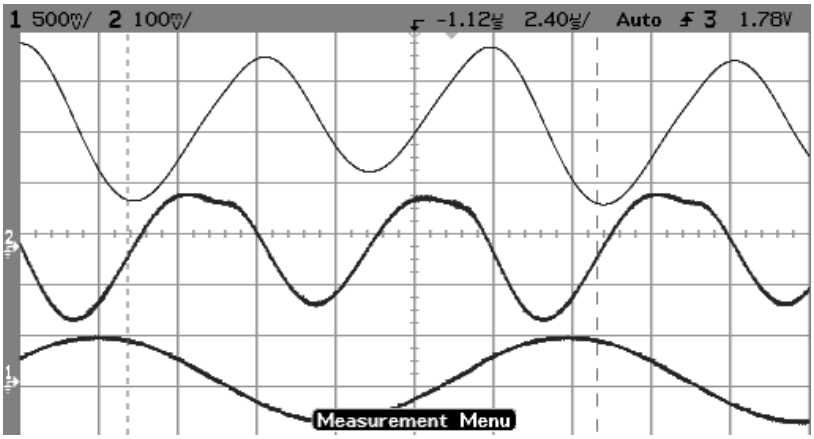

Fig. 5.10 Tuned sensor excited at 70 kHz, excitation current (lower trace, 50 mA/div), integrated output voltage (virtual axial flux) (upper trace, 100 nWb/div), and output voltage (middle trace, 100 mV/div).

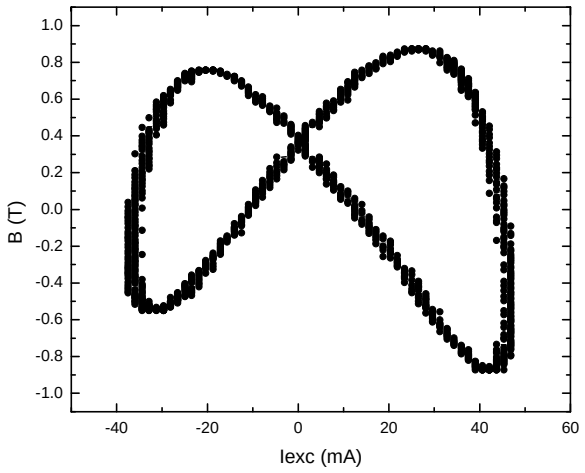

Fig. 5.11Virtual gating curve for tuned sensor in Fig. 5.10.

Fig. 5.12 shows the original tuned fluxgate waveforms in different external fields with excitation current of 10 mA rms in 490 kHz tuned by coil self-capacitance. The corresponding gating curve is shown in Fig. 5.13. Note that in this method the sensitivity can be enhanced much higher than tuning with external capacitor since the working frequency can be much higher.

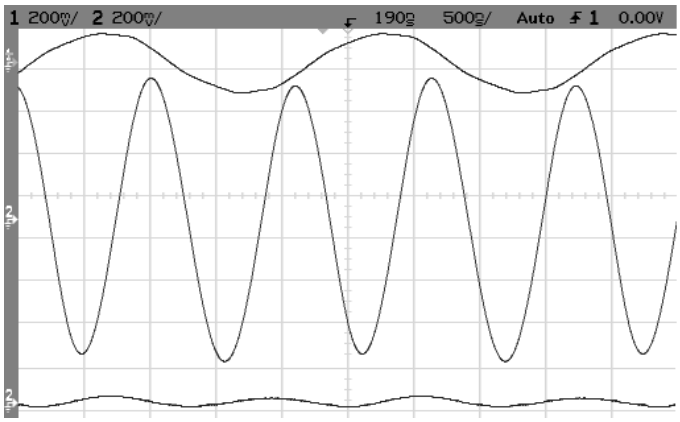

Fig. 5.12 Waveforms of tuned sensor at excitation current I_{exc} = 10 mArms, 490 kHz. Upper trace: I_{exc} (20 mA/div); Middle trace: output voltage V_{out} (200 mV/div) at external field B_o = 50 μT; Lower trace: output V_{out} (200 mV/div) at B_o = 0.

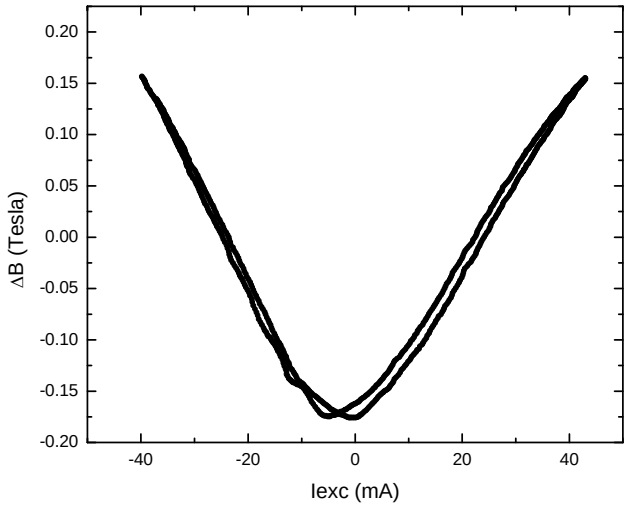

Fig. 5.13 Gating curves of the sensor working in the second-harmonic mode and tuned by self-capacitance as shown in Fig. 5.12.

5.2.1 Excitation Current

The open-loop characteristics of the sensor tuned by self-capacitance are shown in Fig. 5.14 for two kinds of sensing elements. Note that at the same excitation current frequency, the sensor using electroplated CWs could obtain higher sensitivity in the weak field than the sensor using GCAWs.

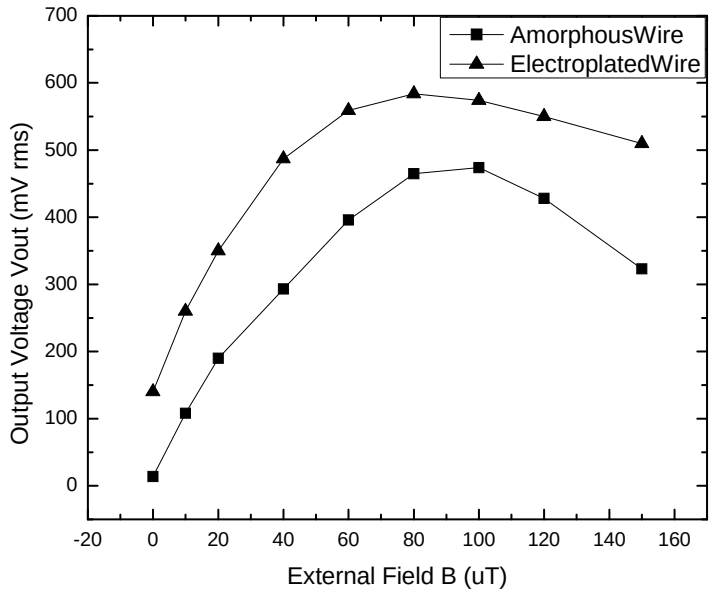

Fig. 5.14 Open-loop characteristics of tuned sensor. Excitation current for amorphous wire: 500 kHz, 5 mA rms; for electroplated wire: 500 kHz, 20 mA rms

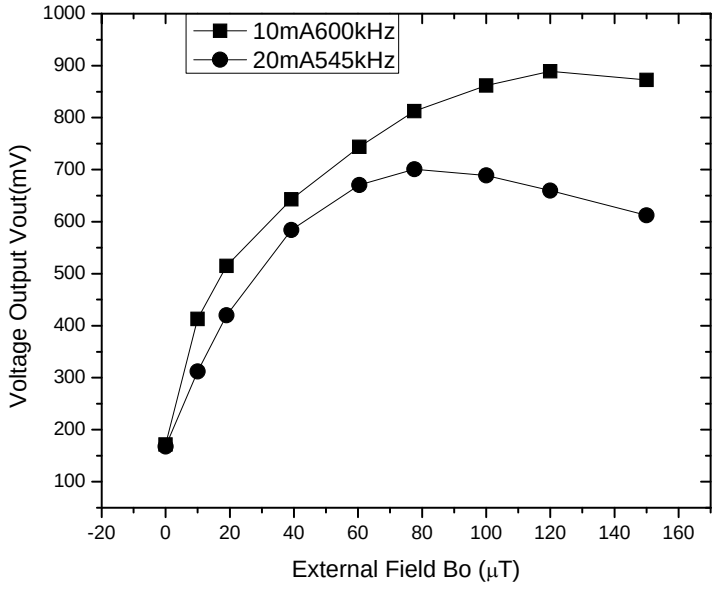

(a)

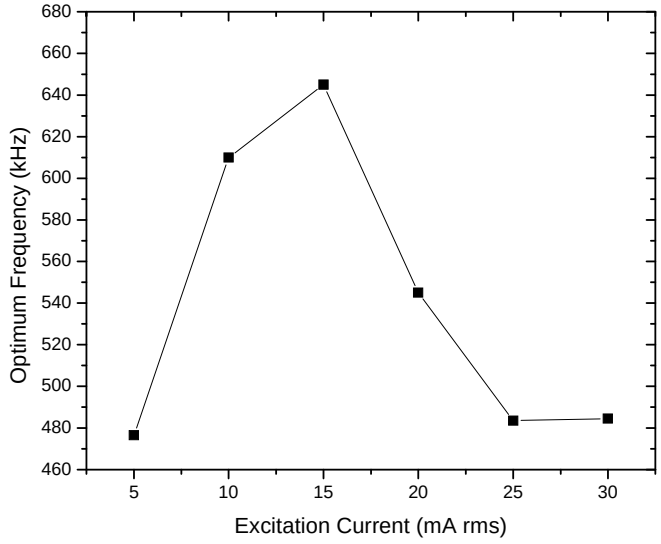

(b)

Fig. 5.15 (a) Dependence of the sensor output on the external field at 545 kHz and 600kHz. (b) Dependence of optimum frequency on the excitation current amplitude.

As proved in [88] by means of transverse Kerr effect (TKE), the composite wire shows near-surface circular domains with alternating left- and right-handled magnetization. When a current flowing through the wire a circular magnetic field will be set up to magnetize the permalloy layer. The magnetization vectors of the domains incline a certain angle to the wire axis due to the helical anisotropy. Initially the excitation current causes the domain wall movement occur, which results into the net magnetization along the longitudinal direction. With the increase of the excitation current, the domain magnetizations rotate gradually to the circular direction, which

reduces the longitudinal net magnetization. This alternating net magnetization by the excitation ac gives rise to the even harmonic signals induced in the pickup coil.

The dependence of the sensor output on the external field with various excitation ac current amplitudes was studied. Fig. 5.15 (a) shows that when applying a small excitation current (10 mArms), the sensor could obtain a higher sensitivity at higher frequency. Further increase of the current amplitude (20 mArms) could not improve the sensitivity, because the optimum working frequency was reduced. The dependence of optimum frequency (i.e. frequency at which the sensitivity is maximized) on the excitation current amplitude is shown in Fig. 5.15 (b). For ac amplitudes of 10 mArms and 20 mArms, the optimum frequencies were 600 kHz and 545 kHz, respectively. In general the frequency dependence of the sensor sensitivity is complex as it is caused by frequency dependence of incremental permeability and also by eddy currents (which also depend on permeability). In this case the sensor is tuned and also the quality factor of the resonant circuit is frequency dependent.

Fig. 5.16 shows the sensor sensitivity and perming error [4] as a function of excitation amplitude. The sensor was excited at 600 kHz and tuned by self-capacitance. It was found that there is optimum amplitude of the excitation current for the best sensitivity. The value for our sensing core is 10 mA rms. The perming error was investigated by applying magnetic field shocks (or pulses with the amplitude of

10 mT by a current-controlled Helmholtz coil), to the sensor and then calculating the offset change from the outputs. With the increase of the excitation current the perming error reduced. This trend corresponds to the case of solid core fluxgate sensors [4]. Compared with amorphous wires, the composite wires having the non-magnetic material (Cu) core for the sensing element have the advantage of lower perming errors due to the fact that the copper core avoids the magnetic remanence in the central portion of the sensing element during the magnetization reversal.

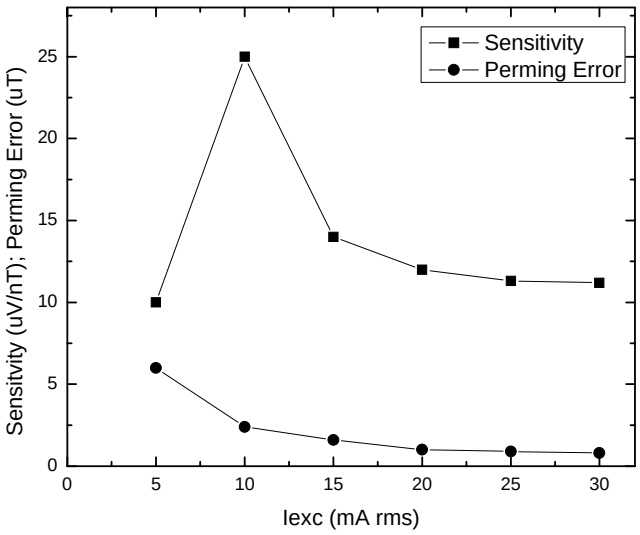

Fig. 5.16 Sensitivity and perming error of orthogonal fluxgate working at 600 kHz.

5.2.2 Parameters of Pickup Coil

The pick-up coil is the initial and essential readout component. Performance of the sensor relies partly on the electrical properties of the pick-up and process circuits, besides on the magnetic properties of the sensing element. A series of micro coils, as shown in Fig. 5.17, were wound onto a glass tube using an auto-coiling micro-wire machine. Results show that for the best sensitivity of the sensor, an optimal configure of all the physical parameters exists.

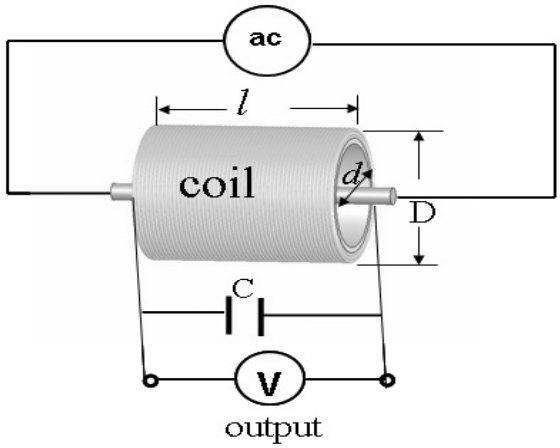

Fig. 5.17 Physical parameters of the pickup coil, including number of turns N, the length *l*, the inner and outer coil tube diameters d and D, diameter of the coil wire $d_{w.}$

5.2.2.1 Number of turns

The orthogonal fluxgate sensor output $V_{out}(t)$ is proportional to the number of turns N. $V_{out}(t)$ also depends on the resonant frequency, *f*, of the pick-up coil circuit. However, with the increase of N, the parasitic self-capacitance of the coil always increases, which decreases f. So, there is a limit of N.

With the small number of turns N, the sensitivity increases with N. Fig. 5.18 shows the sensor operating at 150 kHz with the output in variation with the number of turns of the coil. The coil length was fixed at 15 mm. This can be explained by the Faraday inductive law. The sensing output from the pickup coil will be

$$V_i = -\frac{d\phi}{dt} = -\frac{d(NA\mu(t)H_{ext}(t))}{dt} = -NA\left(H\frac{d\mu(t)}{dt} + \mu\frac{dH_{ext}(t)}{dt}\right) \tag{5.1}$$

where ϕ, A are the magnetic flux and cross section area of the coil, respectively. $\mu(t)$ and $H_{ext}(t)$ are the ac longitudinal permeability and the external magnetic field. It can be seen from the equation that the sensing output is directly proportional to the number of turns. Notice that the above equation will be complicated when we deduce the permeability in tensor form. The permeability is related to the frequency of the excitation current.

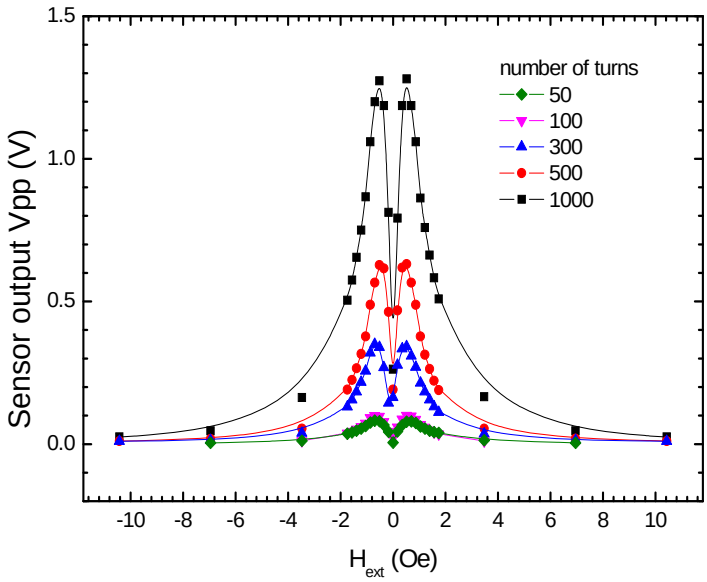

Fig. 5.18 Sensor output in variation with the number of turns of the pickup coil.

The parasitic self-capacitance also increases with N, which results in the lower resonance frequency of the pickup circuit. Thus, the sensitivity will drop. There is an optimal number of turns. This was observed when we compared the sensor output with variable N from 500 to 2000, shown in Fig. 5.19. The other parameters are fixed: coil length is 9 mm and coil tube inner diameter is 0.8 mm. The diameter of sensing core is 16 μm. For the later experiments, we use pickup coils in 1000 turns.

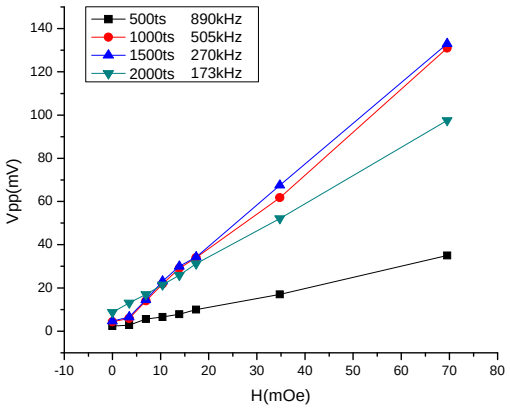

(a)

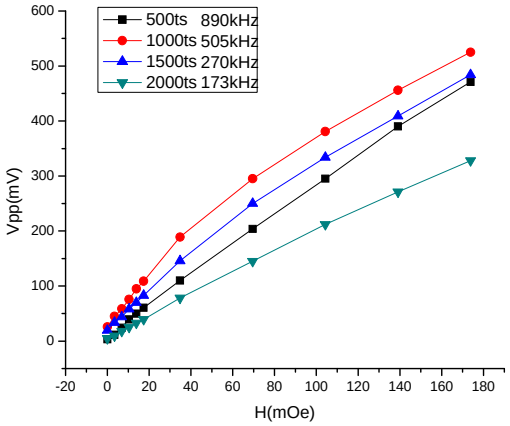

(b)

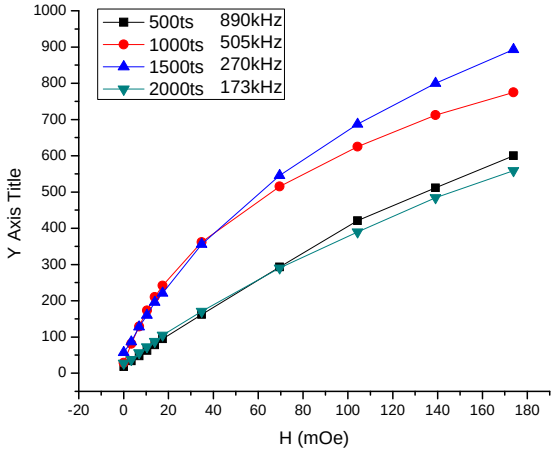

(c)

Fig. 5.19 Sensor output in variation with the number of turns of the the pickup coil,the excitation current are (a)5mA (b)10mA (c)15mA (rms)

5.2.2.2 Diameter of the coil wire

The effect of coil wire diameter on the sensor sensitivity was also investigated. Fig. 5.20 shows the sensor output curve in variation with the diameter of the coil wire at different driving current frequency for the sensing element. The number of turns of the coil was fixed at 1000 and the length of the coil is fixed at 1.5 cm. It can be observed that the smaller wire diameter of 80 μm gave the higher sensitivity for the sensor in comparison to the wire diameter of 200 μm.

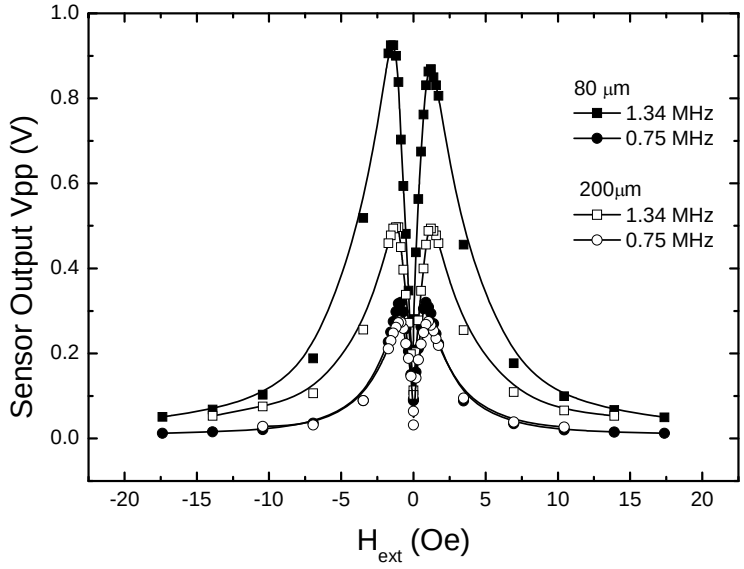

Fig. 5.20 Comparison of sensor output for different diameters of the coil wire.

5.2.2.3 Length of the coil

Fig. 5.21 shows the sensor output curve in variation with the length of the coil. One coil was longer than the length of the sensing element (10 mm) while another coil was shorter than the sensing element. The wire diameter was fixed at 80 μm and the number of turns was ensured to be 1000. The sensor with the shorter coil of 8mm gave larger output than the sensor with longer coil of 15mm. This could be that the shorter coil could avoid the non-uniformity of the sensing element during sensing (at the two ends of the sensing element, the permeability may be smaller because of demagnetization effect).

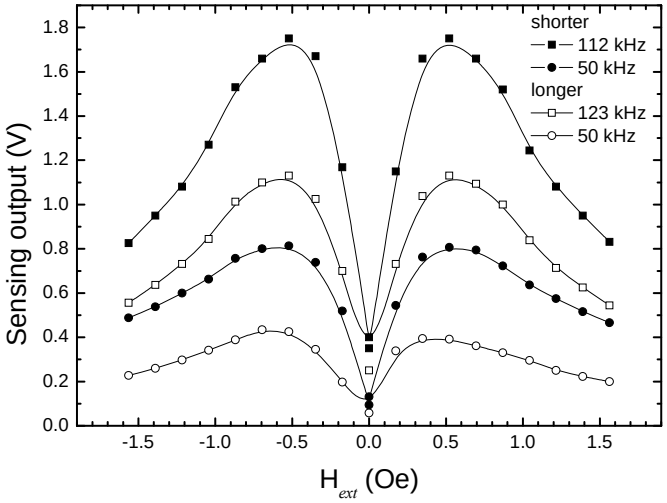

Fig. 5.21 Comparison of sensor output for different lengths of the coil.

5.2.2.4 Diameter of the coil tube

Fig. 5.22 shows the effect of the coil diameter on sensor output. The coils were ensured to be of the same length of 15mm and having the same number of turns of 50. The coil with the smaller diameter has the higher sensitivity. If the gap of the coil and sensing element is considered, then the equation (4.1) will be revised as

$$V_i = -N\left(\frac{d\left(A_0\mu_0 H_{ext}(t)\right)}{dt} + \frac{d\left(A_c\mu_r H_{ext}(t)\right)}{dt}\right) \tag{5.2}$$

where A_0 and A_c are the cross section area of the gap and the sensing element, and μ_0 and μ_r are the vacuum permeability and the longitudinal permeability of the sensing element respectively. Under the external magnetic field, the vacuum permeability

does not change. Therefore, the first term in the right bracket will be constant. That means that the gap between the coil and sensing element only arises from the shifting of the offset of sensing output. However, the larger diameter coil will use a longer coil wire which resulted in higher dc resistance and parasitic self-capacitance. These variations could have changed the resonance frequency and deteriorated the sensor sensitivity.

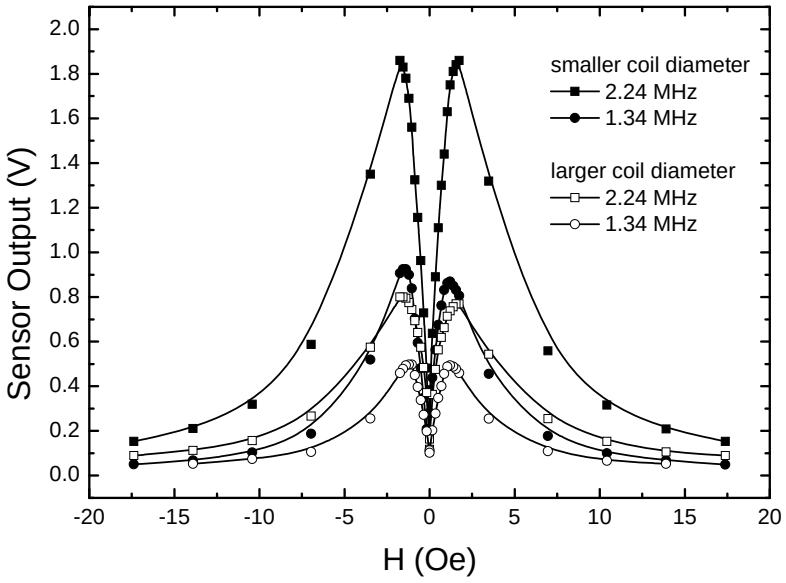

Fig. 5.22 Comparison of sensor output for different diameters of the coil.

5.3 Sensitivity Improvement using Multi-core Sensing Element

5.3.1 Sensitivity of single GCAW and CDAW

Fig. 5.23 shows the sensor output curves for sensors with different sensing elements driven by low and high frequency ac. The low frequency results were obtained using a 1000-turn pick-up coil, and the high frequency results were obtained using a 50-turn pick-up coil. In both cases the coil was connected to a low value capacitor in parallel. It can be seen that for each of the sensing elements, the sensing output displays a centrosymmetric curve about the origin, with a peak at certain external field. The sensor output came from the time-variable inductance of the micro coil. The variation of the magnetic flux of the coil with time induced a voltage between the ends of the coil, as shown in Eq. 5.1. The sensing element was subjected to two magnetic fields. One was the *ac* circumferential field induced by the driving current and another was the external magnetic field. Since the field to be measured was almost steady, the second term in the right bracket in Eq. 5.1 can be ignored.

In this case, the dynamic permeability is a tensor. Even without external magnetic field, the longitudinal permeability also varies with time, owing to the magnetization by the ac circumferential field. For zero instant value of the excitation field the longitudinal permeability is the maximum. For both positive and negative maximum of the excitation current the large part of the core volume is saturated in circumferential direction, so that the longitudinal permeability reaches its minimum twice in one period. That is why the output signal is at the second harmonics.

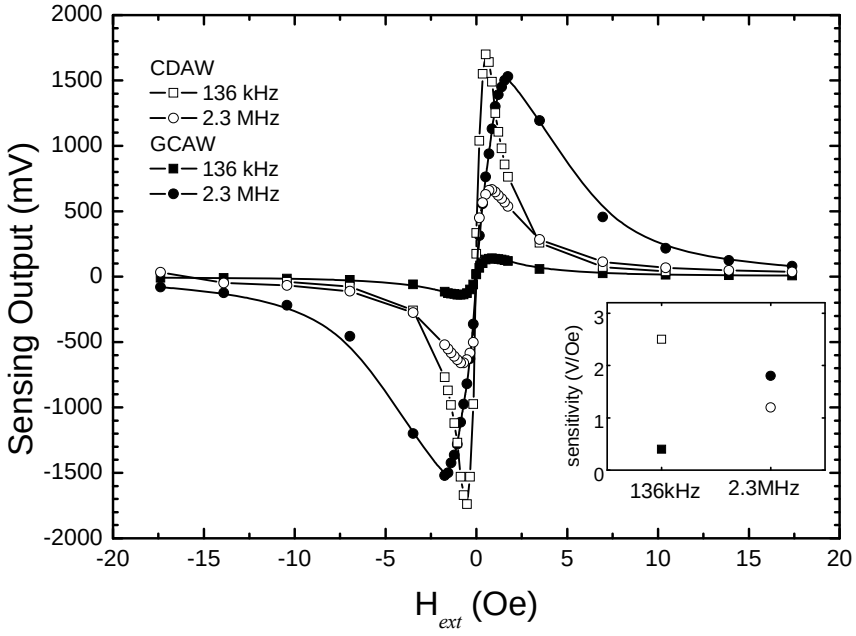

Fig. 5.23 Comparative study of sensor output for three different sensing elements: cold-drawn amorphous wire (CDAW) and glass-coated amorphous wire (GCAW). The inset shows the sensitivity of the sensors tested at low and high frequencies within the external field of 0.5 Oe.

In our case both wires have circumferential anisotropy. The sensitivity to the longitudinal external field is high due to the softness and the low demagnetization factor in this direction. When the sensing element was subjected to the external field, the circumferential permeability increased with increasing the field until reaching the circumferential anisotropy field of the element. After that, the circumferential permeability decreases with further increases of the external field. For higher values of the measured field this dependence has some effects on the waveform of the excitation field. Compared to circumferential permeability, the situation of longitudinal permeability was just opposite. For small values of the measured field the

permeability time dependence is not influenced, so that the induced voltage is almost linearly proportional to the measured field. For external field approaching anisotropy field the volume of the core which is saturated by the excitation field starts to decrease. This leads to increase of the minimum axial permeability and thus decrease of the sensitivity. As the sensitivity depends on the time derivative of the axial permeability, the mentioned dependence is not straightforward.

The higher driving frequency gives higher sensing output and sensitivity. This tendency can be explained by Eq. 5.2 and Eq. 5.3,

$$d\mu / dt \propto f_{dr} \tag{5.3}$$

where the differential result of permeability with respect to time is proportional to the driving frequency and so the output V_{out} is directly proportional to the driving frequency f_{dr}. It should be noted that at higher frequencies this tendency is influenced by other factors such as frequency dependence of permeability and quality factor of the resonant circuit at the output. This is shown in Fig. 5.23. For higher frequency the number of turns was proportionally lower, so ideally the voltage sensitivity would remain the same. The observed changes in sensitivity (increase for GCAW and decrease for CDAW) are caused by the mentioned second-order effects.

As observed in Fig. 5.23, both CDAW and GCAW showed very sharp output signal increase with increasing external magnetic field in the weak field range. At low frequency, the sensor with CDAW sensing element seems to have the best sensitivity. At high frequency, however, the sensor with GCAW sensing element has the higher sensitivity.

5.3.2 Nonlinear Increase of Sensitivity with multi-core GCAWs

To compare the sensing performance of the multi-core sensing element orthogonal fluxgate sensor with the traditional single-core sensing element orthogonal fluxgate sensor, these two kinds of sensors were constructed and tested. For both sensors, glass-coated CoFeSiB amorphous wires [9] were used for the ferromagnetic cores as the sensing element. Each of the glass coated wires was 18 mm in length, having a 16 μm diameter amorphous ferromagnetic core coated with a glass layer of 2 μm in thickness. The single-core sensor had the sensing element formed by one wire, whereas the multi-core sensor had the sensing element formed by 16 wires. A 1000-turn pick-up coil was used for both the single-core and multi-core sensors. The AC excitation current was supplied by a function generator, Agilent 33250A. The sensing output voltage was measured using an oscilloscope, Agilent 54624A. The AC passing through each of the ferromagnetic cores was controlled at 6 mA. Arrangements were made to keep the current density passing through each core remain unchanged as the number of cores increased in the sensing element. The frequency of excitation current used was the optimum in sensing a weak external field, which was determined by supplying a fixed external filed of small value, (e.g. 5 μT) to the sensor and then varying the frequency of the excitation current passing through the sensing element till the sensor's second harmonic output reached the maximum. The typical waveforms of the excitation current and output voltage for zero and non-zero measured field for the single-core sensor and 16-core sensor are shown in Fig. 5.24. The sensor output voltage was on the second harmonics. The sensitivity tests were conducted under shielding using a magnetic shielding cylinder. The external magnetic

field to be measured was generated using a Helmholtz coil connected to a high precision DC source, which generates magnetic field of densities ranging from 0 to 800 μT.

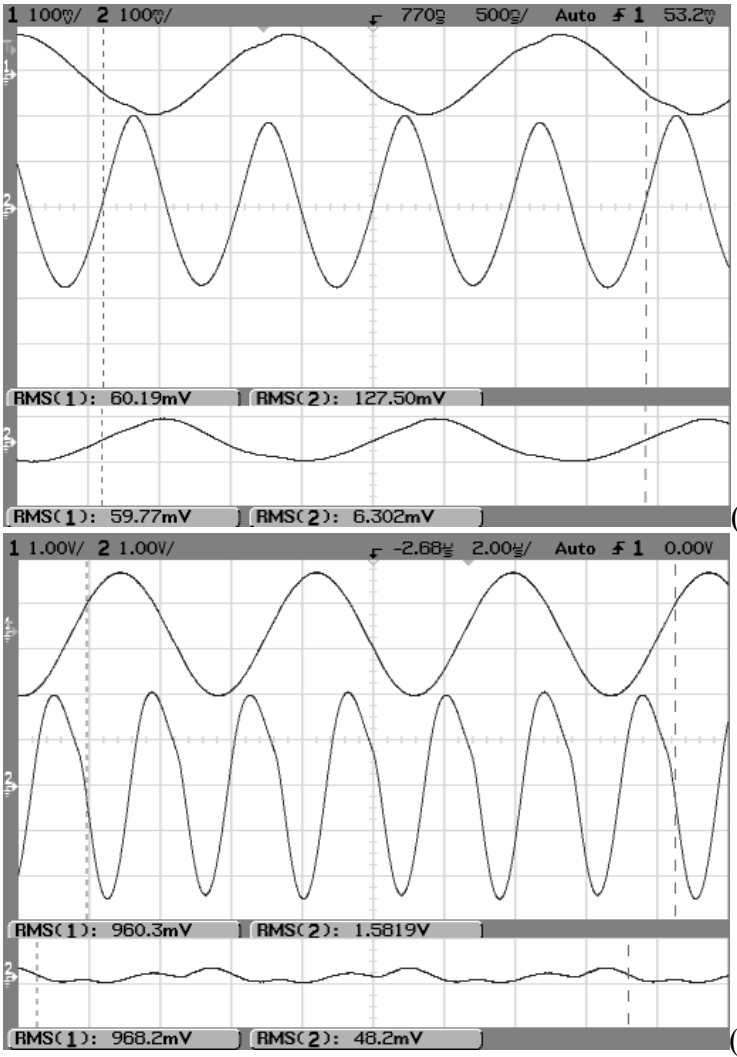

Fig. 5.24 Typical waveforms (please note the different scales) of the excitation current and output voltage for zero and non-zero measured field for the single-core sensor and 16-core sensor are shown in (a) and (b), respectively. (a) In the upper trace: I_{exc} =6mA rms (10 mA/div); in the middle trace: voltage output for 8A/m measured field (100 mV/div); in the lower trace: voltage output for zero measured field (20 mV/div). (b) In the upper trace: I_{exc}=96mA rms (100mA/div); in the middle trace: voltage output for 8A/m measured field (1V/div); in the lower trace: voltage output for zero measured field (500mV/div).

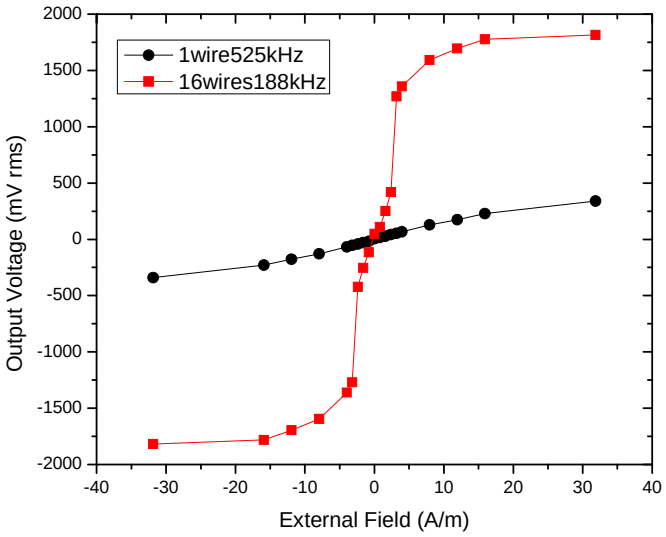

Fig. 5.25 Comparison of the sensing outputs of the single-core sensor and 16-core sensor. The sensitivities of the single core sensor and 16-core sensor at the external field of 4μT were 13 mV/μT and 850 mV/μT, respectively. Also, note that the optimum frequency for the 16-core sensor was lower than that for the single-core sensor.

As shown in Fig. 5.25, in measuring the external field of intensity ranging from 0 to 40 μT, the sensing output of the 16-core sensor in voltage increase was much larger than that of the single-core sensor. Under the excitation currents of 6 mArms at 525 kHz for the single-core sensor and 96 mArms at 188 kHz for the 16-core sensor, the sensor sensitivities at the external field of 4μT were 13 mV/μT and 850 mV/μT, respectively. The sensitivity of the 16-core sensor was 65 times higher than that of the single-core sensor. Fig. 5.26 shows that as the number of ferromagnetic wires in the sensing element increased, the sensitivity of the multi-core sensor increased

exponentially, which was very different from the linear increasing calculated by multiplying the sensitivity of a single-core sensor and the number of such sensors.

The sensor offset of the two sensors can be seen from Figs. 5.24 and Fig. 5.25. At the zero measured field, the single-core and 16 –core sensors had the outputs of 6.3 mV and 48.2 mV, respectively. The offset value increased with the number of cores increased from 1 to 16 at an average rate of 0.5, approximately. The linearity of the sensors can also be observed from Fig. 5.25. The overall sensing outputs of both single-core and 16-core sensors were non-linear. However, compared to the single-core sensor, the 16-core sensor has a highly linear output range corresponding to the measured field of 3 to 4 A/m. The perming errors for the single-core and 16-core sensors were also measured for comparison, which at 10 mT were 2 μT and 5 μT, respectively.

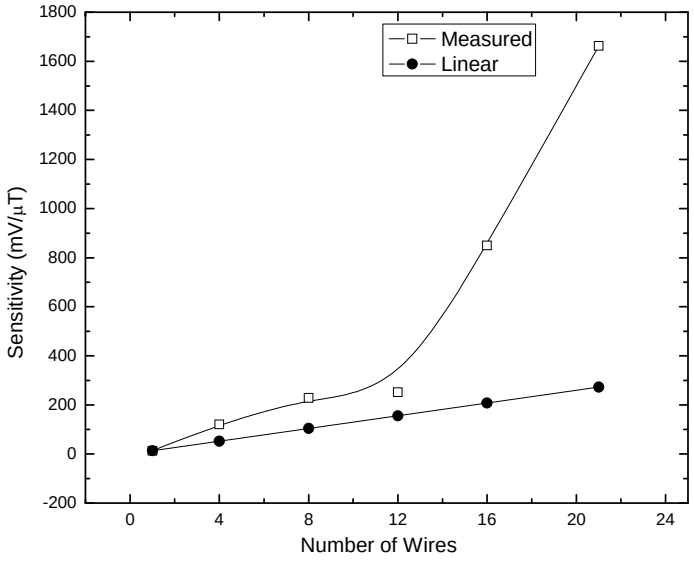

Fig. 5.26 The measured sensitivity of the multi-core sensor increased exponentially as the number of cores wires increased from 1 to 21. A “linear” curve calculated by multiplying the number of single-core sensors and the sensitivity of a single-core sensor is shown for comparison.

As shown in Fig. 5.27, for small number of wires and for the same external field varying from 0 to 40 μT, as the number of cores in the sensing element increased from 1 to 4, the sensing output voltage increased accordingly and significantly. Surprisingly, the sensitivity increase against the core number was not proportional (with constant ratio) but also exponential as shown in Fig. 5.28, which was in similar trend with that of Fig. 5.26.

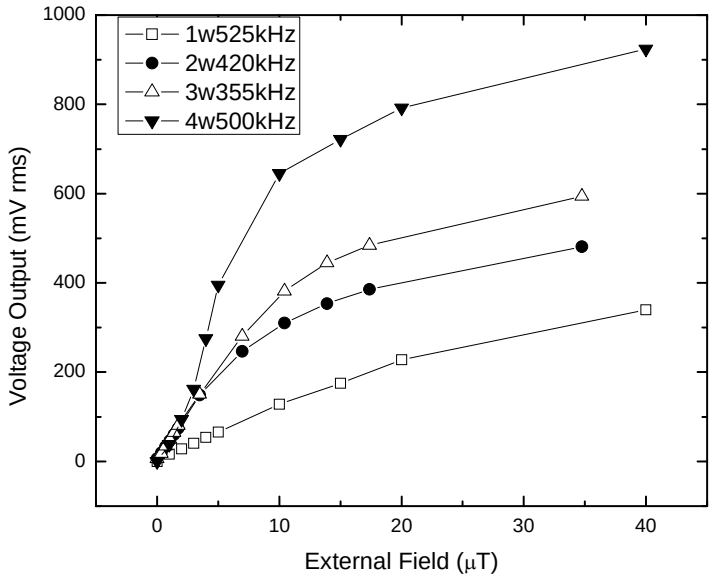

Fig. 5.27As the number of cores in the sensing element increased from 1 to 4, the output increased accordingly and significantly for the same field range of 0 to 40 μT.

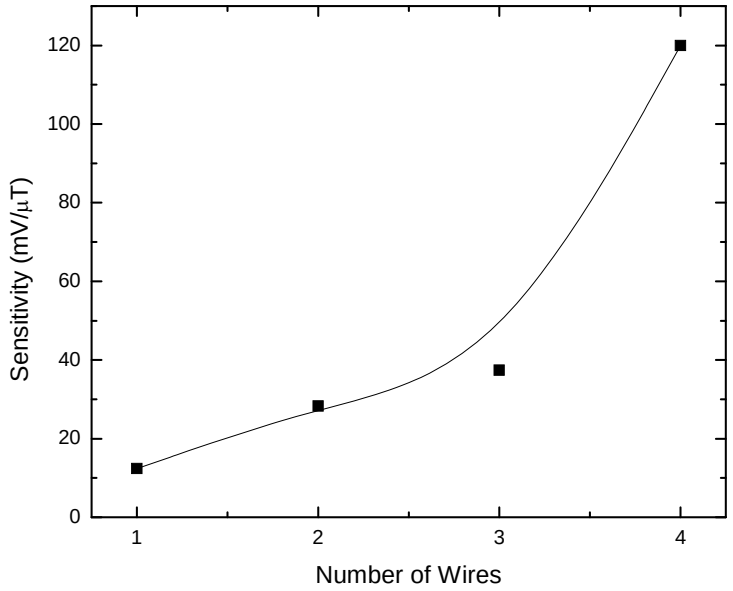

Fig. 5.28 The sensitivity, calculated as the average value of sensing output (shown in Fig. 5.27) for the external field varying from 0 – 5 μT, increased exponentially with the core number increase.

5.3.3 Sensitivity Resonance

To investigate such a dynamic magnetic interaction effect, sensing elements with larger number of ferromagnetic cores were constructed for testing. It was found that with larger number of cores packed in the sensing element, such as with 16 cores, there was a resonance with the sensing output, corresponding to a narrow range of external field, as shown in Fig. 5.29 (a). The resonance became more and more significant as the number of cores was increased.

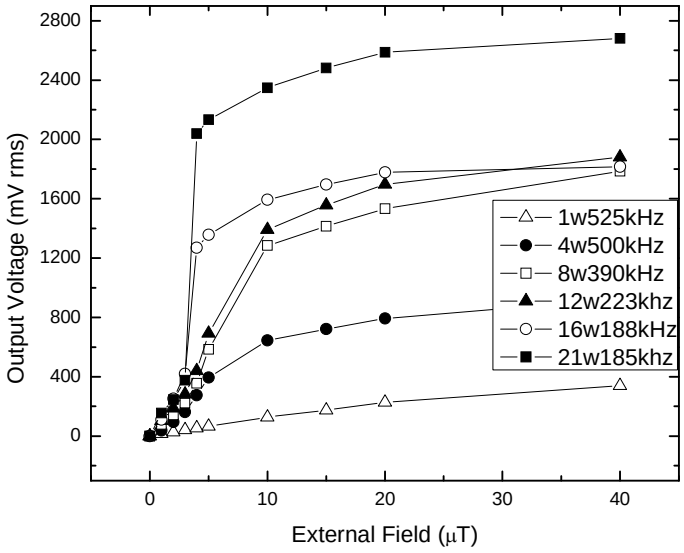

(a)

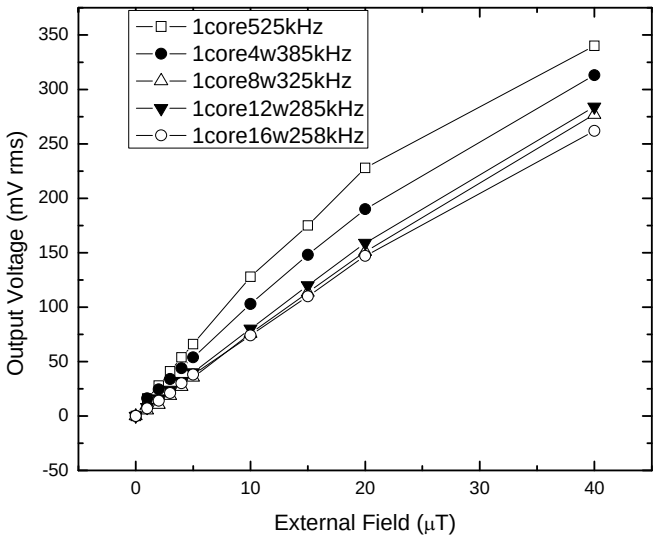

(b)

Fig. 5.29 (a) Sensing output for sensing element with the number of cores of 1, 4, 8, 16, 21, respectively, showing obvious sensitivity resonance in sensing element with 16 cores or 21 cores; (b) sensing output for sensing elements with the number of cores of 1, 5, 9, 13, 17, respectively, each with only one core having excitation current passing through.

It should be noted that the magnetic interaction between the closely packed ferromagnetic cores, which should have caused the exponential increase and resonance in the sensor sensitivity as observed, was on the condition that each ferromagnetic core was magnetized by a high frequency field induced by the high frequency excitation current passing through the core. This condition was confirmed by the results as shown in Fig. 5.29 (b), in which the sensing elements were closely packed with the number of cores of 1, 5, 9, 13, 17, respectively, each with only one core having excitation current passing through. Compared to the case of one-core sensing element, the sensing output in the cases with multi-core sensing element was slightly lower, and the larger the number of cores, the lower the sensing output.

Based on the findings that the magnetic interaction between the ferromagnetic cores relate to the high frequency excitation current passing through the cores, to further investigate the interaction effect, for the sensors having sensing elements packed with 16 ferromagnetic cores, the sensing output was measured against the frequency of excitation current to see the relationship between the sensing element sensitivity resonant frequency and the external field intensity. Fig. 5.30 shows that the resonant frequency varied with the external field. The resonant frequency increased against the external field.

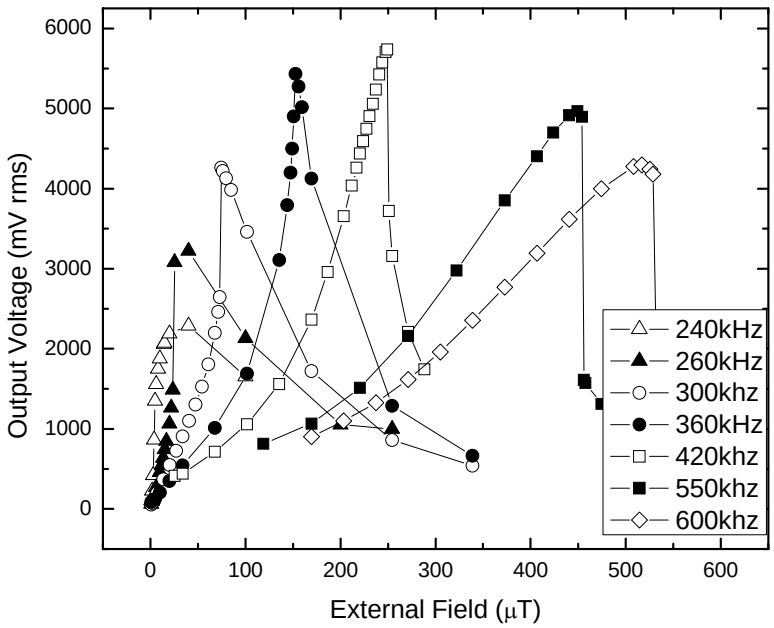

Fig. 5.30 Sensing output and sensitivity resonance vary with the frequency of excitation current passing through the 16 cores of sensing element. The resonant frequency increased against the external field.

5.4 Noise characterization of multi-core fluxgate

5.4.1 Multi-core orthogonal fluxgate with GCAWs

An example of the measured sensitivity curves is shown in Fig. 5.31: two wires (T1A and T1B were used individually (single-wire cores) or closely together, either in serial or antiserial connection. The results show that the sensitivities for double cores are more than twice the sensitivity of single-wire sensors. One explanation of this fact can be the increase of the quality of the tuning circuit due to larger cross-section of inserted ferromagnetic material. However, this mechanism is still under study. The frequency characteristics of the sensitivity show that with the exception of highest

frequencies the sensitivity of serially and antiserially connected cores is same. The important advantage of antiserial connection is that the amplitude of spurious voltage at the excitation frequency is lower and thus the signal processing is much easier.

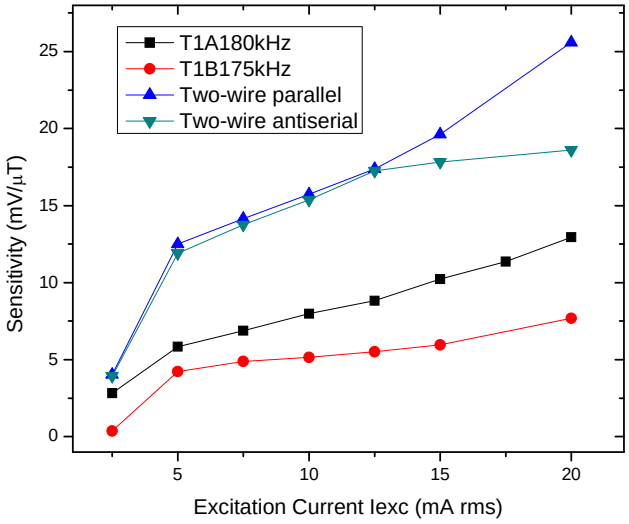

Fig. 5.31 Sensitivity using T1A and T1B as cores for tuned fluxgate sensor: single-wire versus two-wire.

The lowest noise of 0.34 nT/√Hz@1Hz (1.2 nT rms in 30 mHz to 10 Hz range) was achieved for core made of antiserially connected wires with dipolar interaction (Fig. 5.32). The noise in the time domain and short-term (10-minute) offset stability at constant temperature are shown in Fig. 5.33. Distance between the wires was approximately 100 μm and excitation current was 20 mArms. With the excitation current reduced to 10 mA the noise increased to 0.52T nT/√Hz@1Hz. These are values competitive to AMR sensors.

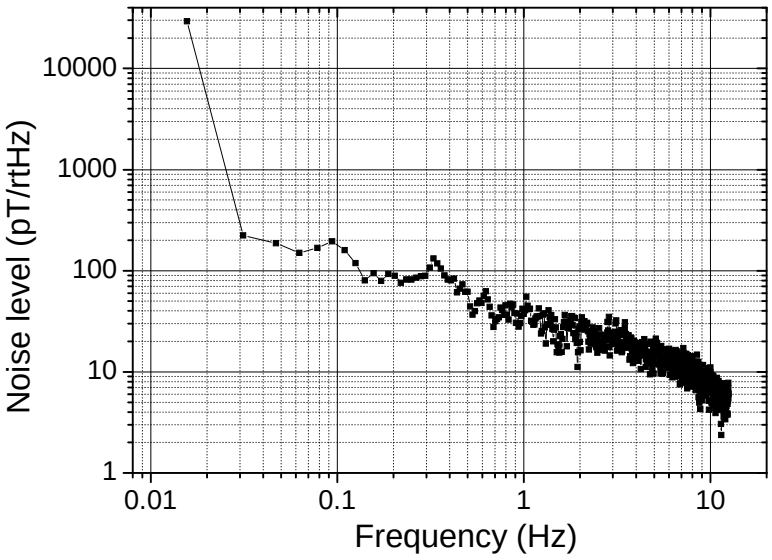

Fig. 5.32 Noise of two-wire core with dipolar interaction excited antiserially.

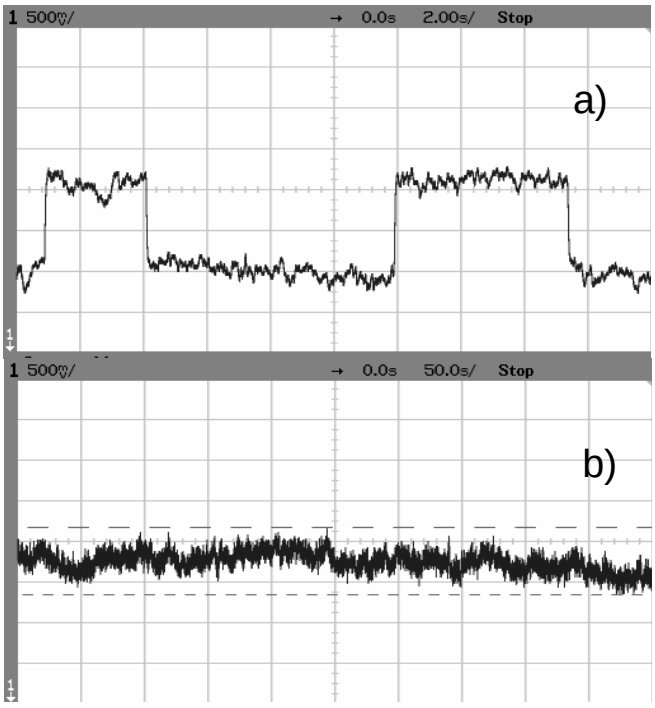

Fig. 5.33 Noise of the same sensor in the time domain:
a) response to 10 nT field step, b) 10-minute stability (same y scale 5 nT/div)

5.4.2 Multi-core orthogonal fluxgate with CWs

Fig. 5.34 (a) compares the sensitivity of the orthogonal fluxgate sensors with micro-wire arrays based on CWs in different number of wires working in both fundamental mode and second harmonic mode. It is shown that in the two working modes the sensitivity increased non-linearly with the increase of the number of wires. This is similar to the results reported previously [139] in which the glass covered amorphous wires were used as the multi-core sensing element in orthogonal fluxgate sensors.

It is noticed that the sensitivity of the second harmonic is always larger than that of the fundamental mode, which is different from the results in [53] and [58]. This is the consequence of the different materials and dimensions used for the sensing element.

Regarding the noise level of the micro-wire arrays, it can be seen from Fig. 5.34 (b) that the 5-wire array structure had the lowest noise level in both fundamental mode and second harmonic mode. This can be explained by the large collective compactedness value of the 5-wire array structure, which is relatively more compact and uniform with most wires packed close to each other. The noise spectrum density at 1 Hz has been reached as low as 42 pT/rtHz in the fundamental mode and 177 pT/rtHz in the second harmonic mode. The Magnetic field noise spectral density of the 5-wire array in both working modes was shown in Fig. 5.35. For the same sensing element, the noise level was suppressed four times lower using fundamental mode compared to the second harmonic mode.

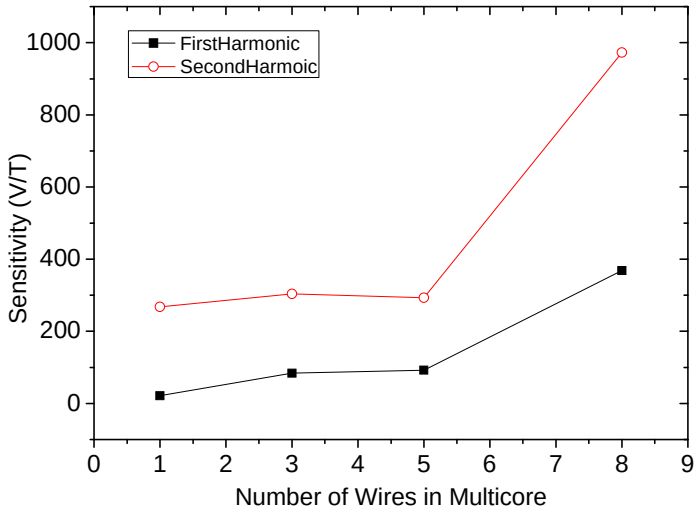

(a)

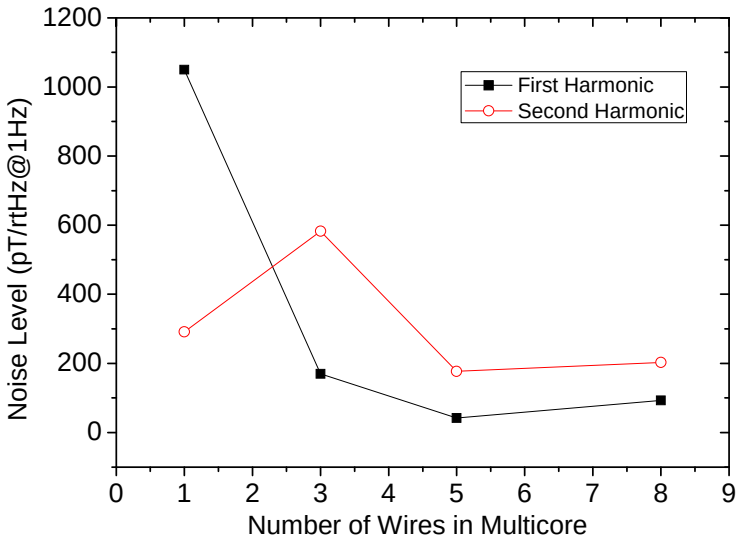

(b)

Fig. 5.34 (a) Sensitivity and (b) Noise level of the multi-core sensing elements working in fundamental mode and second harmonic mode.

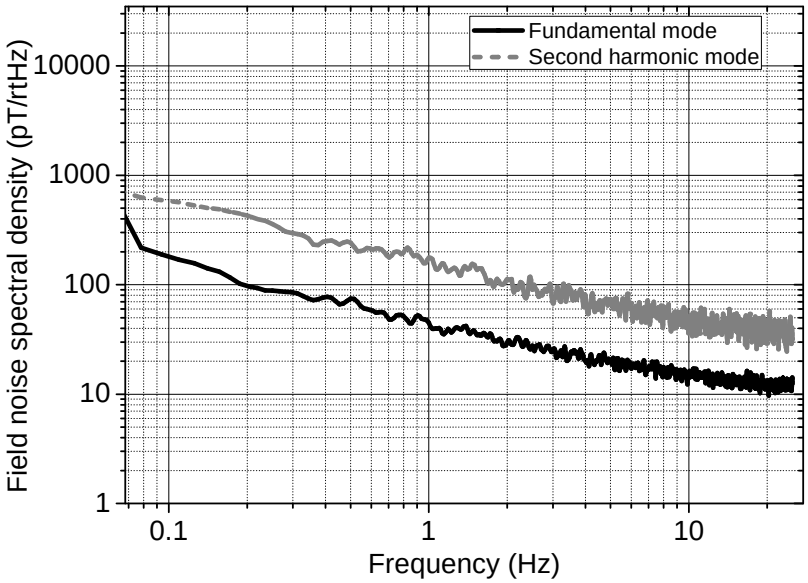

Fig. 5.35 Magnetic field noise spectral density of the 5-wire array working in fundamental mode and second harmonic mode.

5.5 Interaction in Multi-core FeCoSiB GCAWs

5.5.1 Volume Increase of the Sensing Element

Two tests were conducted to investigate how the volume of ferromagnetic material in the sensing element formed by one core would contribute to the sensing output in comparison with increasing the number of ferromagnetic cores. The first test compared one core of diameter 23 μm against two cores of diameter 16 μm. The second test compared one core of diameter 30 μm against three cores of diameter 16 μm. In each case the cross-sectional areas of the sensing element were kept almost equal (128π μm^2 vs 132π μm^2 in the two-core case vs one-core case, and 192π μm^2 vs 225π μm^2 in the three-core case vs one-core case).

The magnetic properties of the core wires in the 3 diameters were also measured and compared by hysteresis loops, as seen in Fig. 5.36. The larger diameter wire had lower coercivity values-higher permeability.

The results are shown in Fig. 5.36 and Fig. 5.37. In Fig. 5.36, comparison between sensing outputs from two-core sensing element and from one-core is shown. In sensing the weak field up to 10 μT (see Fig. 5.36 (a)), the two-core sensor showed the sensitivity of 120 mV/μT against 60 mV/μT in one-core sensor, which is 100% higher. Another difference was that the saturation field of the two-core sensor was larger than that of one-core sensor (see Fig. 5.36 (b)). The results in Fig. 5.37 for three-core against one-core showed similar features and trends as those observed from the case of two-core against one-core. These results indicated that the increase of sensor sensitivity by the multi-core sensing element was unlikely due to the increase in the volume of the ferromagnetic material in the sensing element.

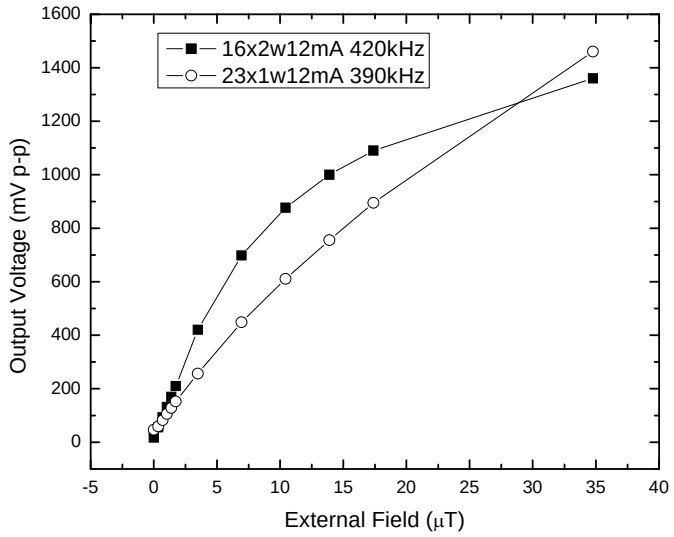

(a)

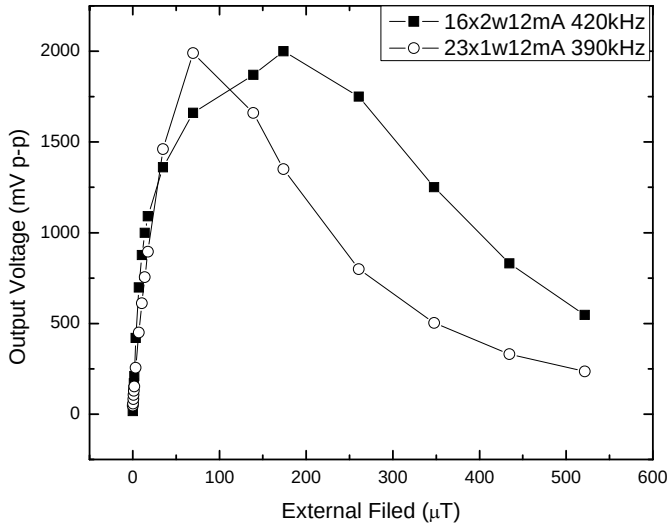

(b)

Fig. 5.36 Comparison between sensor outputs from two-core and one-core sensing elements in sensing external field (a) from 0 to 40 μT, and (b) from 0 to 600 μT. (The excitation current densities were the same for two-core and one-core sensing elements, but the frequencies were different. For each case, the optimum frequency that makes the highest sensitivity was used).

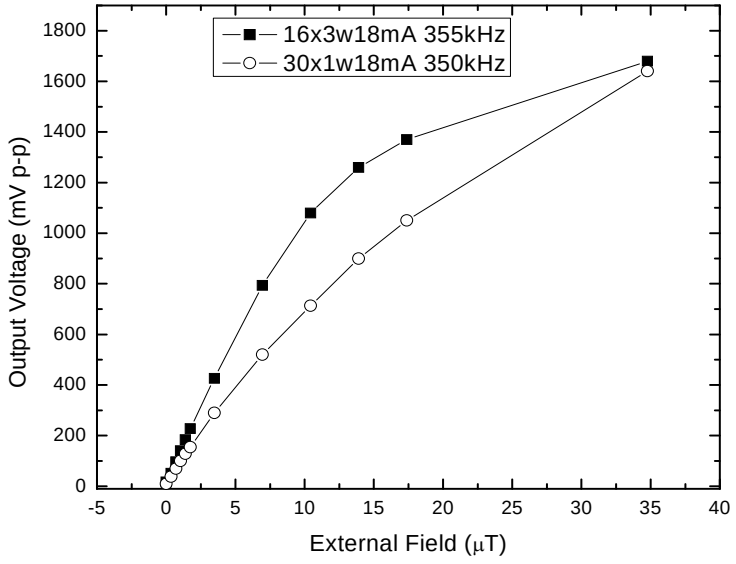

(a)

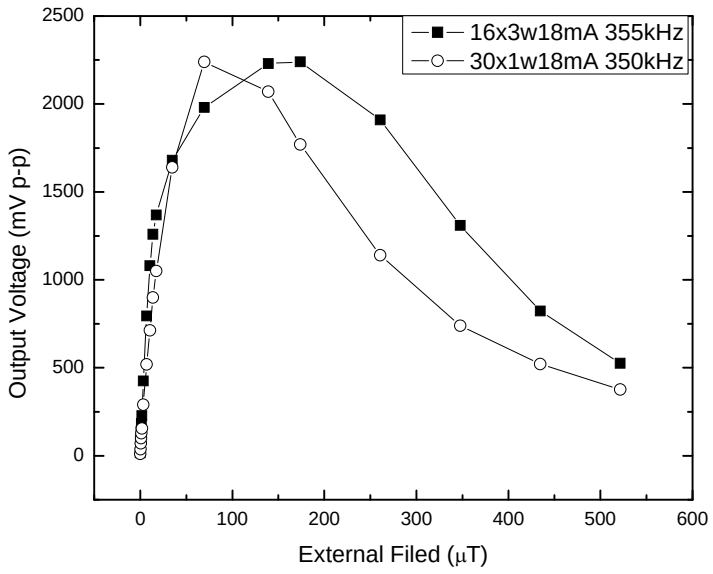

(b)

Fig. 5.37 Comparison between sensor outputs from three-core and one-core sensing elements in sensing external field (a) from 0 to 40 μT; (b) from 0 to 600 μT. (The excitation current densities were the same for three-core and one-core sensing elements, but the frequencies were different. For each case, the optimum frequency that makes the highest sensitivity was used).

5.5.2 Increase in the Current flow in the sensing element

Considered that the AC current passing through each core may generate an AC circumferential filed that magnetizes other cores directly and such fields from all the cores may partially be cancelled out by each other and partially be enhanced by each other, the total effect of having multiple currents on the sensing output was investigated experimentally by forming the sensing element with four copper wires of diameter 70 μm in parallel to and together with a glass-coated amorphous wire of diameter 23 μm. The test results for the sensing output with and without current passing through the copper wires are shown in Fig. 5.38. From Fig. 5.38 (a) it can be

seen that when a low voltage was applied, the sensing output for the case with current passing through the copper wires was actually smaller compared to the one without current passing through the copper wires, indicating a negative effect of the current passing through the copper wires. When the voltage applied was high enough shown in Fig. 5.38 (b), with and without current passing through the copper wires, the sensing outputs were about the same.

These results indicated that increase in the current flows in the sensing element would not cause the increase of the sensitivity of the multi-core sensor as observed.

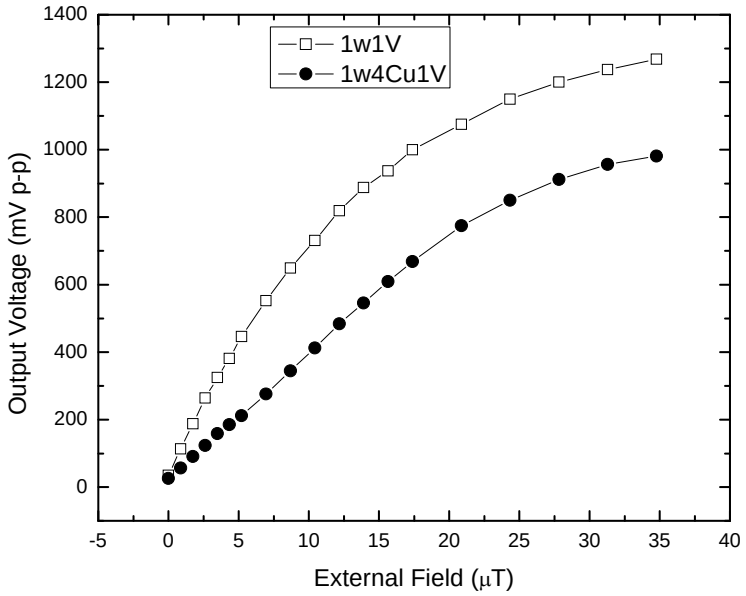

(a)

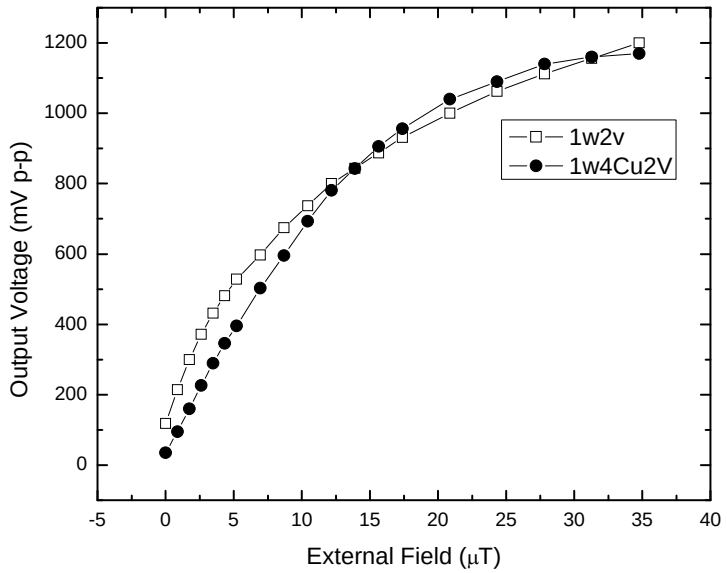

(b)

Fig. 5.38 Sensing output for sensing element with and without currents passing through four cooper wire cores parallel to and together with a glass-coated amorphous wire core; (a) when applied voltage was 1 V, (b) when applied voltage was 2 V.

5.5.3 Interaction between the ferromagnetic cores under ac excitation field

To check if magnetic interaction between the ferromagnetic cores in the sensing element was the main cause of the exponential increase of sensitivity of the multi-core sensor, considered the fact that the intensity of magnetic interaction between two bodies is inversely proportional to distance between the two bodies, the sensor sensitivity in relation to the distance between the cores in the sensing element was tested. Fig. 5.39 shows the results for a two-core sensing element case, in which the left side core and right side core were having a distance of 5 times of their diameter. The curves L and R show the sensing output for the left side core and the right side

core, respectively, each core alone having the excitation current passing through. The curve LR shows the sensing output for both cores having the excitation current passing through. The curve LaddR shows a summation of the sensing output for the excitation current passing through the left core only and that for the right core only. It can be seen that taking into consideration of experimental measurement errors, curves LR and LaddR are about the equal. This means that when the distance between the two cores is large, such as 5 times of their diameter, the increase in the sensor sensitivity is a linear summation rather than the exponential increase as shown in Figs. 2 and 3, in which the multiple cores were packed next to each other.

This result indicated that the exponential increase in the sensor sensitivity with increasing the number of cores in the multi-core sensor was due to magnetic interactions between the closely packed ferromagnetic cores under the influence of high frequency excitation current.

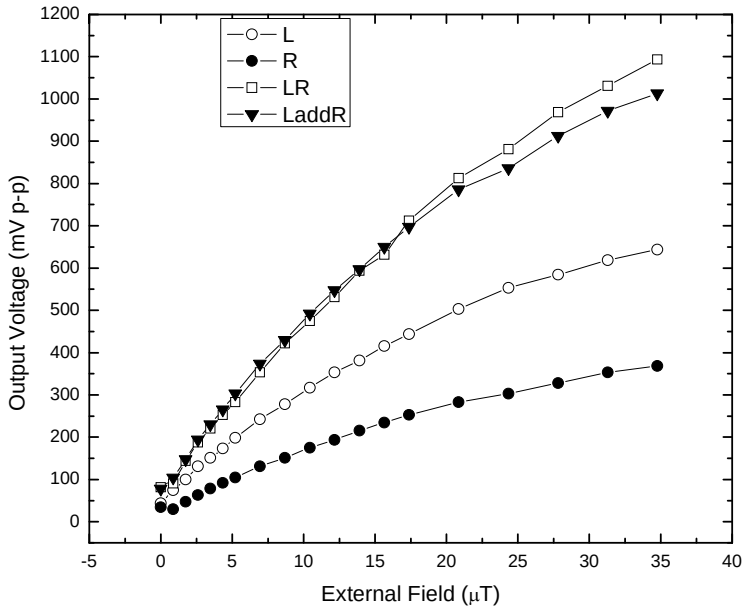

Fig. 5.39 Sensing output for a two-core sensing element having a distance of 5 times of their diameter between the two cores.

5.6 Summary

A new design of multi-core orthogonal fluxgate sensor has been studied experimentally, in which the sensing element is the multiple ferromagnetic micro-wires forming arrays. Firstly the characteristics of the orthogonal fluxgate effect have been investigated using single GCAW and CW in regarding to the parameters that influence the sensitivity and noise. 1) Orthogonal fluxgate responses in both fundamental mode and 2^{nd} harmonic mode have been measured and compared using multi-core sensing element. The traditional 2^{nd} harmonic mode has higher sensitivity while the fundamental mode has lower noise level. However, the power consumption of the fundamental mode is higher since it needs additional bias dc for excitation. 2) The sensitivity can be enhanced by tuning effect using adjusting capacitor or self-capacitance of the pickup coil. However, caution should be noted that circuit may be unstable by too much tuning. 3) Excitation current plays an essential role in the orthogonal fluxgate. The sensitivity increases with the increase of the amplitude of the excitation current and after an optimum value it will decrease gradually. Also, the optimum excitation frequency is dependent on the amplitude of the current with a local maximum at 15 mArms for CWs. The perming error, caused by the remanent field in the sensing element has been found suppressed by large excitation current. 4) The parameters of the pickup coil have been studied and it can be concluded that for the number of turns, though theoretically the sensitivity is proportional to it, the larger number of turns, the larger self-capacitance which lowers the optimum frequency and thus deteriorates the sensitivity. The optimum number of turns found experimentally is 1000 for the micro-wire sensor. For other geometries, the sensitivity can be

enhanced by the pickup coil with reduced diameter of the coil wire, shortened coil length, and smaller diameter of the coil tube. All these characterization provide a solid basis for the multi-core orthogonal fluxgate design and development.

The sensitivity and noise of the multi-core orthogonal fluxgate have been investigated based on GCAW and CW arrays with different number of wires and different structures. Results showed that the sensitivity of the multi-core orthogonal fluxgate sensor is much higher than the conventional single-core orthogonal fluxgate sensors, and the sensitivity increases exponentially with the increase of the number of wire in the arrays. Limited by the experimental conditions, the highest number of wire for GCAWs is 21 and for CWs is 8. The highest sensitivity recorded is 1663 mV/μT found in GCAW array with 21 wires. In the noise measurement it is found that the noise level is did not increase with the increase of the number of wires in the sensing element. It depends on the array structure of the wires and the working mode. The noise level has been found lower in the fundamental mode compared to that in the second harmonic mode. In both fundamental mode and second harmonic mode, a minimum noise density has been found in a 5-wire array which was the optimum structure in this study.

To understand the mechanism of the multi-core effect on the sensitivity and noise, experiments have been designed and conducted to investigate the interaction between wires in the array. The results showed that the sensing output increases with increasing the number of cores exponentially only if the multiple cores in the sensing element are close enough to each other and have high frequency current passing through them. Such sensitivity increase was neither due to solely increase in the

excitation current through cores, nor due to the increase of the volume of ferromagnetic material in the sensing element. The results further showed that there was a sensitivity resonance of the sensing element, with the resonant frequency varied with external magnetic field. All the results pointed to a conclusion that there was a dynamic magnetic interaction between the ferromagnetic micro-wires in multi-core orthogonal fluxgate, which makes the sensing output increase exponentially with the number of wires.

Chapter 6
Multi-core Orthogonal Fluxgate Modeling

6.1 Introduction

This chapter presents the theoretical studies on the multi-core orthogonal fluxgate effect based on the structured micro-wire arrays. It has been shown in the Section 2.3 that the conventional models of the orthogonal fluxgate effect are established on the simplified magnetic properties of the sensing element, using either isotropic approximation or single domain structure. In this project, modeling of the sensing element is taking account of several key parameters of the novel multi-core structures, the number of wires, the anisotropy, the susceptibility tensor, as well as dipolar interaction between wires. Analytical models of the sensitivity and noise are also proposed for the multi-core orthogonal fluxgate sensor as shown in Fig. 6.1 in order to combine the suitable readout methods with the field response mechanisms and to optimize the performance of the sensor.

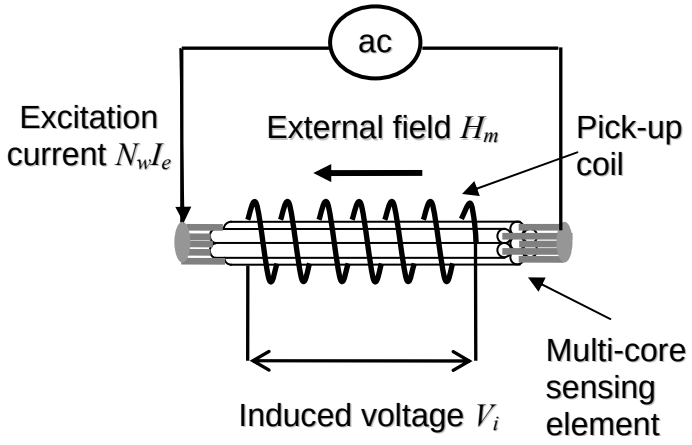

Fig. 6.1 Multi-core orthogonal fluxgate setup

6.2 Magnetization Process of the Multi-core Structure

For the multi-core structure in forms of micro-wire arrays, both the magnetization process in the individual wires and the interaction between wires have to be considered. The following two models are proposed to cover these two aspects.

6.2.1 Hysteresis loop model

For GCAWs, the well-known "core-shell" domain structure results in the dominant circumferential anisotropy in the wire. Based on the magnetization rotation model introduced in section 2.3.4, a simple and effective model of axial hysteresis loop of GCAWs can be shown as in the Fig. 6.2 (a). Since the coercivity of the GCAWs is very small, the axis loop can also be considered linear within +/- H_k. Fig. 6.2 (b) shows the circular hysteresis loop model where the shape is similar to that of axial model but the squareness ratio and circular coercivity $H_{c\theta}$ are larger. Due to the tensor nature of the susceptibility, an axial-circular loop can also be modeled as shown in Fig. 6.2 (c). In the axial-circular loop M_zH_θ, an external field H_m in the axial direction has to be applied, and the axial component of the magnetization is $\chi_i H_m$, where χ_i is the initial susceptibility of the wire. $\chi_i H_m$ in axial-circular loop can be regarded as the counterpart of the remanent magnetization in the axial loop. Corresponding to the increasing trend of magnetization in axial loop, in axial-circular loop, the magnetization M_z should be decreasing with the circumferential field H_θ due to the magnetization rotation. When the circumferential field reaches H_k, the M_z should be zero.

$$M_z = \chi_i H_m \pm \frac{\chi_i H_m}{H_k} H_\theta \tag{6.1}$$

Once taking into account of coercivity, the axial-circular loop will become the one with dot line shown in Fig. 6.2 (c). This model agrees well with the gating curves measured in section 5.2.1.

These three hysteresis loops can also be used in materials with helical anisotropy, such as CWs, with only modification of the values of H_c and $H_{c\theta}$. For CWs, the domain structures have been studied by Kerr effect magneto-optical method and the results showed that in the surface of the CWs there are circular domains forming "bamboo" like structure. However, it was found that the domain structure which closely related to the anisotropy of the wires depends greatly on the fabrication process of the wires. That is, the conditions where the CW were deposited, especially the external magnetic field which may alter the direction of the anisotropy. Normally, the external field is non zero and the anisotropy is helical and occasionally, the external field is zero and the anisotropy is circular. Most CW samples have been electroplated in water bath without magnetic shielding and the helical anisotropy has always been observed.

Note that the difference between the hysteresis models and the one in section 2.3.4 is that no single domain assumption is needed in these hysteresis models, since these models are based on the anisotropy and domain structure of the micro-wires.

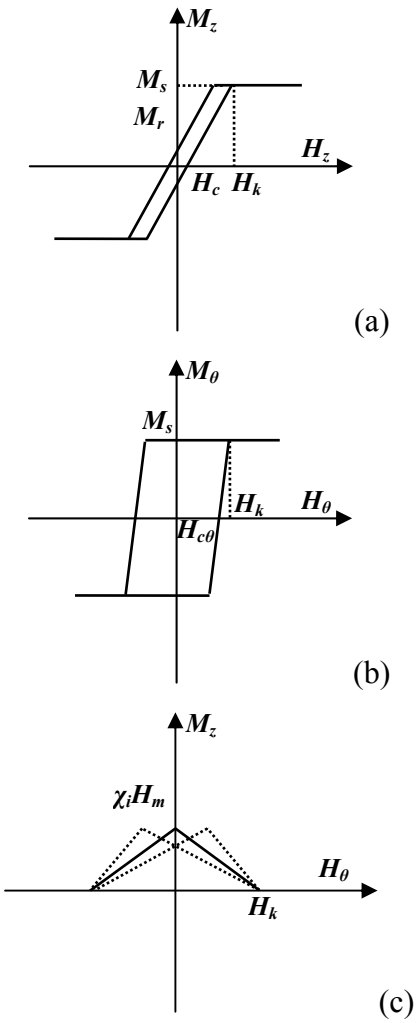

Fig. 6.2 Hystersis loop model for GCAWs and CWs, (a) axial loop M_zH_z; (b) circular loop $M_\theta H_\theta$ and (c) axial-circular loop M_zH_θ.

6.2.2 Dipolar interaction model

Consider the structure of the micro-wire arrays shown in Fig. 4.13. Since the central part of the wires exhibited adjacent circular domains with alternating left- and right-handed magnetization, there must be longitudinal domains in the wire ends. Therefore, a dipolar field from the end domains of an individual microwire, H_{dipole}, can be

derived in the similar way described in [93],

$$H_{dipole} \propto \frac{m \cdot V}{d^3} \tag{6.2}$$

where ***m*** is the magnetic moment of the end domain treated as a dipole, ***V*** the volume of the domain, and ***d*** the distance between the center of the dipole and the calculated point.

However, completely modeling the structured micro-wire arrays will be an intricate problem, especially for those consisting of NiFe/Cu composite wires which exhibit complicated domain structures. In this section, only the number of wires and the arrangement of the arrays have been considered and the micro-wires in the array are assumed all identical. In this way, a "collective compactedness" factor C_a, of the arrays can be estimated:

$$C_a = \frac{\sum_{i=1}^{N-1} \left(\frac{1}{d_i} \right)^3}{N} \tag{6.3}$$

Where N is the number of the wires in the array and d_i is the distance between wire i and the wire in the center of the array. The collective compactedness takes into account both the effective contiguous volume and the total volume of the array. The larger the collective compactedness value, the more compact the structure, and possibly the larger the interaction effect. Note that this collective compactedness factor is not suitable for the arrays without a "center wire", for example, 2-wires, 3-wire piled up, etc. Table 1 lists the C_a values for the microwire arrays with different number of wires and different structures.

It is shown that the 5-wire array has a largest C_a value whereas the 3-wire array has the smallest C_a value, which means that the 5-wire array is the most closely packed structure and the 3-wire array is the most incompact structure in the tested samples. This result agrees well with the noise level measurement of the arrays used in orthogonal fluxgate as the sensing element, as shown in Fig. 5.34.

The net effect of the compact micro-wire array structure is that it is more uniform and thus tends to profile in a single wire structure. Therefore, it is expected that the micro-wire array with a honeycomb structure as shown in Fig. 6.3 will be the most favorable for interaction (the C_a is 0.86).

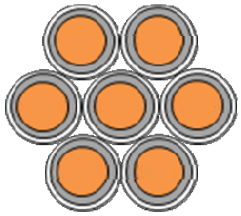

Fig. 6.3 Structure of 7-wire honeycomb

Table 6.1 Collective compactedness value

Array	Collective compactedness, C_a
3-wire	0.667
5-wire	0.8
8-wire	0.673
7-wire honeycomb	0.86

6.3 Skin Effect on Multi-core Structure

Initial susceptibility of a micro-wire array can be enhanced by increasing the number of wires in the array, due to increase of the effective magnetization volume and effect of magnetic domain unification between wires.

6.3.1 Effective magnetization volume

Effective magnetization volume of the material used as magnetic sensing element is the volume of the material that can be fully magnetized by the excitation field. The excitation field is induced by an ac current. At high frequencies, the current density distribution is only in the surface parts of the material due to so called eddy current effect. Therefore, only a small part of the material is useful for the sensing purpose. In case of micro-wires, the volume of this effective part of the material is determined by the skin depth

$$\delta = \sqrt{\frac{2}{\omega\sigma\mu_\theta}} \tag{6.4}$$

where ω is the angular frequency, σ is the conductivity, and μ_θ is the maximum differential circumferential permeability of the wire.

Now we consider a single wire and an N-wire array with same total volume, V. The radiuses of the single wire and each wire in the array are R and $R/\sqrt{N}$, respectively, as shown in Fig. 6.4. With an arbitrary δ (δ < R), the effective volume of the single wire V_1, is

$$V_1 = V - \pi(R-\delta)^2 \tag{6.5}$$

which is always smaller than that of the array, V_N,

$$V_N = V - N\pi(R/\sqrt{N} - \delta)^2 \tag{6.6}$$

With increase of N, the effective magnetization volume of the N-wire array increases as long as the skin depth satisfies

$$\delta < 2R(\sqrt{N+1} - \sqrt{N}) \tag{6.7}$$

Practically N cannot be infinite. The optimum number of wires depends on the skin depth.

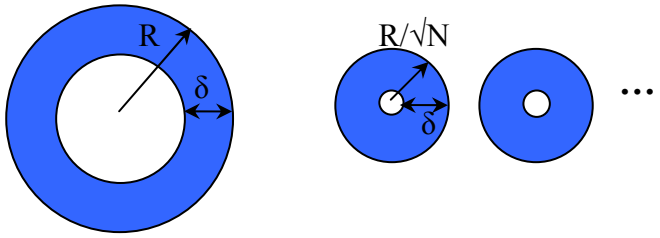

Fig. 6.4 Cross-sections of a single wire and an N-wire array, where the blue areas represent the effective volumes of the wires.

6.3.2 Magnetic domain unification

The magnetic interaction phenomenon is short-ranged, field-induced, and frequency-dependent. Based on this, a domain unification model can be proposed.

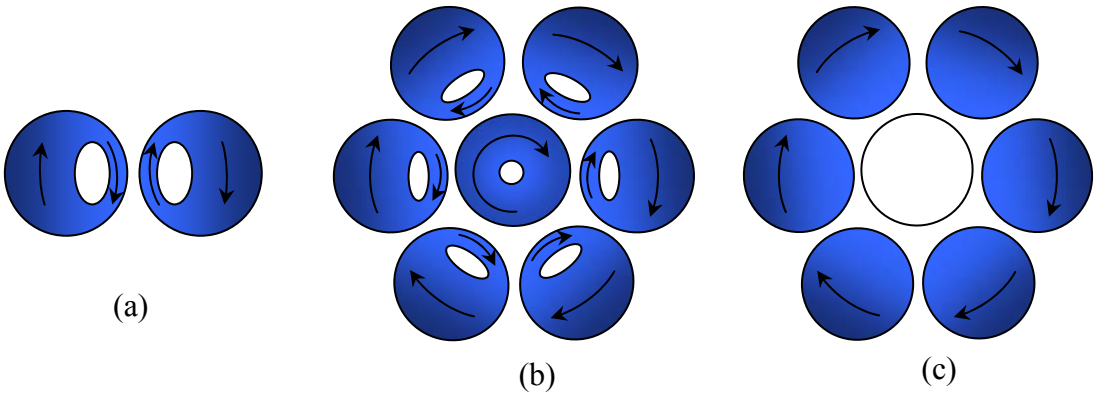

Fig. 6.5 Domain structure of ferromagnetic wire array consists of (a) two wires, (b) multiple wires with sandwich structure, excited at dynamic domain unification frequency and (c) multiple wires with only outer-domain unification, excited at enough high frequency.

Consider circular domain structures in a two-wire system, as shown in Fig. 6.5 (a). Due to the current-induced field by the neighbor wire, the current distribution in the wire will be changed. Simultaneously, the domain structure of the wire will be distorted: the size of outer parts will be enlarged and the inner parts will be reduced. For large number of wires, the domains of neighboring wires would be “unified” and form a effective large circular domain, as shown in Fig. 6.5 (b). The outer-most part of the domains and the middle-part of the domains unify and form a domain coupling in opposite direction. The inner-most part domain is in same direction with the outer-most part, and at the same time form the other domain coupling.

This sandwich structure is advantageous in stability, since the total magnetic energy of the coupling domains is smaller than a single domain. Note that in this structure all of the wires have ac current passing through so that they are all excited. The effective volume will not be reduced. Since large parts of the domains are unified, the total material is more uniformed, and the magnetic properties, such as susceptibility, should be improved.

When the dipole-dipole interaction is considered, the domain structure of the array system will be further distorted by stray fields in the axial direction. The axial component of the magnetization depends on the dipole moment and size of magnetic dipoles.

The sensitivity of unified domain structure is frequency dependent. The optimum sensitivity can be obtained when the dynamic permeability is the optimum. The dynamic permeability is determined by the domain dynamics in the magnetization process, and the size and distribution of domains rely on the skin depth

which is frequency dependent. This model is partially verified by the MI measurement results of GCAWs arrays with different number of wires as shown in section 4.1.4.2, where the frequency of the maximum MI ratio decreases with the number of wires. It can be explained by the inference of domain unification model that the dimension of the interacting domains increases with the number of wires and the corresponding maximum frequency of domain motion decrease with the number of wires.

An extreme case is that when the excitation frequency is too high, the skin depth becomes smaller so that the sandwich domain structure will disappear and only the outer-most part domains will unify, as shown in Fig. 6.5 (c). In this case the effective volume will be greatly reduced and the sensitivity would drop.

6.4 Second Harmonic Sensitivity Model

Based on the modeling of parallel fluxgate effect discussed in section 2.2.3, an analytical model of the 2nd harmonic sensitivity of the orthogonal fluxgate effect can be derived. Consider the multi-core orthogonal fluxgate setup as shown in Fig. 6.1. The excitation current flowing through the micro-wire array is N_wI_e, where $I_e=I_0\sin(\omega t)$, and N_w is the number of wires in the array. The excitation field in each wire produced by the excitation current will be $H_e = H_0\sin(\omega t)$, as shown in Fig. 3.5. In the closely packed micro-wire array, H_e of each wire will be affected by the induced field in neighboring wires and finally frequency dependent. For simplicity, $H_0=I_0/2\pi R$, where R is the radius of the micro-wire. Using the hysteresis loop model developed in section 6.2.1, the axial magnetization

$$M_z = \chi_i H_m \pm \frac{\chi_i H_m}{H_k} \frac{I_0}{2\pi R} \sin(\omega t) \tag{6.8}$$

Thus, the induced voltage in the pickup coil is

$$V_i = -\frac{d\Phi}{dt} = -NN_w A\mu_0 \frac{\chi_i H_m}{H_k} \frac{dH_e(t)}{dt} = -\frac{\mu_0 NN_w A H_m I_0 \chi_i \omega}{2\pi R H_k} \cos(\omega t) \tag{6.9}$$

The real and imaginary parts of the 2nd harmonic V_2 of the V_i are

$$V_2' = \frac{\omega}{\pi} \int_0^T V_i \sin(2\omega t) dt = \beta \int_0^T \cos(\omega t) \sin(2\omega t) dt \tag{6.10a}$$

$$V_2'' = \frac{\omega}{\pi} \int_0^T V_i \cos(2\omega t) dt = \beta \int_0^T \cos(\omega t) \cos(2\omega t) dt \tag{6.10b}$$

$$\beta = -\frac{\mu_0 NN_w A H_m I_0 \omega^2 \chi_i}{2\pi^2 R H_k} \tag{6.11}$$

Assume that $H_0 > H_k$ and the circumferential anisotropy field is H_a. By solving piecewise integration of Eq. 6.10 based on the circular hysteresis model (Fig. 6.2 (b)) and conducting first order Talor series approximation, the amplitude of 2nd harmonic can be obtained

$$|V_2| = \frac{16\mu_0 NN_w A H_a \chi_i H_m f}{H_k} \sqrt{H(H_0, H_k, H_{c\theta})} \tag{6.12}$$

where

$$\begin{aligned} H(H_0, H_k, H_{c\theta}) = & \left(\frac{H_k}{H_0}\right)^2 + \left(\frac{H_k - 2H_{c\theta}}{H_0}\right)^2 - 2\left(\frac{H_k}{H_0}\right)^2 \left(\frac{H_k - 2H_{c\theta}}{H_0}\right)^2 \\ & + 2\left(\frac{H_k}{H_0}\right)\left(\frac{H_k - 2H_{c\theta}}{H_0}\right) \sqrt{1 - \left(\frac{H_k}{H_0}\right)^2} \times \sqrt{1 - \left(\frac{H_k - 2H_{c\theta}}{H_0}\right)^2} \end{aligned} \tag{6.13}$$

The sensitivity of 2nd harmonic is

$$S_2 = \frac{16\mu_0 NAN_w H_a \chi_i f}{H_k} \sqrt{H(H_0, H_k, H_{c\theta})} \tag{6.14}$$

Therefore, theoretically the sensitivity is proportional to the number of wires in the multi-core array. However, as discussed in Chapter 4, magnetic properties of the micro-wire arrays changes as the number of wires increases. Since the circular anisotropy field increases non-linearly with the number of wires, as shown in Fig. 4.8, and the initial susceptibility can also increase non-linearly with the number of wires, the overall trend of sensitivity is non-linear. Using the experimental results for multi-core orthogonal fluxgate based on GCAWs shown in Fig. 4.8 (b) and Fig. 5.26 and assuming the axial saturation field as the circumferential anisotropy field, the relative sensitivity $S(N_w)/S(N_w=1)$ is calculated and plotted against the experimental measured results, as shown in Fig. 6.6.

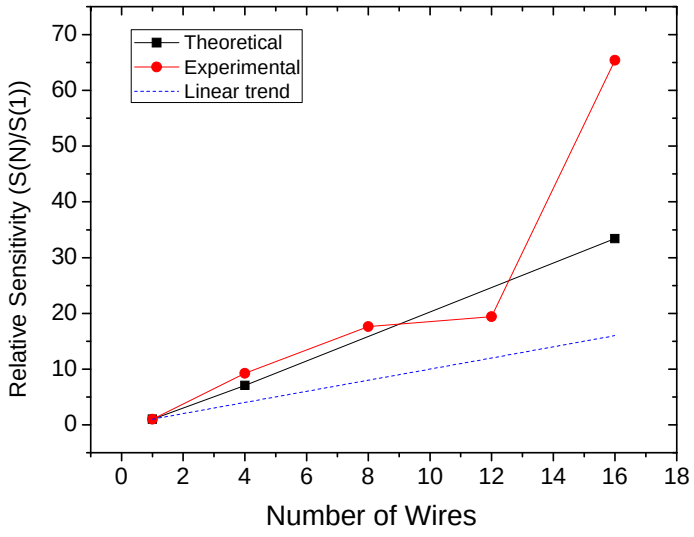

Fig. 6.6 Comparison between experimental and theoretical dependence of the 2nd harmonic sensitivity on the number of wires in the multi-core orthogonal fluxgate (dot line is the linear increasing trend with the number of wires).

The theoretical calculation agrees well with the experiment results when the number of wires is smaller than 10. The discrepancy showing in the larger number of wires may due to the non-linearity of the initial susceptibility, inaccuracy in the estimated values of anisotropy field, and experiment errors occurred in the multi-core sensing element preparation which may deteriorate the uniformity of the sensing core, especially for large number of wires.

6.5 Noise Limit of Multi-core Fluxgate Sensors

A complete noise model for of a fluxgate system should include white noise from the sensing cores and the low frequency 1/*f* noise. In this study only the white noise is considered since the 1/*f* noise is far beyond the project scope. Using the fluctuation dissipation theorem, the equilibrium magnetization noise S_M^{eq} is proportional to the lossy susceptibility of the core χ'' and inversely proportional to the volume of the core Ω [76]

$$S_M^{eq} = \frac{4k_B T \chi''(\omega)}{\Omega \omega} \tag{6.15}$$

where T is the temperature and k_B is the Boltzmann constant. However, the Eq. 6.15 does not apply directly to the fluxgate since the fluxgate core is not in thermal equilibrium. The core is alternately saturated by excitation current. The corrected field noise is

$$S_N = \frac{\mu_0^2 S_M}{\left(dM / dH\right)^2} \tag{6.16}$$

where

$$\frac{dM}{dH} = \frac{dM}{dH_z} \approx \chi_{\max} \tag{6.17}$$

Consider the Eq. 4.3 and the domain-wall dynamics [132], the imaginary part of the permeability complex

$$\mu'' = \frac{(\mu_{dc} - \mu_0)\omega\tau}{1 + \omega^2\tau^2} \tag{6.18}$$

where μ_{dc} is the static permeability and τ is the relaxation time constant representing the delay of the domain-wall displacement with the excitation field in the high frequencies, the field noise becomes

$$S_N = \frac{4\mu_0^2 k_B T}{\Omega\omega}\frac{\chi''}{N_w\chi_{\max}^2} = \frac{4\mu_0^2 k_B T}{\Omega}\frac{(1 + \chi_{\max} - \mu_0)\tau}{N_w\chi_{\max}^2(1 + \omega^2\tau^2)} \tag{6.19}$$

where N_w is the number of wires in the multi-core, Ω is the volume of each micro-wire. Since χ_{max} >>1, by Eq. 4.3,

$$S_N = \frac{4\mu_0^2 k_B T}{\Omega M_s}\frac{\tau}{N_w\chi_{\mathrm{m}}(1 + \omega^2\tau^2)} \le \frac{2\mu_0^2 k_B T}{\Omega M_s}\frac{1}{N_w\chi_{\mathrm{m}}\omega} \tag{6.20}$$

Therefore, for multi-core orthogonal fluxgate sensors, the white noise level is inversely proportional to the number of wires, maximum susceptibility and measuring frequency. Using experimental data, the white noise of multi-core orthogonal fluxgate based on GCAW arrays consisting of 1, 4, 16 wires and NiFe/Cu CW arrays consisting of 1, 3, 5, 8 wires is plotted in Fig. 6.6 (a) and (b), respectively. Note that for GCAW arrays, the white noise is very small (in fT level) and for CW arrays the

white noise is in pT level. This difference is mainly due to the large difference in the wire volume, for CWs, only the volume of the permalloy layer was calculated so that the noise is much higher than GCAWs. Both trends of the two micro-wire arrays are decreasing with the number of wires, which can be explained by the large impact of the total volume.

Compared with the experimental results in Fig. 5.34 (b), the general trends reasonably agree. The theoretical values are much smaller than experimental data due to the simplicity of the model and many possible noise sources in the measurement. Nevertheless, the white noise model provides the fundamental limits to the multi-core orthogonal fluxgate sensors based on the micro-wire arrays.

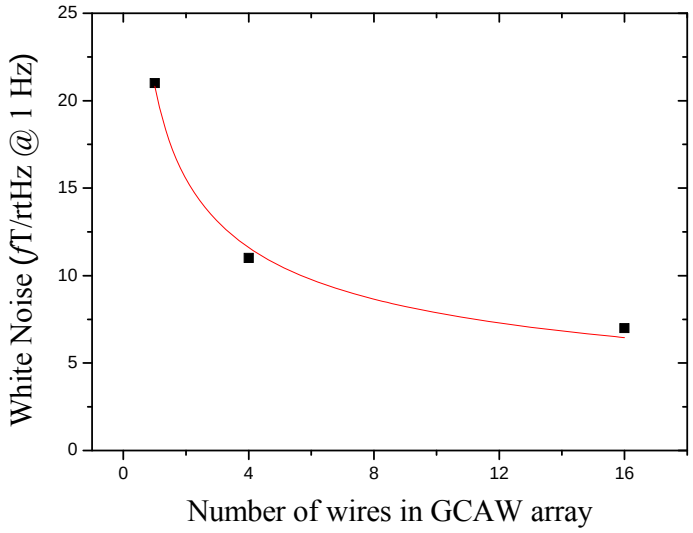

(a)

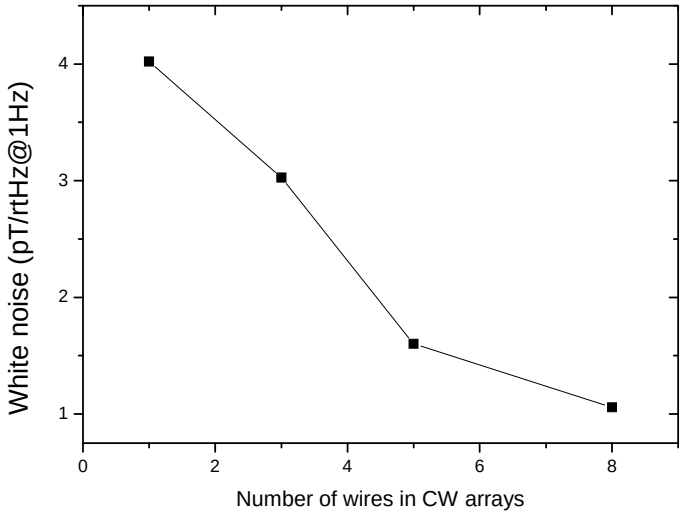

(b)

Fig. 6.7 Calculated white noise level of multi-core orthogonal fluxgate sensors based on (a) CoFeSiB GCAWs and (b) NiFe/Cu CWs.

6.6 Summary

The magnetization process of the micro-wire arrays with GCAWs and CWs has been modeled by three hysteresis loops. In orthogonal fluxgate the micro-wire arrays present a complicated magnetization process due to the operation mode that the excitation field is in circumferential direction and the sensing field is in the axial direction. Fitting with this application, micro-wire arrays present large orthogonal fluxgate responses resulting from their anisotropy and domain structures. GCAWs have a circumferential anisotropy with a small angle to axial direction due to the core-shell domain structure. CWs present helical anisotropy with easy axis inclined to circular direction. Correspondingly axial loop has been modeled with small coercivity

and small susceptibility and circular loop has been modeled with large coercivity and large susceptibility. The axial-circular loop is based on the measured gating curves and has been simplified to linear dependence of the axial magnetization on the circular field.

A dipolar interaction model taking into account of the compactedness of the micro-wire arrays has been developed. A collective compactedness value derived from the ratio of effective contiguous volume to the total material volume can be used to describe the degree of the interaction effect in some certain micro-wire arrays with small number of wires and compact structure. The model has been verified by experimental results on the noise level of arrays with different number of CWs. According to this model the 7-wire honeycomb structure is most favourable array structure which has become the design guide of the multi-core sensing element.

In the high frequency domain, the skin effect plays a key role in the magnetization of multi-core structures. The effective magnetization volume of multiple wires with small diameter has been calculated and compared with that of single wire with equal total volume. It is found that the largest number of wires depends on the skin depth, which is frequency dependent. Assuming micro-wires with different diameters have same magnetic properties, the increase of the number of wires results in linear increase of the sensitivity.

On the other hand, non-linear increase of the sensitivity may arise when a domain unification effect occurs, in which magnetic domains in neighboring wires “unifies” into a large effective domain and the maximum domain motion frequency

will decrease. The decreasing trend of frequency with the number of wires is in good agreement with that of the frequency of the maximum MI ratio in variation with the increase of the number of wires measured in GCAW arrays. Moreover, the domain unification model predicts the improvement of the magnetic properties of the micro-wire array with sandwich structure, which agrees with the outcome of the dipolar interaction model.

Based on the experimental measurement results and hypothesized models of the micro-wire arrays, an analytical model of the 2^{nd} harmonic sensitivity of the multi-core orthogonal fluxgate has been established. Expressions of the 2^{nd} harmonic output and the sensitivity derived by Fourier analysis show that the number of wires, anisotropy field, initial susceptibility and frequency are the key parameters determining the sensitivity. The theoretical results agree well with the measured data from GCAW arrays with the number of wires less than ten. For larger number of wires, discrepancy occurs and can be reasonably explained by the simplicity of the model and nonuniform arrangement of the arrays with large number of wires.

The last part of the theoretical work is the model of the white noise of the multi-core sensing element in the form of micro-wire arrays. Based on a corrected magnetization equilibrium model, the local maximum noise expression has been derived through domain-wall dynamics. Theoretically the noise level is inversely proportional to the number of wires, maximum susceptibility, and working frequency. The model provides the fundamental white noise level to the multi-core orthogonal fluxgate. The theoretical noise of GCAWs is tens of femtotesla which is far below the

experimental results while the noise of CWs is less than 4 picotesla which is more close to the experimental results.

Chapter 7
Multi-core Orthogonal Fluxgate Magnetometers

Based on the multi-core sensing elements in form of ferromagnetic micro-wire arrays, orthogonal fluxgate magnetometers with optimum parameters have been designed, fabricated, and tested. The major objective performances are sensitivity and noise, as well as the size, power consumption, and thermal stability. In this chapter, the details of the design and fabrication of the readout circuit and sensor head of the magnetometer are presented in section 7.1. The performance testing results in sensitivity and thermal stability are presented in section 7.2. Finally, comparison of main performance between our multi-core orthogonal fluxgate (MOFG) prototype and commercial off-the-shelf (COTS) magnetometers is summarized.

7.1 Design and Fabrication of MOFG

7.1.1 Magnetic Feedback Circuit

The block diagram of the magnetometer working on feedback second harmonic mode is shown in Fig.7.1. The magnetic feedback circuit consists of three circuit modules: excitation circuit, readout channel (forward loop), and feedback loop. The sensor was excited by the excitation circuit that provides a square wave current with frequency f and a $2f$ signal as a reference for the phrase sensitive detector (PSD). Induced voltage signal from the pickup coil in the sensor head is going to the signal readout channel. To obtain sufficient amplification, a pre-amplifier (LT1028) with very low input noise is used before the original signal is denoised by a band pass filter. A PSD is used to

demodulate the high frequency signal to dc or near-zero frequency, since the output signal from the senor is amplitude modulated by the measured field [140-141]. PSD can be realized using analogue switches or multiplexers. The circuit is designed to measure only the second harmonic. By replacing the PSD with a gated integrator, we could also use the higher even harmonics, which may increase the sensitivity and lower the noise [4].

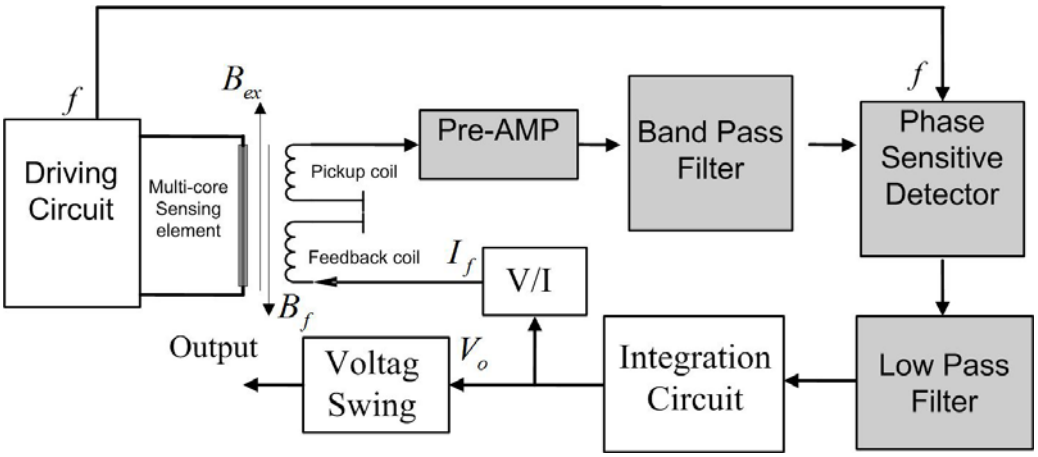

Fig. 7.1 Block diagram of function modules in single axis multi-core orthogonal fluxgate magnetometer

The demodulated signal is filtered and integrated by a feedback loop and snet back to the feedback coil after voltage-current conversion. The purpose to include the feedback loop is to improve the linearity and increase the stability of the sensor. The feedback loop has a large gain by the integration module. The sensor nonlinearity and the nonstability of its sensitivity are suppressed by the feedback gain. Therefore, the magnetometer is working in a closed loop mode.

For 3-axis magnetometers, circuit for three channels can be easily extended from the single channel feedback circuit with few modifications. Limited by the board

size and power consumption, some function modules has been removed (eg. band pass filter). The block graph of the circuit functional modules of 3-axis magnetometer is shown in Fig. 7.2. A complete schematic drawing of the circuit for 3-axis magnetometer is attached in Appendix A. The printed circuit board (PCB) design with dimensions is shown in Fig. 7.6 (a) and the fabricated PCB with all components on the board is shown in Fig. 7.6 (b).

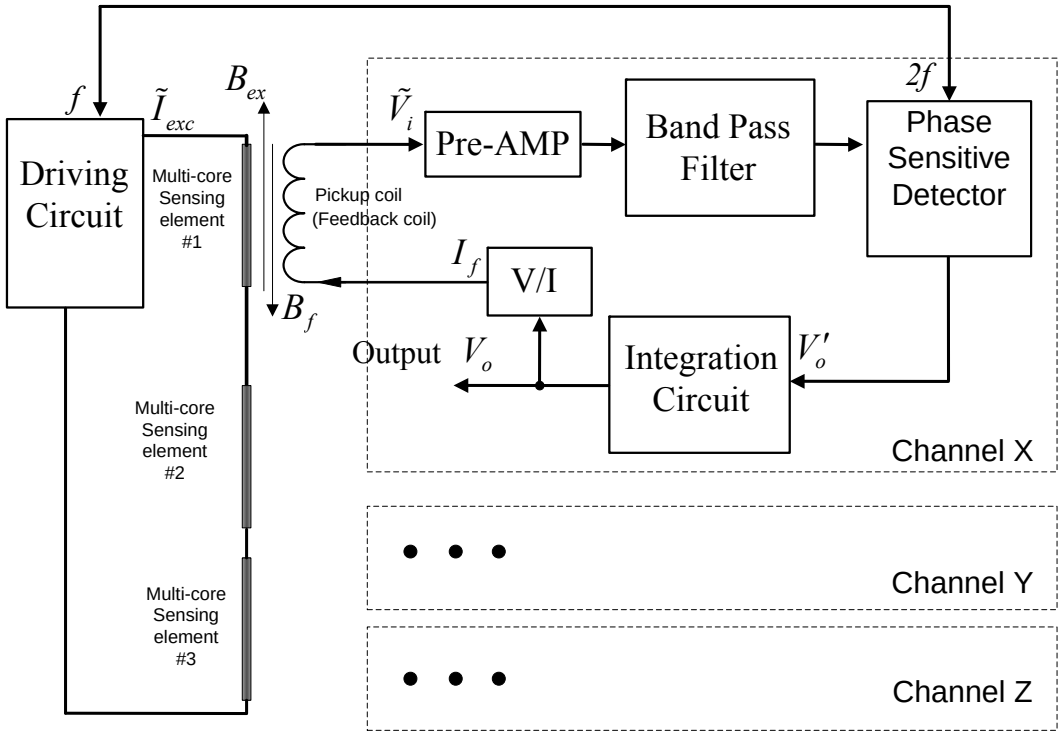

Fig. 7.2 Block diagram of function modules in 3- axis multi-core orthogonal fluxgate magnetometer extended from single axis design

7.1.2 Sensor head and 3-aixs design

In the multi-core sensing element, the multiple sensing wires should be close enough to make magnetic interaction between the wires possible, while not touching each

other. For CWs, two steps must be carried out to construct the composite wires into multi-core structure: firstly, the wires have to be coated with a layer of insulation; secondly, they have to be placed neatly. The insulation coating layer outside the composite wires is used for electrical separation of the neighboring wires in the multi-core structure. Diluted nail polish was gently spread over the newly fabricated composite wires. After a few seconds, a thin layer of insulation would form with a thickness of about tens of nanometers.

Multi-corer sensing elements were fabricated under microscope manually. A planar structure was firstly constructed and fixed and then other wires were added one by one. The first 3 composite wires had to be placed closely side by side to form an inner layer. Two composite wires were placed side by side or on the top of previous 3 wires. Then the whole structure had to be fixed and turned over. The last 2 wires were placed in the same way on the top of the inner layer. Diluted nail polish was used for fixation of the wires to each other. Figure 7.3 shows the fabricated multi-core sensing element with 7 wires in honeycomb structure.

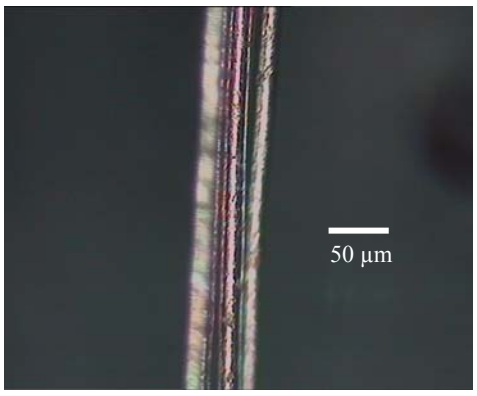

(a)

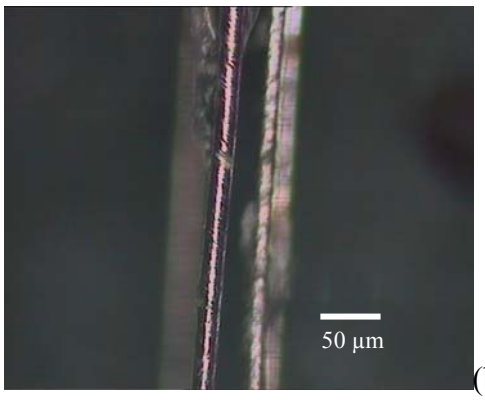

(b)

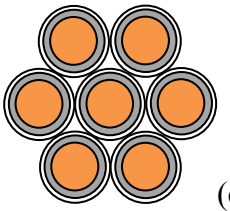

(c)

Fig. 7.3 Fabricated 7-wire honeycomb structure under a microscope (a) and (b). These two photos were taken in different angle. (c) Schematic graph of 7-wire honeycomb structure.

Using 7-wire array as the sensing element, a small sensor head has been fabricated as shown in Fig 7.4. The parameters of the sensor head are presented in Table 7.1. Note that the parameters of the sensor head with micro-wire arrays used for the magnetometer prototype have to be optimized in regarding to the uniformity, arrangement, length to achieve the best performance. The sensor head was using pickup coil as the feedback coil as well. Thus the size can be reduced and the sensor head becomes more compact. Fig. 7.5 shows how these sensor head boards were assembled in the circuit board and the structure of the coordinate system on the board.

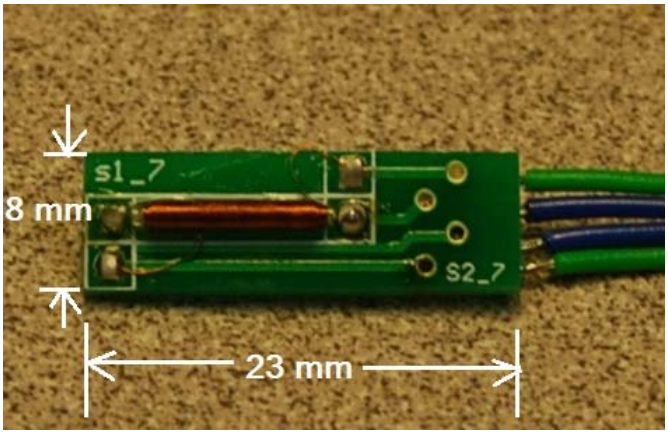

Fig. 7.4 Sensor head board with sensing element, pickup coil and connection wires.

Table 7.1 Parameters of the sensor head

Component	Value
Core length	12 mm
Core cross section	Φ25 μm
Pickup coil length	9 mm
Pickup coil diameter	1 mm
Pickup coil turns	570
Pickup coil wire	Φ80 μm

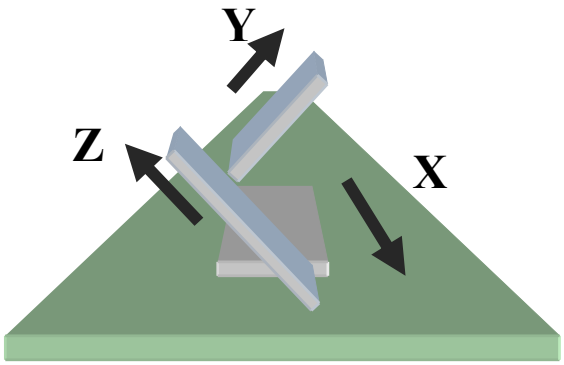

Fig. 7.5 Structure of the sensor head and the coordinate system.

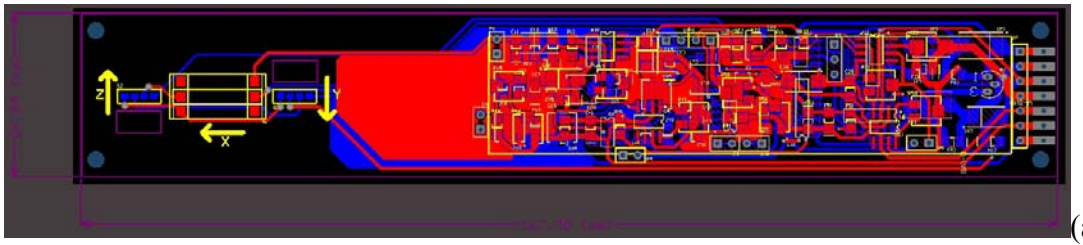
(a)


(b)

Fig. 7.6 Design schematic of the 3-channel readout circuit (a) and photo of the fabricated circuit board (b).

7.2 Performance testing and specifications

7.2.1 Sensitivity and noise

Fig. 7.7 shows the three channel output under the external magnetic field along with the X axis ranging from -50 μT to 50 μT. The system sensitivity is thus 200 mV/μT. Orthogonal voltage outputs of the axes Y and Z are due to the remanent field inside the shielding chamber.

Noise levels of single axis magnetometer and 3-axis magnetometer are shown in Fig. 7.8 and Fig. 7.9, respectively. For single axis magnetometer, the 7-wire GCAWs array with the optimum honeycomb structure was used as the sensing element. The noise level of 8.5 pT/rtHz at 1 Hz has been achieved. For 3-axis magnetometer, limited by the excitation power capability, a 3-wire CW array was used as the sensing element and the noise levels of three channels are within 12 pT/rtHz at 1 Hz. This value is quite close to the theoretical fundamental white noise limit which is 4 pT/rtHz at 1 Hz for single wire and 1 pT/rtHz at 1 Hz for 8-wire array. The 3-axis magnetometer using 7-wire honeycomb arrays as the multi-core sensing element has been proposed and the prototype is in development.

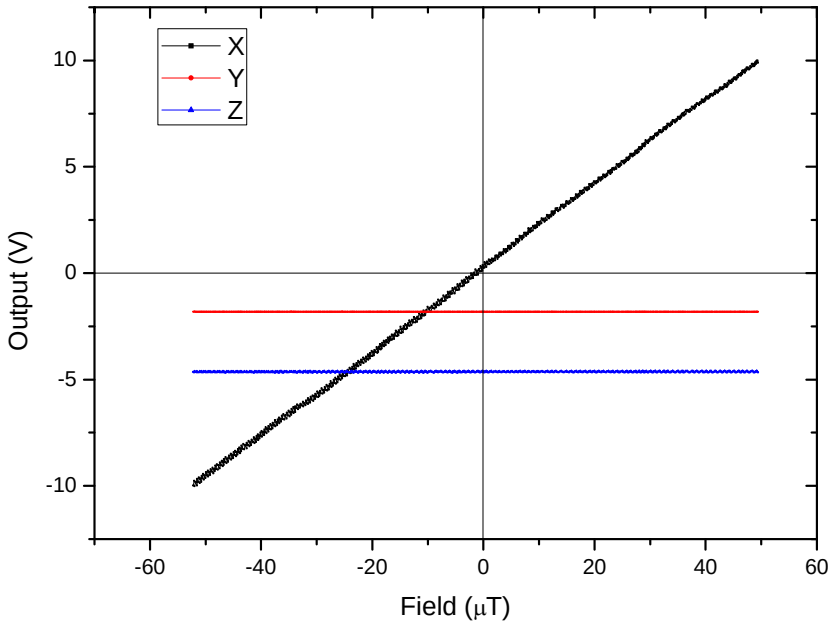

Fig. 7.7 Sensitivity of X channel and calibration of Y and Z channel.

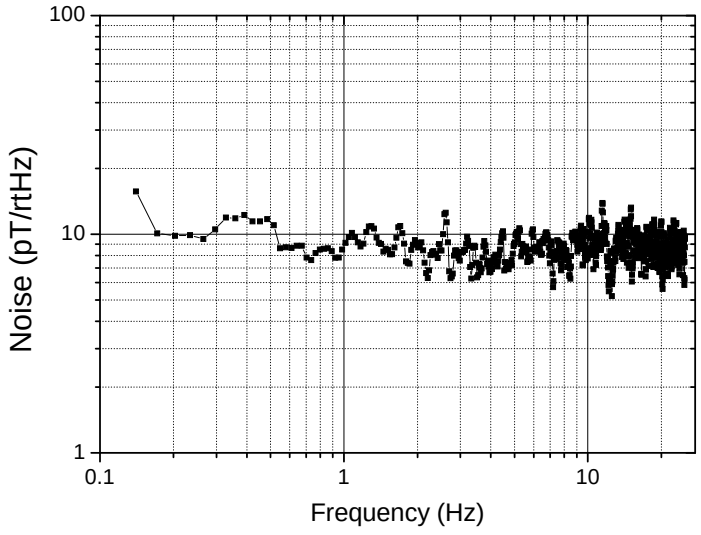

Fig. 7.8 Noise level of the single axis magnetometer using 7-wire honeycomb array based on CoFeSiB GCAWs in the sensing element.

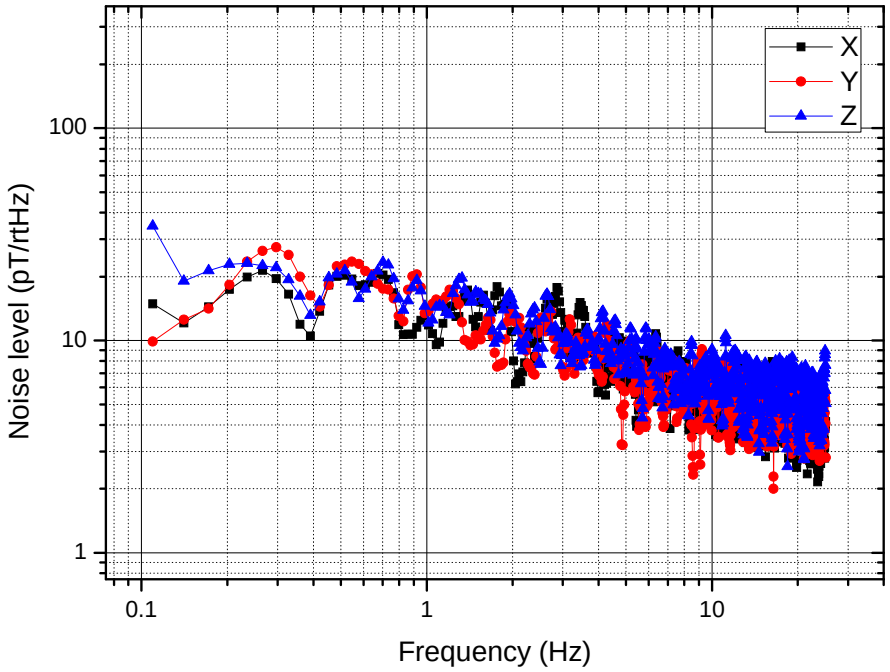

Fig. 7.9 Noise levels of the 3-axis magnetometer using 3-wire array based on NiFe/Cu CWs in the sensing element.

7.2.2 Thermal stability

The thermal stability of the 3-axis magnetometer has been tested in a temperature-controlled shielding chamber as described in section 3.4.3. As shown in Fig. 7.10, the temperature drift factor is +/- 0.35 nT/^{o}C in the temperature range of 10 ^{o}C to 70 ^{o}C and +/- 0.1 nT/ ^{o}C in the range of 20 ^{o}C to 40 ^{o}C. Further reduce of the temperature drift factor can be achieved by using circuit components with low temperature coefficient, optimizing the feedback coil, and matching the temperature expanding coefficient of the components in the sensor head.

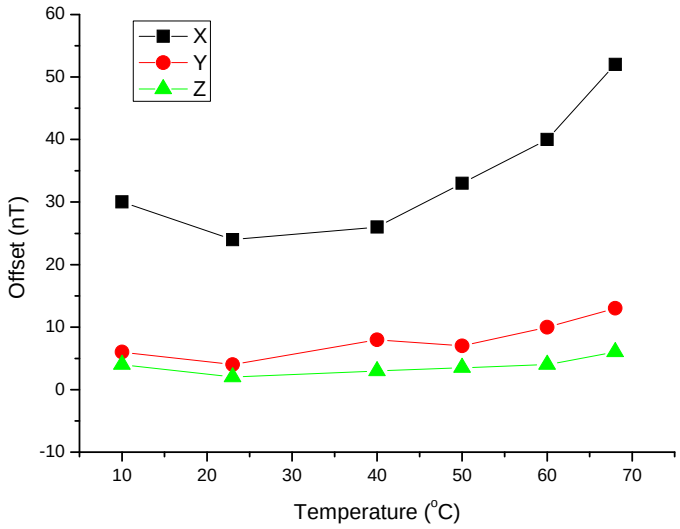

Fig. 7.10 Temperature stability test: sensor offset Vs temperature.

7.2.3 Comparison of NUS MOFG and COTS magnetometers

Main performance specifications of the multi-core orthogonal fluxgate magnetometer developed in this project, including detection range, noise level, operating temperature, power consumption, size, and weight have been compared with the most advanced commercial off-the-shelf magnetometers, as shown in Table 7.2. The advantages of our magnetometer are in the high sensitivity, low noise and small size.

Table 7.2 Performance comparison between NUS MOFG and COTS magnetometers

Fluxgate sensor parameters	Bartington[142]	Applied Physics System Model 544[143]	Billingsley DFMG28[144]	NUS MOFG			
				Single-core		Multi-core	
				Electroplated CW	GCAW	10-wire GCAW	7-wire honeycomb GCAW
Sensing Principle	Parallel fluxgate	Parallel fluxgate	Parallel fluxgate	Orthogonal fluxgate			
Range	+/- 70μT	~ +/-50 μT(?)	+/- 65μT	+/- 50μT	+/- 20μT	+/- 15μT	+/- 50μT
Noise	7-10pT rms/rtHz@1Hz	500pT	8 pT rms/rtHz@1Hz	40pT rms/rtHz@1Hz	40pT rms/rtHz@1Hz	6pT rms/rtHz@1Hz	8.5 pT rms/rtHz@1Hz
Operating Temp. Range	-40^0C- $+70^0$C	0^0C-70^0C	—	10^0C-40^0C	10^0C-40^0C	10^0C-40^0C	10^0C-70^0C
Power consumption	312~442mW	> 350mW	750 mW	280mW	280mW	~400mW	~720mW
Weight	85g	50g	909g	70g			30g
Size	dia25x202mm	20.3 x 19 x 117 mm	dia78 x 305 mm	20x10x10 mm (Readout 80x100x30mm)			20x20x155mm

7.3 Summary

A small size 3-axis multi-core orthogonal fluxgate magnetometer has been designed, fabricated, and tested. The magnetometer has integrated a 3-channel magnetic feedback circuit and three senor heads. The magnetic feedback circuit consists of three circuit modules with functions of current excitation, signal readout, and feedback loop. The magnetometer is working in the close loop mode with enhanced linearity and stability. The sensor heads have been designed and fabricated based on the multi-core sensing element, in which micro-wires arrays using CoFeSiB GCAWs and NiFe/Cu CWs were fabricated with optimum structure parameters, eg. the length of the wires were 10 mm and the structure of the array was 7-wire honeycomb. The three sensor heads have been deployed in the PCB perpendicular to each other.

Performance of the multi-core orthogonal fluxgate magnetometer regarding to the sensitivity, noise level and thermal stability have been tested. The highest sensitivity of 200 mV/μT in a detection range of +/- 50 μT has been achieved with the noise level of 8.5 pT/rtHz@1 Hz, using 7-wire honeycomb structured GCAW array. The lowest noise level of 6 pT/rtHz@1 Hz has been achieved in a low noise version with a detection range of +/- 50 μT, using 10-wire GCAW array. The temperature stability of the 3-axis magnetometer prototype has been tested in a temperature-controlled shielding chamber and the temperature drift factor of +/- 0.35 nT/^{o}C in an operating temperature ranging from 10 ^{o}C to 70 ^{o}C has been achieved. The size of the 3-axis sensor head was within 18 mm x 18 mm x 35 mm and the total size of the magnetometer is 20 mm x 20 mm x 155 mm.

Finally, comparison between our prototype with commercial off-the-shelf magnetometers shows that the multi-core orthogonal fluxgate magnetometer is competitive in regard to the sensitivity, noise, and size.

Chapter 8
Conclusions and Future Work

8.1 Conclusions

The extreme of orthogonal fluxgate sensor in terms of sensitivity and noise has been investigated experimentally and theoretically. Novel multi-core sensing element materials using ferromagnetic micro-wires array have been designed and characterized, the physical mechanism of multi-core orthogonal fluxgate effects has been investigated and modeled, and an orthogonal fluxgate magnetometer using micro-wire array with optimum structure has been designed, fabricated and tested. Both sensitivity and noise depend on the number of wires and the magnetic properties of the arrays. The experimental results showed that the sensitivity increases exponentially with the number of wires. An analytical model indicates that the sensitivity has no limit for the extreme as long as the magnetic properties have not been deteriorated as the number of wires increases. However, the noise in the micro-wire arrays has a minimum with an optimum structure. The theoretical minimum of the white noise is much smaller than the experiment one and is inversely proportional to the number of wires and the susceptibility of arrays.

The magnetic properties of the micro-wire arrays based on near zero magnetostrictive $Co_{68.15}Fe_{4.35}Si_{12.5}B_{15}$ GCAWs fabricated by Taylor-Ulitovsky method and $Ni_{80}Fe_{20}$/Cu CWs prepared by electrodeposition, on their physical dimensions and structures has been investigated by hysteresis loops. The magnetic anisotropy of the wire resulting from the coupling of magnetostriction and internal

stresses can be tailored by varying the ratio of glass coating layer thickness to the metal core radius. The larger the ratio, the smaller the angle between the easy axis of anisotropy and circumferential direction. The results showed a critical length of 10 mm in both GCAWs and CWs below which the anisotropy switched to circumferential direction from original helical direction due to the end domains of the wires. Further, this study revealed that for GCAWs with circumferential anisotropy, the easy axis of the anisotropy inclines more to the circumferential direction with the increase of the number of wires and the dynamic hysteresis loops showed that an ac current flowing into the arrays exasperates such effect. For CWs, the anisotropy variation is just in opposite – the original helical anisotropy inclines to longitudinal direction with the increase of the number of wires. MI measurement confirmed the anisotropy of the arrays and presented the dynamic magnetic properties. In both cases, with the number of the wires increases, the frequency of the maximum MI ratio decreases resulting from the decrease of the domain wall motion frequency due to the enlarged domain dimensions by the interaction.

The characteristics of the orthogonal fluxgate effect have been thoroughly investigated regarding the parameters that influence the sensitivity and noise, such as the working mode, tuning effect, amplitude and frequency of excitation current, and the parameters of the pickup coil. The optimum working condition have been concluded and used for sensor development. The results showed that the sensitivity of the multi-core orthogonal fluxgate sensor is much higher than conventional single-core sensors, and the sensitivity increases exponentially with the increase of the number of wire in the arrays. Under the experimental conditions, the highest

sensitivity recorded is 1663 mV/μT in a GCAW array with 21 wires. The noise level depends on the array structure and the working mode. A minimum noise density has been found for the 5-wire array working in fundamental mode.

Investigation of the interaction between wires showed that the nonlinear increase of the sensitivity occurs only in the closely packed arrays high frequency current passing through not solely due to the increase of the volume of ferromagnetic material. A dynamic magnetic interaction between the ferromagnetic micro-wires is the reason for the exponential increase of the sensitivity with the number of wires.

Based on the measured magnetic properties and orthogonal fluxgate characteristics, the magnetization process of the micro-wire arrays has been modeled by three hysteresis loops. The axial loop has been modeled with small coercivity and small susceptibility, the circular loop has been modeled with large coercivity and large susceptibility and the axial-circular loop is based on the measured gating curves and has been simplified to linear dependence of the axial magnetization on the circular field.

A dipolar interaction model taking into account of the compactedness of the micro-wire arrays has been verified by experimental results on the noise level of arrays with different number of CWs. According to this model the 7-wire honeycomb structure is most favourable array structure which has become the design guide of the multi-core sensing element. Moreover, the nonlinear increase of the sensitivity has been attributed to domain unification effect in which the dimension of the effective domain enlarged and the domain motion frequency decreased. The decreasing trend of

frequency with the number of wires is in good agreement with that of the frequency of the maximum MI ratio in variation with the increase of the number of wires measured in GCAW arrays.

An analytical model of the 2nd harmonic sensitivity of the multi-core orthogonal fluxgate has been established showing that the number of wires, anisotropy field, initial susceptibility and frequency are the key parameters determining the sensitivity. The theoretical results agree well with the measured data from GCAW arrays with the number of wires less than ten. Discrepancy in large number of wires occurrs due to the simplicity of the model and nonuniform arrangement of wires. The model of the white noise of the multi-core sensing element based on a corrected magnetization equilibrium model provides the theoretical limit of the white noise level which is inversely proportional to the number of wires, maximum susceptibility, and working frequency. The theoretical noise of GCAWs is tens of femtotesla which is far below the experimental results while the noise of CWs is less than 4 picotesla which is quite close to the experimental results.

Finally, a 3-axis multi-core orthogonal fluxgate magnetometer based on CoFeSiB GCAW and NiFe/Cu CW micro-wires arrays with optimum structure parameters has been designed, fabricated, and tested. The highest sensitivity of 200 mV/μT in a detection range of +/- 50 μT has been achieved with the noise level of 8.5 pT/rtHz@1 Hz, using 7-wire honeycomb structured GCAW array. The lowest noise level of 6 pT/rtHz@1 Hz has been achieved in a low noise version with a detection range of +/- 15 μT, using 10-wire GCAW array. The operating temperature is ranging from 10 ^{o}C to 70 ^{o}C and the size of the magnetometer is 20 mm x 20 mm x 155 mm.

Compared with commercial off-the-shelf magnetometers the novel multi-core orthogonal fluxgate magnetometer is competitive in regard to the sensitivity, noise, and size.

8.2 Suggestions for future work

Currently the preparation of multi-core sensing element is a tedious and time consuming process. The short wires have to be cut from a long wire sample and the magnetic properties may be changed. Hence, testing on each wire after cutting is necessary to guarantee the homogeneity of the wires. However, the magnetic properties of the wires can be deteriorated by manipulating the wires into the specific arrangement of arrays. Therefore, new method for fabrication and preparation of the multi-core sensing element is needed. Technological challenge is how to produce a large amount of micro-sized ferromagnetic materials with desirable structure and magnetic properties. Template-assisted electrodeposition, sputtering, pulsed laser deposition are all possible approaches.

The new characterization method is also valuable for sensor and material research. The true profile of the domain behavior of many micro-sized materials is still unknown. For example, the interdomain wall dynamics in the GCAWs with core-shell domain structure may play a critical role in the magnetization process of the wires but has not been noticed until recently. The challenge is using what kind of characterization tools can we find these “unsung heroes”.

In theoretical aspect, a more complete model taking into account the true domain structures will be very useful for the orthogonal fluxgate modeling and also for other material studies. The challenge is the complexity of the domain profiles in the materials, especially when the materials are inhomogeneous in composition and structure.

References

[1] R. C. O'Handley, *Modern magnetic materials : principles and applications* New York : Wiley, 1999.

[2] N. C. Jim Daughton, "Magnetic Sensor Market Economic Impact," Nov, 2003.

[3] A. M. Pawlak, *Sensors and Actuators in Mechatronics: Design and Applications*: CRC Press, Taylor & Francis Group, 2007.

[4] P. Ripka, *Magnetic Sensors and Magnetometers*: Artech House, 2001.

[5] O. V. Nielsen*, et al.*, "Development, Construction and Analysis of The ORSTED Fluxgate Magnetometer," *Measurement Science & Technology,* vol. 6, pp. 1099-1115, 1995.

[6] E. Chassefiere*, et al.*, "DYNAMO: a Mars upper atmosphere package for investigating solar wind interaction and escape processes, and mapping Martian fields," *Mercury, Mars and Saturn,* vol. 33, pp. 2228-2235, 2004.

[7] F. Primdahl*, et al.*, "In-flight spacecraft magnetic field monitoring using scalar/vector gradiometry," *Measurement Science & Technology,* vol. 17, pp. 1563-1569, 2006.

[8] F. Primdahl*, et al.*, "Fluxgate magnetometry for precise mapping of the Earth's field," *Sensor Letters,* vol. 5, pp. 110-112, 2007.

[9] M. Acuna, "Fluxgate magnetometers for outer planets exploration," *Magnetics, IEEE Transactions on,* vol. 10, pp. 519-523, 1974.

[10] M. H. Acuna, "Space-based magnetometers," *Review of Scientific Instruments,* vol. 73, pp. 3717-3736, 2002.

[11] P. Ripka and P. Navratil, "Fluxgate sensor for magnetopneumometry," *Sensors and Actuators a-Physical,* vol. 60, pp. 76-79, 1997.

[12] D. Robbes*, et al.*, "Highly sensitive uncooled magnetometers: State of the art. Superconducting magnetic hybrid magnetometers, an alternative to SQUIDs?," *Applied Superconductivity, IEEE Transactions on,* vol. 11, pp. 629-634, 2001.

[13] H. Koch, "SQUID magnetocardiography: status and perspectives," *Applied Superconductivity, IEEE Transactions on,* vol. 11, pp. 49-59, 2001.

[14] A. E. Mahdi, *et al.*, "Some new horizons in magnetic sensing: high-Tc SQUIDs, GMR and GMI materials," *Sensors and Actuators A: Physical,* vol. 105, pp. 271-285, 2003.

[15] O. V. Lounasmaa and H. Seppa, "SQUIDs in neuro- and cardiomagnetism," *Journal of Low Temperature Physics,* vol. 135, pp. 295-335, 2004.

[16] Y. Okada, *et al.*, "BabySQUID: A mobile, high-resolution multichannel magnetoencephalography system for neonatal brain assessment," *Review of Scientific Instruments,* vol. 77, p. 024301, 2006.

[17] M. Pannetier, *et al.*, "Femtotesla Magnetic Field Measurement with Magnetoresistive Sensors," *Science,* vol. 304, pp. 1648-1650, June 11, 2004 2004.

[18] J. Malvivuo and R. Plonsey, *Bioelectromagnetism*. New York: OXFORD UNIVERSITY PRESS, 1995.

[19] D. Polvani, "Magnetic loops as submarine detectors," in *OCEANS*, 1977, pp. 718-723.

[20] S. V. Marshall, "Vehicle detection using a magnetic field sensor," *Vehicular Technology, IEEE Transactions on,* vol. 27, pp. 65-68, 1978.

[21] P. Ripka, *et al.*, "Mine Detection in Magnetic Soils," *Sensor Letters,* vol. 5, pp. 15-18, 2007.

[22] P. Ripka, *et al.*, "DC Gradiometers for Bomb Detection: Scalar Versus Vectorial," *Sensor Letters,* vol. 5, pp. 271-275, 2007.

[23] P. Ripka and P. Kaspar, "Portable fluxgate magnetometer," *Sensors and Actuators a-Physical,* vol. 68, pp. 286-289, 1998.

[24] J. T. Bono, *et al.*, "Magnetic sensor operation onboard a UUV: magnetic noise investigation using a total-field gradiometer," in *OCEANS 2003. Proceedings*, 2003, pp. 2018-2022 Vol.4.

[25] Y. Nishibe, *et al.*, "Sensing of passing vehicles using a lane marker on a road with built-in thin-film MI sensor and power source," *Ieee Transactions on Vehicular Technology,* vol. 53, pp. 1827-1834, 2004.

[26] "Magnetic field sensors roadmap," *National Institute of Standards and Technology,* Nov. 2003.

[27] K. Mohri, *et al.*, "Amorphous wire and CMOS IC-based sensitive micromagnetic sensors utilizing magnetoimpedance (MI) and stress-

impedance (SI) effects," *IEEE Transactions on Magnetics,* vol. 38, pp. 3063-3068, 2002.

[28] P. Ripka, "Precise vectorial magnetic sensors," *Smart Sensors and Mems,* vol. 181, pp. 203-228, 2004.

[29] A. Ito*, et al.*, "Medical application of functionalized magnetic nanoparticles," *Journal of Bioscience and Bioengineering,* vol. 100, pp. 1-11, 2005.

[30] W.-T. Liu, "Nanoparticles and their biological and environmental applications," *Journal of Bioscience and Bioengineering,* vol. 102, pp. 1-7, 2006.

[31] M. Vopalensky*, et al.*, "Precise magnetic sensors," *Sensors and Actuators a-Physical,* vol. 106, pp. 38-42, 2003.

[32] P. Ripka, "New directions in fluxgate sensors," *Journal of Magnetism and Magnetic Materials,* vol. 215, pp. 735-739, 2000.

[33] P. Ripka and G. Vertesy, "Sensors based on soft magnetic materials - Panel discussion," *Journal of Magnetism and Magnetic Materials,* vol. 215, pp. 795-799, 2000.

[34] M. A. M. Caruso, Mr. B, "A new perspective on magnetic field sensing," *Honeywell Inc.,* 2001.

[35] S. M. S. (ed), "Semiconductor Sensors," pp. 207-210, 1994.

[36] F. Primdahl, "The fluxgate magnetometer," *Journal of Physics E: Scientific Instruments,* p. 241, 1979.

[37] E. S. Agency, "Swarm Mission Report," *http://esamultimedia.esa.int/docs/SP_1279_6_Swarm.pdf*.

[38] J. M. G. Merayo*, et al.*, "Triaxial fluxgate gradiometer of high stability and linearity," *Sensors and Actuators a-Physical,* vol. 120, pp. 71-77, 2005.

[39] D. Gordon*, et al.*, "Factors affecting the sensitivity of gamma-level ring-core magnetometers," *Magnetics, IEEE Transactions on,* vol. 1, pp. 330-337, 1965.

[40] S. Chikazumi, *Physics of Ferromagnetism*, 2nd ed.: Oxford University, 1997.

[41] J. W. Rayleigh, *The Philos. Mag.,* vol. 5(XXIII), 1887.

[42] M. L. Brillouin, *J. Phys. Radium,* vol. 8, 1927.

[43] H. Chiriac*, et al.*, "Phenomenological model for the simulation of hysteresis loops in NiFe/Cu multilayered nanowires," 2008, p. 07D919.

[44] Z. Wlodarski, "Classical and hyperbolic approximation of hysteresis loops," *Physica B: Condensed Matter,* vol. 389, pp. 347-350, 2007.

[45] Z. Wlodarski, "Modeling hysteresis by analytical reversal curves," *Physica B: Condensed Matter,* vol. 398, pp. 159-163, 2007.

[46] W. Zdzislaw*, et al.*, "Application of different saturation curves in a mathematical model of hysteresis," *Compel,* vol. 24, p. 1367, 2005.

[47] F. Primdahl, "The fluxgate mechanism, part I: The gating curves of parallel and orthogonal fluxgates," *Magnetics, IEEE Transactions on,* vol. 6, pp. 376-383, 1970.

[48] T. M. Palmer, "A Small Sensitive Magnetometer," *Proc. IEE Part II (London),* vol. 100, p. 545, 1953.

[49] L. R. Alldredge, "Magnetometer," *U.S. patent 2 856 581,* Octorber 14, 1958.

[50] E. O. Schonstedt, "Saturable measuring device and magnetic core therefor," *U.S. patent 2 916 696,* December 8, 1959.

[51] P. E. Gise and R. B. Yarbrough, "An improved cylindrical magnetometer sensor," *Magnetics, IEEE Transactions on,* vol. 12, pp. 1104-1106, 1977.

[52] R. N. G. Dalpadado, "Bipolar magnetometer sensor similar to fluxgate device but having equal input and output sinusoidal frequencies and zero Barkhausen noise," *Electronics Letters,* vol. 28, 1992.

[53] I. Sasada, "Orthogonal fluxgate mechanism operated with dc biased excitation," 2002, pp. 7789-7791.

[54] L. Kraus*, et al.*, "Magnetic field sensor based on asymmetric inverse Wiedemann effect," *Sensors and Actuators A: Physical,* vol. 142, pp. 468-473, 2008.

[55] K. Goleman and I. Sasada, "High Sensitive Orthogonal Fluxgate Magnetometer Using a Metglas Ribbon," *Magnetics, IEEE Transactions on,* vol. 42, pp. 3276-3278, 2006.

[56] O. Zorlu*, et al.*, "An orthogonal fluxgate-type magnetic microsensor with electroplated Permalloy core," *Sensors and Actuators A: Physical,* vol. 135, pp. 43-49, 2007.

[57] I. Sasada, "Symmetric response obtained with an orthogonal fluxgate operating in fundamental mode," *Magnetics, IEEE Transactions on,* vol. 38, pp. 3377-3379, 2002.

[58] E. Paperno, "Suppression of magnetic noise in the fundamental-mode orthogonal fluxgate," *Sensors and Actuators a-Physical,* vol. 116, pp. 405-409, 2004.

[59] P. Anton, *et al.*, "Compensation of the thermal drift in the sensitivity of fundamental-mode orthogonal fluxgates," 2006, p. 08B305.

[60] http://www.aichi-steel.co.jp/ENGLISH/pro_info/pro_intro/elect_3.html.

[61] A. S. Antonov, *et al.*, "Nonlinear magnetization reversal of Co-based amorphous microwires induced by an ac current," *Journal of Physics D-Applied Physics,* vol. 34, pp. 752-757, Mar 2001.

[62] A. S. Antonov, *et al.*, "Nonlinear magnetoimpedance effect in soft magnetic amorphous wires extracted from melt," *Sensors and Actuators A: Physical,* vol. 106, pp. 208-211, 2003.

[63] N. Kawajiri, *et al.*, "Highly stable MI micro sensor using C-MOS IC multivibrator with synchronous rectification," *IEEE Transactions on Magnetics,* vol. 35, pp. 3667-3669, 1999.

[64] K. Mohri, *et al.*, "Sensitive micro magnetic sensor family utilizing magneto-impedance (MI) and stress-impedance (SI) effects for intelligent measurements and controls," *Sensors and Actuators a-Physical,* vol. 91, pp. 85-90, 2001.

[65] A. S. Antonov, *et al.*, "Nondiagonal impedance of amorphous wires with circular magnetic anisotropy," *Journal of Magnetism and Magnetic Materials,* vol. 187, pp. 252-260, Aug 1998.

[66] D. P. Makhnovskiy, *et al.*, "Measurement of field-dependent surface impedance tensor in amorphous wires with circumferential anisotropy," *Journal of Applied Physics,* vol. 87, pp. 4804-4806, May 2000.

[67] D. P. Makhnovskiy, *et al.*, "Field-dependent surface impedance tensor in amorphous wires with two types of magnetic anisotropy: Helical and circumferential," *Physical Review B,* vol. 63, Apr 2001.

[68] S. Sandacci, *et al.*, "Off-diagonal impedance in amorphous wires and its application to linear magnetic sensors," *IEEE Transactions on Magnetics,* vol. 40, pp. 3505-3511, 2004.

[69] K. J. O. I.R. Smith, "The Wiedemann effect: a theoretical and experimental comparison," *Brit. J. Appl. Phys.,* vol. 16, 1965.

[70] A. Hernando and et al., "The inverse Wiedemann effect for low torsional stress," *Journal of Physics D: Applied Physics,* vol. 11, p. 2401, 1978.

[71] E. Pulido, *et al.*, "Amorphous wire magnetic field and DC current sensor based on the inverse Wiedemann effect," *Magnetics, IEEE Transactions on,* vol. 27, pp. 5241-5243, 1991.

[72] J. J. Freijo, *et al.*, "Matteucci and inverse Wiedemann effects in amorphous wires with enhanced circumferential domains," *Journal of Applied Physics,* vol. 85, pp. 5450-5452, Apr 1999.

[73] M. Vazquez and A. Hernando, "A soft magnetic wire for sensor applications," *Journal of Physics D-Applied Physics,* vol. 29, pp. 939-949, Apr 1996.

[74] H. Chiriac, *et al.*, "DC magnetic field measurements based on the inverse Wiedemann effect in Fe-rich glass covered amorphous wires," *IEEE Transactions on Magnetics,* vol. 35, pp. 3625-3627, 1999.

[75] H. Chiriac, *et al.*, "Inverse Wiedemann Effect in glass-covered amorphous wires," in *2nd European Conference on Magnetic Sensors and Actuators*, Sheffield, England, 1998, pp. 147-149.

[76] R. H. Koch, *et al.*, "Fundamental limits to magnetic-field sensitivity of flux-gate magnetic-field sensors," *Applied Physics Letters,* vol. 75, pp. 3862-3864, 1999.

[77] D. Scouten, "Sensor noise in low-level flux-gate magnetometers," *Magnetics, IEEE Transactions on,* vol. 8, pp. 223-231, 1972.

[78] R. H. Koch and J. R. Rozen, "Low-noise flux-gate magnetic-field sensors using ring- and rod-core geometries," *Applied Physics Letters,* vol. 78, pp. 1897-1899, 2001.

[79] K. Shirae, "Noise in amorphous magnetic materials," *Magnetics, IEEE Transactions on,* vol. 20, pp. 1299-1301, 1984.

[80] M. Vazquez and D. X. Chen, "The magnetization reversal process in amorphous wires," *Magnetics, IEEE Transactions on,* vol. 31, pp. 1229-1238, 1995.

[81] V. M. A. Hernando, M.C. Sanchez, M. Vazquez (Eds.), *Magnetic Properties of Amorphous Metals*. Amsterdam: Elsevier, 1987.

[82] H. H. L. (Ed.), *Rapidly Solidified Alloys*. New York: Marcel Dekker, 1993.

[83] H. L. Seet, *et al.*, "Development of high permeability nanocrystalline permalloy by electrodeposition," *Journal of Applied Physics,* vol. 97, 2005.

[84] X. P. Li, *et al.*, "Electrodeposition and characteristics of Ni80Fe20/Cu composite wires," *Journal of Magnetism and Magnetic Materials,* vol. 304, pp. 111-116, 2006.

[85] H. Chiriac and T. A. Óvári, "Amorphous glass-covered magnetic wires: Preparation, properties, applications," *Progress in Materials Science,* vol. 40, pp. 333-407, 1996.

[86] K. Mohri, *et al.*, "LARGE BARKHAUSEN AND MATTEUCCI EFFECTS IN FECOSIB, FECRSIB, AND FENISIB AMORPHOUS WIRES," *IEEE Transactions on Magnetics,* vol. 26, pp. 1789-1791, 1990.

[87] H. Chiriac, *et al.*, "Magnetoelastic anisotropy of amorphous microwires," in *15th International Symposium on Soft Magnetic Materials*, Bilbao, Spain, 2001, pp. 469-471.

[88] E. E. Shalyguina, *et al.*, "Magneto-optical investigation of local magnetic properties and micromagneticstructure of NiFe/Cu microwires," *Thin Solid Films,* vol. 505, pp. 165-167, 2006.

[89] J. Velázquez, *et al.*, "Dynamic magnetostatic interaction between amorphous ferromagnetic wires," *Physical Review B,* vol. 54, p. 9903, 1996.

[90] L. C. Sampaio, *et al.*, "Magnetic microwires as macrospins in a long-range dipole-dipole interaction," *Physical Review B,* vol. 61, p. 8976, 2000.

[91] Y. Di, *et al.*, "Collective length effect on the magnetostatic properties of arrays of glass-coated amorphous alloy microwires," *Journal of Magnetism and Magnetic Materials,* vol. 320, pp. 534-539, 2008.

[92] J. Velazquez, *et al.*, "About the dipolar approach in magnetostatically coupled bistable magnetic micro and nanowires," *Magnetics, IEEE Transactions on,* vol. 39, pp. 3049-3051, 2003.

[93] H. Chiriac, *et al.*, "Dipolar interaction between amorphous microwires," *IEEE Transactions on Magnetics,* vol. 44, pp. 479-484, Apr 2008.

[94] R. Piccin and et al., "Magnetostatic interactions between two magnetic wires," *EPL (Europhysics Letters),* vol. 78, p. 67004, 2007.

[95] A. Chizhik and et al., "Interaction between Co-rich glass-covered microwires," *Journal of Physics D: Applied Physics,* vol. 36, p. 1058, 2003.

[96] A. Pereira, *et al.*, "How do magnetic microwires interact magnetostatically?," *Journal of Applied Physics,* vol. 105, p. 083903, 2009.

[97] X. P. Li, *et al.*, "Multi-core orthogonal fluxgate sensor," *Journal of Magnetism and Magnetic Materials,* vol. 300, pp. e98-e103, 2006.

[98] S. Foner, "Versatile and Sensitive Vibrating-Sample Magnetometer," *Review of Scientific Instruments,* vol. 30, pp. 548-557, 1959.

[99] P. P. a. A. K. R. A. Niazi, "A precision, low-cost vibrating sample magnetometer," *CURRENT SCIENCE,* vol. 79, pp. 99-109, 2000.

[100] J. Hernando and J. M. Barandiaran, "Circular magnetisation measurement in ferromagnetic wires," *Journal of Physics D: Applied Physics,* vol. 11, p. 1539, 1978.

[101] L. V. Panina and K. Mohri, "Magneto-impedance effect in amorphous wires," *Applied Physics Letters,* vol. 65, pp. 1189-1191, 1994.

[102] R. S. Beach and A. E. Berkowitz, "Giant magnetic field dependent impedance of amorphous FeCoSiB wire," *Applied Physics Letters,* vol. 64, pp. 3652-3654, 1994.

[103] A. Zhukov, *et al.*, "Recent advances in studies of magnetically soft amorphous microwires," *Journal of Magnetism and Magnetic Materials,* vol. 321, pp. 822-825, 2009.

[104] D. de Cos, *et al.*, "High-frequency magnetoimpedance in multilayer thin films with longitudinal and transverse anisotropy," *Journal of Magnetism and Magnetic Materials,* vol. 320, pp. e954-e957, 2008.

[105] D. Muraca, *et al.*, "Influence of Ge on magnetic and structural properties of Joule-heated Co-based ribbons: Giant magnetoimpedance response," *Journal of Magnetism and Magnetic Materials,* vol. 320, pp. 2068-2073, 2008.

[106] É. Kisdi-Koszó, *et al.*, "Magnetic properties of finemet-type thin layers," *Journal of Magnetism and Magnetic Materials,* vol. 160, pp. 333-334, 1996.

[107] X. P. Li, *et al.*, "Portable comprehensive magnetic shielding cylinder for weak magnetic field sensor testing in an island free of ac noise," in *Magnetics Conference, 2005. INTERMAG Asia 2005. Digests of the IEEE International*, 2005, pp. 1537-1538.

[108] J. Fan, *et al.*, "Low power orthogonal fluxgate sensor with electroplated Ni80Fe20/Cu wire," *Journal of Applied Physics,* vol. 99, 2006.

[109] R. S. Popovic, *et al.*, "The future of magnetic sensors," *Sensors and Actuators A: Physical,* vol. 56, pp. 39-55, 1996.

[110] B. Z. Kaplan and U. Suissa, "Experimental proof that fluxgates operation is directly related to electric antennas theory," *Sensors and Actuators A: Physical,* vol. 69, pp. 226-233, 1998.

[111] L. Perez*, et al.*, "Analytical model for the sensitivity of a toroidal fluxgate sensor," *Sensors and Actuators a-Physical,* vol. 130, pp. 142-146, 2006.

[112] P. Ripka*, et al.*, "Characterisation of magnetic wires for fluxgate cores," *Sensors and Actuators A: Physical,* vol. In Press, Corrected Proof.

[113] M. Butta and P. Ripka, "Model for coil-less fluxgate," *Sensors and Actuators A: Physical,* vol. 156, pp. 269-273, 2009.

[114] P. Ripka*, et al.*, "Multiwire core fluxgate," *Sensors and Actuators A: Physical,* vol. 156, pp. 265-268, 2009.

[115] http://en.wikipedia.org/wiki/Thermoelectric_Modules.

[116] http://www.ferrotec.com/products/thermal/modules/.

[117] A. P. Zhukov*, et al.*, "The remagnetization process in thin and ultra-thin Fe-rich amorphous wires," *Journal of Magnetism and Magnetic Materials,* vol. 151, pp. 132-138, 1995.

[118] V. Zhukova*, et al.*, "Length effect in a negative magnetostrictive Co-Si-B amorphous wire with rectangular hysteresis loop," *Journal of Magnetism and Magnetic Materials,* vol. 254-255, pp. 182-184, 2003.

[119] A. M. Severino*, et al.*, "Influence of the sample length on the switching process of magnetostrictive amorphous wire," *Journal of Magnetism and Magnetic Materials,* vol. 103, pp. 117-125, 1992.

[120] D. Atkinson*, et al.*, "THE MAGNETIC AND MAGNETOELASTIC PROPERTIES OF SURFACE CRYSTALLIZED IRON-BASED AMORPHOUS WIRE," *Journal of Magnetism and Magnetic Materials,* vol. 131, pp. 19-28, 1994.

[121] P. T. Squire*, et al.*, "MAGNETOSTRICTIVE AND MAGNETOELASTIC PROPERTIES OF RAPIDLY QUENCHED WIRE," *IEEE Transactions on Magnetics,* vol. 31, pp. 1239-1248, 1995.

[122] S. Atalay*, et al.*, "Magnetoelastic properties of annealed Co72.5Si12.5B15 amorphous wires," *Journal of Magnetism and Magnetic Materials,* vol. 158, pp. 145-146, 1996.

[123] H. Chiriac*, et al.*, "Magnetic hysteresis in glass-covered and water-quenched amorphous wires," in *International Conference on Magnetism*, Cairns, Australia, 1997, pp. 205-206.

[124] H. Chiriac*, et al.*, "Magnetoelastic behavior in Co-based glass-covered amorphous wires," in *International Magnetics Conference (Intermag Europe 2002)*, Amsterdam, Netherlands, 2002, pp. 2823-2825.

[125] H. Chiriac*, et al.*, "Optimized GMI response of co-based amorphous glass-coated microwires by direct control over the magnetoelastic anisotropy from the surface region," in *10th Joint Magnetism and Magnetic Materials Conference/International Magnetics Conference*, Balitmore, MD, 2007, pp. 2977-2979.

[126] Z. J. Zhao*, et al.*, "Comparative study of the sensing performance of orthogonal fluxgate sensors with different amorphous sensing elements," *Sensors and Actuators a-Physical,* vol. 136, pp. 90-94, 2007.

[127] H. Chiriac*, et al.*, "Amorphous glass-covered magnetic wires for sensing applications," *Sensors and Actuators A: Physical,* vol. 59, pp. 243-251, 1997.

[128] K. Mohri*, et al.*, "Recent advances of micro magnetic sensors and sensing application," *Sensors and Actuators a-Physical,* vol. 59, pp. 1-8, 1997.

[129] D. Menard*, et al.*, "Modeling of domain structure and anisotropy in glass-covered amorphous wires," 1998, pp. 6566-6568.

[130] T. A. Ovari*, et al.*, "Near-Surface Magnetic Structure and GMI Response in Amorphous Microwires," *Magnetics, IEEE Transactions on,* vol. 45, pp. 4282-4285, 2009.

[131] M. H. Phan*, et al.*, "Large enhancement of GMI effect in polymer composites containing Co-based ferromagnetic microwires," *Journal of Magnetism and Magnetic Materials,* vol. 316, pp. e253-e256, 2007.

[132] J. M. Barandiaran*, et al.*, "Influence of magnetization processes and device geometry on the GMI effect," *Magnetics, IEEE Transactions on,* vol. 38, pp. 3051-3056, 2002.

[133] M. Takajo*, et al.*, "Domain observations of Fe and Co based amorphous wires," *Magnetics, IEEE Transactions on,* vol. 29, pp. 3484-3486, 1993.

[134] R. Varga*, et al.*, "Single-Domain Wall Propagation and Damping Mechanism during Magnetic Switching of Bistable Amorphous Microwires," *Physical Review Letters,* vol. 94, p. 017201, 2005.

[135] J. Fan, *et al.*, "Study of the Noise in Multicore Orthogonal Fluxgate Sensors Based on Ni-Fe/Cu Composite Microwire Arrays," *Magnetics, IEEE Transactions on,* vol. 45, pp. 4451-4454, 2009.

[136] P. Ripka, *et al.*, "Permalloy GMI sensor," *Journal of Magnetism and Magnetic Materials,* vol. 254, pp. 633-635, 2003.

[137] M. V. M. Knobel, and L. Kraus, "Giant Magnetoimpedance," *in K.H.J. Buschow (ed): Handbook of Magnetic Materials,* vol. 15, pp. 497-563, 2003.

[138] F. E. Atalay and et al., "Magnetoimpedance effect in electroplated NiFeRu/Cu wire," *Journal of Physics D: Applied Physics,* vol. 39, p. 431, 2006.

[139] X. P. Li, *et al.*, "A design of orthogonal fluxgate sensor," 2006, p. 08B313.

[140] T. Kanno, *et al.*, "Amorphous wire MI micro sensor using C-MOS IC multivibrator," *IEEE Transactions on Magnetics,* vol. 33, pp. 3358-3360, 1997.

[141] L. P. Shen, *et al.*, "Mechano-encephalogram based on amorphous wire micro SI acceleration sensor," *IEEE Transactions on Magnetics,* vol. 37, pp. 2007-2009, 2001.

[142] http://www.bartington.com.

[143] Http://www.appliedphysics.com.

[144] http://www.magnetometer.com/.

Appendix A Schematic drawing of the circuit for 3-axis multi-core orthogonal fluxgate magnetometer